Calhoun: The NPS Institutional Archive

DSpace Repository

Theses and Dissertations | 1. Thesis and Dissertation Collection, all items

2008-12

Modeling the performance of MEMS based directional microphones

Chatzopoulos, Dimitrios.

Monterey, California. Naval Postgraduate School

http://hdl.handle.net/10945/3797

Downloaded from NPS Archive: Calhoun

http://www.nps.edu/library

Calhoun is the Naval Postgraduate School's public access digital repository for research materials and institutional publications created by the NPS community. Calhoun is named for Professor of Mathematics Guy K. Calhoun, NPS's first appointed -- and published -- scholarly author.

Dudley Knox Library / Naval Postgraduate School
411 Dyer Road / 1 University Circle
Monterey, California USA 93943

NAVAL POSTGRADUATE SCHOOL

MONTEREY, CALIFORNIA

THESIS

MODELING THE PERFORMANCE OF MEMS BASED DIRECTIONAL MICROPHONES

by

Dimitrios Chatzopoulos

December 2008

Thesis Advisor: Daphne Kapolka
Co-Advisor: Gamani Karunasiri

Approved for public release; distribution is unlimited

THIS PAGE INTENTIONALLY LEFT BLANK

REPORT DOCUMENTATION PAGE		Form Approved OMB No. 0704-0188

Public reporting burden for this collection of information is estimated to average 1 hour per response, including the time for reviewing instruction, searching existing data sources, gathering and maintaining the data needed, and completing and reviewing the collection of information. Send comments regarding this burden estimate or any other aspect of this collection of information, including suggestions for reducing this burden, to Washington headquarters Services, Directorate for Information Operations and Reports, 1215 Jefferson Davis Highway, Suite 1204, Arlington, VA 22202-4302, and to the Office of Management and Budget, Paperwork Reduction Project (0704-0188) Washington DC 20503.

1. AGENCY USE ONLY *(Leave blank)*	2. REPORT DATE December 2008	3. REPORT TYPE AND DATES COVERED Master's Thesis

4. TITLE AND SUBTITLE Modeling the Performance of MEMS Based Directional Microphones	5. FUNDING NUMBERS
6. AUTHOR(S) Dimitrios Chatzopoulos	
7. PERFORMING ORGANIZATION NAME(S) AND ADDRESS(ES) Naval Postgraduate School Monterey, CA 93943-5000	8. PERFORMING ORGANIZATION REPORT NUMBER
9. SPONSORING /MONITORING AGENCY NAME(S) AND ADDRESS(ES) N/A	10. SPONSORING/MONITORING AGENCY REPORT NUMBER

11. SUPPLEMENTARY NOTES The views expressed in this thesis are those of the author and do not reflect the official policy or position of the Department of Defense or the U.S. Government.

12a. DISTRIBUTION / AVAILABILITY STATEMENT Approved for public release; distribution unlimited	12b. DISTRIBUTION CODE

13. ABSTRACT (maximum 200 words)

A Micro Electro Mechanical System (MEMS) based directional microphone consisting of two plates hinged at the center is modeled using finite element software. A new method is developed in which the sensor is acoustically coupled to an incoming sound wave. The method successfully reproduces results of previous non-acoustic coupled simulations for solid plates. The resonance frequencies match within 0.8% for the rocking mode and 2% for the bending mode. The displacement amplitudes match within 17% for the rocking mode and 5% for the bending mode.

After ensuring agreement with previous simulations, the model was extended to include more realistic boundary conditions. The sound pressure at the back of the plates is included along with the drag force on the plates due to the acoustic particle velocity flow. This new model reproduces the experimentally achieved resonance frequency values within 21% for the rocking mode and 2% for the bending mode. The displacement amplitude obtained for the rocking mode is approximately 6 times lower than the experimental value while the bending mode amplitude is 47% higher. Manufacturing tolerances for these MEMS devices likely contribute to the discrepancy between simulated and experimental values.

A novel design is proposed for increasing the displacement amplitude for both solid and perforated plates through the use of a Helmholtz resonator.

14. SUBJECT TERMS MEMS, Simulation, Directional, Microphone, Acoustics, COMSOL	15. NUMBER OF PAGES 115
	16. PRICE CODE

17. SECURITY CLASSIFICATION OF REPORT	18. SECURITY CLASSIFICATION OF THIS PAGE	19. SECURITY CLASSIFICATION OF ABSTRACT	20. LIMITATION OF ABSTRACT
Unclassified	Unclassified	Unclassified	UU

NSN 7540-01-280-5500

Standard Form 298 (Rev. 8-98)
Prescribed by ANSI Std. Z39.18

THIS PAGE INTENTIONALLY LEFT BLANK

Approved for public release; distribution is unlimited

MODELING THE PERFORMANCE OF MEMS BASED DIRECTIONAL MICROPHONES

Dimitrios Chatzopoulos
Lieutenant, Hellenic Navy
B.A. in Applied Sciences, Hellenic Naval Academy, 1997

Submitted in partial fulfillment of the
requirements for the degree of

MASTER OF SCIENCE IN ENGINEERING ACOUSTICS

from the

NAVAL POSTGRADUATE SCHOOL
December 2008

Author: Dimitrios Chatzopoulos

Approved by: Daphne Kapolka
Thesis Advisor

Gamani Karunasiri
Co-Advisor

Daphne Kapolka
Chair, Engineering Acoustics Academic Committee

THIS PAGE INTENTIONALLY LEFT BLANK

ABSTRACT

A Micro Electro Mechanical System (MEMS) based directional microphone consisting of two plates hinged at the center is modeled using finite element software. A new method is developed in which the sensor is acoustically coupled to an incoming sound wave. The method successfully reproduces results of previous non-acoustic coupled simulations for solid plates. The resonance frequencies match within 0.8% for the rocking mode and 2% for the bending mode. The displacement amplitudes match within 17% for the rocking mode and 5% for the bending mode.

After ensuring agreement with previous simulations, the model was extended to include more realistic boundary conditions. The sound pressure at the back of the plates is included along with the drag force on the plates due to the acoustic particle velocity flow. This new model reproduces the experimentally achieved resonance frequency values within 21% for the rocking mode and 2% for the bending mode. The displacement amplitude obtained for the rocking mode is approximately 6 times lower than the experimental value while the bending mode amplitude is 47% higher. Manufacturing tolerances for these MEMS devices likely contribute to the discrepancy between simulated and experimental values.

A novel design is proposed for increasing the displacement amplitude for both solid and perforated plates through the use of a Helmholtz resonator.

THIS PAGE INTENTIONALLY LEFT BLANK

TABLE OF CONTENTS

I. INTRODUCTION 1
A. MOTIVATION 1
B. CONTRIBUTIONS OF THIS THESIS 2
C. THESIS ORGANIZATION 3

II. BACKGROUND 5
A. THE ORMIA OCHRACEA 5
B. KARUNASIRI'S BIOMIMICRY WORK 8

III. THEORY 11
A. OVERVIEW 11
B. ACOUSTIC CONSIDERATIONS 11
1. Relationship between Pressure and Particle Velocity 11
2. The Near Field and Far Field of a Source 12
3. Directionality of an Acoustic Sensor 14
4. Time Difference of Arrival 15
5. Achieving Greater Directionality with Smaller Sensors 16
6. Quality Factor of a Microphone 17
C. THE SIMPLIFIED MECHANICAL MODEL 18
D. AIR DAMPING 25
E. RESONATOR CAVITIES 31

IV. DESIGN DETAILS OF PREVIOUS NPS MEMS SENSORS 33
A. MEMS DESIGN AND CONSIDERATIONS 33

V. MODELING - SIMULATION 39
A. OVERVIEW 39
B. COMSOL SOFTWARE 40
1. Basic Simulation Procedure and Parameters 40
2. System Requirements 44
C. NON - ACOUSTIC COUPLED SIMULATIONS 44
1. General Settings and Considerations 45
2. Results 49
D. ACOUSTIC COUPLED SIMULATIONS 51
1. Main Considerations 52
2. Box Domain Model Simulation 54
a. Simulation Settings 54
b. Results 57
3. Sphere Domain Model Simulation 61
a. Simulation Settings 61
b. Results 64
c. Results for Revised Sphere Radius 68
4. Revised Damping Simulations 75
5. Perforated Plate Simulation 80

6. Device with Resonant Cavity 85
VI. CONCLUSIONS AND RECOMMENDATIONS FOR FUTURE WORK 91
APPENDIX 95
BACK OF THE ENVELOPE CALCULATION FOR THE DAMPING FORCE BASED ON THE MODIFIED ZHANG FORMULA 95
LIST OF REFERENCES 97
INITIAL DISTRIBUTION LIST 99

LIST OF FIGURES

Figure 1. Fly's auditory system (From: Miles et al., 1995) 7
Figure 2. Simple model of the fly's auditory system (*From*: Miles *et al.*, 1995) 8
Figure 3. General schematic of MEMS device (*From*: Karunasiri *et al*., 2005) 9
Figure 4. Difference in distance of signals arriving from the center and the end of a line source to two different spatial points. 13
Figure 5. Sound direction determination with the use of two omnidirectional point receivers. 15
Figure 6. Simplified model of the fly's auditory system (*After*: Shivok, 2007)..... 19
Figure 7. Rocking and bending modes of the mechanical model (*From*: Robert *et a*l., 1996). 22
Figure 8. Incident pressure wave on the MEMS device. (*From*: Dritsas, 2008). 23
Figure 9. Variation of quality factor with air pressure for resonators having various length to thickness ratios for both free space and squeeze-film damping (*From*: Newell, 1968). 27
Figure 10. Silicon cantilevers with different dimensions used by Zhang to determine air damping (*From*: Zhang *et al.*, 2006). 28
Figure 11. Experimental and numerical results justifying the linear model for the damping coefficient in equation (3.15) (*From*: Zhang *et al.*, 2006). 29
Figure 12. Damping coefficient for various cross sections (*From*: Zhang *et. al.*, 2006). 30
Figure 13. Initial design of a perforated MEMS device based on the PolyMUMPs' construction procedure (*From*: Shivok, 2007). 34
Figure 14. Latest chip layout composed of 15 sensors of different design. (*From*: Dritsas, 2008)..... 35
Figure 15. Device #8 - Solid plate design with slit in center (*From*: Dritsas, 2008). 36
Figure 16. Device with removed substrate and the support structure (*From*: Dritsas, 2008). 37
Figure 17. Rocking mode of oscillation. 38
Figure 18. Bending mode of oscillation. 38
Figure 19. Application mode selection used in COMSOL simulations. 41
Figure 20. Subdomain settings for solid stress-strain and pressure acoustics application modes..... 42
Figure 21. Mesh mode and mesh statistics in COMSOL. 43
Figure 22. Definition of polar angle "θ" and azimuthal angle "ψ"..... 46
Figure 23. Set parameters for incident pressure at the upper plate. 48
Figure 24. Set parameters for air damping under the plate. 48
Figure 25. Simulated frequency response of Device #8 in the vertical direction.. 50
Figure 26. Displacement of rocking and bending mode versus angle of incidence (*After*: Dritsas, 2008). 51

Figure 27. Coupling of the acoustic pressure in the MEMS solid stress-strain module (upper side of plate). 53
Figure 28. Coupling of the normal acceleration in the Acoustics Module. 53
Figure 29. Schematic of the “Box Model”. 55
Figure 30. Boundary settings on the upper side of the box. 56
Figure 31. “Box Model” rocking mode. 58
Figure 32. “Box Model” bending mode. 58
Figure 33. Simulated frequency response for the “Box Model”. 59
Figure 34. Simulated pressure response for the “Box Model”. 60
Figure 35. Schematic of the “Sphere Domain” model, 8mm radius. 62
Figure 36. Point sound source settings and position. 63
Figure 37. Simulated frequency response for the 8mm radius “Sphere Model”... 65
Figure 38. Pressure difference at the two edges of the MEMS device. 66
Figure 39. Simulated pressure difference at the two edges of the MEMS device. 67
Figure 40. Sound Pressure Level of the “Sphere Model” at f = 3,450 Hz. 68
Figure 41. Sound Pressure Level over a diagonal at f = 3450 Hz. 69
Figure 42. Pressure difference at the two edges of the MEMS Device with Acoustic Domain radius of 3 cm. 69
Figure 43. Device deformation in the rocking mode frequency – Sphere Model. 70
Figure 44. Device deformation in the bending mode frequency – Sphere Model. 70
Figure 45. Comparison plot between the non-acoustic coupled and acoustic coupled simulation run using the Sphere Model. 72
Figure 46. Displacement versus angle of incidence for the rocking and bending mode – Sphere Model. 73
Figure 47. Frequency response of two identical sensors (*After*: Dritsas, 2008)... 74
Figure 48. Revised back boundary settings. 77
Figure 49. Frequency response for revised boundary settings. 78
Figure 50. Experimental response for the rocking and bending mode (*From*: Dritsas, 2008). 79
Figure 51. 2-D representation of Device #10. 81
Figure 52. 4-Hole equivalent of Device #10. 82
Figure 53. Frequency response for a 4-hole equivalent of Device #10. 84
Figure 54. Resonator cavity and MEMS device. 86
Figure 55. Frequency response of a MEMS device mounted on a resonant cavity. 88
Figure 56. Pressure amplitude on the device plates around the cavity resonance. 89

LIST OF TABLES

Table 1. Parameters used in the model presented by Dritsas [After: Dritsas, 2008]. 47
Table 2. COMSOL simulation results for solid plate Device #8. value for air density is ρ=1.025 kg/m^3 [*From*: Dritsas, 2008]. 49
Table 3. COMSOL simulation results for a solid plate device in a Box Acoustic Domain..... 59
Table 4. COMSOL simulation results for a solid plate device in Box Acoustic Domains of varying sizes..... 61
Table 5. COMSOL simulation results for a solid plate device in a sphere Acoustic Domain, radius 8 mm. 64
Table 6. COMSOL simulation results for a solid plate device in a spherical Acoustic Domain for various angles of incidence, radius R=3 cm. 71
Table 7. COMSOL simulation results for a solid plate device in a sphere Acoustic Domain with revised boundary conditions. 77
Table 8. Experimental values as presented by Dritsas (*From*: Dritsas, 2008).. 79
Table 9. Comparison of simulation and experimental results for the solid, non-backed MEMS device..... 80
Table 10. Simulated results for a 4-hole equivalent of Device #10 in a spherical Acoustic Domain. 84
Table 11. Simulated results for a MEMS device backed by a resonator cavity. . 87

THIS PAGE INTENTIONALLY LEFT BLANK

ACKNOWLEDGMENTS

I would like to thank Professor Daphne Kapolka for her mentorship, guidance, support, and patience throughout this effort. It has been a privilege working with you.

I would also like to thank Professor Gamani Karunasiri for his guidance and support.

I would like to thank Joy Newman for editing this thesis.

Last, but not least, I would like to thank my wife, Evangelia, for her everlasting support and patience during this effort.

THIS PAGE INTENTIONALLY LEFT BLANK

I. INTRODUCTION

A. MOTIVATION

Hearing is one of the senses used by creatures in nature to locate and track other living organisms or objects. The ability to perform that action successfully depends upon the directional capabilities of their auditory systems. Possessing the capability to correctly determine the direction of incoming sound can help them, amongst other things, detect their prey, find a host for reproduction, or navigate in space.

Civilian and military applications have used acoustic sensors for many years. Examples include sonar, which remains the primary method of detecting objects underwater, an early detection device of incoming airplanes in World War II, and many others. The directional capability of these sensors is one measure of their effectiveness. Most of the manmade devices used today to detect sound, such as microphones or hydrophones, sense the pressure of an acoustic wave and convert the pressure signal into a voltage output. The time difference Δt of arrival in the incoming pressure signal between the consecutive sensors in an array can be used to determine its direction. It turns out that the longer the array, the greater its directionality. The theory chapter of this thesis provides further details on the subject of directionality.

An alternative to the pressure sensor, which has the potential to achieve good directionality with a smaller sensor, is the “particle velocity sensor.” These detect the acoustic particle velocity of an incoming sound wave. The particle velocity (unlike pressure) is a vector quantity.

In an attempt to achieve greater directionality in a small sensor, insect hearing has also been examined. One particular insect studied is the fly known as “Ormia Ochracea.”

Because of its small size, if the fly relied solely on the time difference of arrival of the acoustic pressure between two ears, it would not be able to determine the direction of sound. As it turns out, however, the fly is able to determine the direction of its prey. The directional capability in this case is based on a mechanism that detects the difference in the amplitude of oscillation between two membranes present in its auditory system.

In principle, constructing a sensor similar to the fly's system would require only one device to determine the direction of sound given a high enough signal to noise ratio (SNR). Moreover, the dimensions of that device would be small compared to other sensors in use today. There are many possible applications for such a sensor. Application examples could be in underwater acoustics, as a passive receiver on sonar devices, and in air where it could be placed together with other micro devices to form a compact sensor system capable of sensing a wide variety of signals in the environment.

B. CONTRIBUTIONS OF THIS THESIS

This thesis focuses on the designs, modeling, and experimental results of Micro-Electro-Mechanical Systems (MEMS) built by a team headed by Professor Karunasiri of the Naval Postgraduate School (NPS). These devices were based on the principles governing the auditory system of the "Ormia Ochracea." Previous students simulated the effect of the incoming pressure wave on the device by computing the force the free field acoustic wave would exert on the top of the device. In contrast, the simulations conducted for this thesis models the results of the incoming pressure wave by coupling the acoustic and MEMS domains. This is an important difference, because at frequencies where the wavelength is large compared to the dimensions of the device, the acoustic pressure on the back of the device is not expected to be negligible. A second contribution of this thesis involves the treatment of air damping. Previous simulations treated the air damping as proportional to the velocity of the device. This is perfectly reasonable for a device oscillating in still air. A sound wave,

however, produces movement of the air molecules. In this thesis, the force resulting from the movement of the device relative to air is calculated based on the difference between the device velocity and the particle velocity of the sound wave moving past it. Lastly, this thesis proposes a novel design that has the potential for increasing the amplitude of the sensor's response by using a resonant cavity behind the device.

C. THESIS ORGANIZATION

Chapter II of this thesis is devoted to a brief background on the biomimicry efforts involving the fly's ear. To show the motivation behind the design of an acoustics MEMS device, it includes a brief description of the auditory system of the fly. It also provides a glimpse of previous NPS successes in designing, constructing, and testing these devices.

Chapter III focuses on the theory involved with these sensors. It discusses acoustic considerations, such as the relationship between pressure and particle velocity, the near and far field of a sound source, sensor directionality issues, and the quality factor of a microphone. This provides a physical basis for decisions made later in the simulation section. Following that, it presents the physics of the mechanical model of the fly's ears created by Miles *et al.,* [1995]. It discusses the air damping mechanisms that limit the amplitude of an acoustics MEMS device and concludes with some of the properties of Helmholtz resonators. These set the stage for understanding how the use of a resonant cavity might result in sound signal amplification.

Chapter IV provides details on the designs of previous and current acoustic MEMS sensors. These include the construction material, dimensions, and some of the basic factors that determine their physical behavior.

Chapter V on the modeling effort contains a summary of previous work as well as the changes and new ideas made in support of this thesis. Details are

provided to enable the reader to reproduce the simulation results, and comparisons are made with both previous simulations as well as the experimental results.

The thesis concludes with several recommendations for future work. Based on the results obtained, it appears most likely that solid plates without a backing represent the best option for reproducing the ability of a fly to determine sound directionality. The ability of a resonant cavity to amplify the response while preserving directionality looks promising but needs further study to verify.

II. BACKGROUND

The work upon which this thesis builds falls into two broad categories. First, it builds upon the work of Miles from the State University of New York at Binghampton. He and his collaborators analyzed the mechanism by which the fly (Ormia Ochracea) achieves sound directionality with its ear. They started publishing this work in the mid 1990's and are currently involved in the design and testing of MEMS biomimetic devices. At about the same time that Miles' group started fabricating MEMS devices, Karunasiri's group at the Naval Postgraduate School began an independent program to design, fabricate, and test biomimetic MEMS sensors. To date, this work resulted in two theses. These two theses constitute the specific design, simulation, and experimental background for this thesis. A variety of research groups have also published studies on the damping mechanisms for MEMS sensors. The work of Zhang and Turner from the University of California Santa Barbara has been particularly useful. As it applies, however, to a very specific aspect of this thesis, Chapter III covers this in the theory portion.

A. THE ORMIA OCHRACEA

Ormia Ochracea is a parasitoid which, to reproduce itself, must lay its larvae on a cricket. The fly locates the cricket solely by using its hearing capabilities. Miles *et al.*, [1995] analyzed the anatomy and physiology of this fly. Taking into consideration that the distance between the hearing organs of the fly is between 450 to 520 μm, the time difference Δt at which the incoming signal would be sensed would be about 1.4μs. This time difference, about a thousand times less than for humans, is extremely small. It cannot be translated into direction using a mechanism that depends solely on the time dependence of the incoming pressure wave at different points [Miles *et al.,* 1995].

Another way to view the problem of directionality is to consider the dimensions of the fly (1.5mm total length) and compare them to the incoming

signal wavelength, which, in the case of the cricket, is 7cm for a frequency of 4.8kHz [Miles *et al.,* 1995]. According to Kinsler [Kinsler *et al*., 2000], a "simple source" is one where kr << 1, where k = 2πf/c is the wavenumber, and r is the radius of the source. Furthermore, a "simple source" is omnidirectional. Approximating the fly to be a sphere of radius r = 1.5mm, the calculation is kr = 0.09 << 1. Therefore, the fly is essentially a "simple source." It can be shown that, when used as a receiver, the directionality of a source is the same. Therefore, the direction finding capabilities of a fly at the frequency of interest would have to be extremely limited if, again, the directionality were achieved solely based on the time difference of arrival of the pressure wave at the surface of the ear.

Facing the fact that Ormia Ochracea does not comply with the calculations above and that it does find the direction of the cricket's song, a mechanism other than simple time difference of arrival must be assumed. Indeed, research on the fly's auditory system reveals that it relies on the relative amplitude of two different modes to determine the direction of incoming sound.

To reveal the underlying mechanics, the main aspects of the fly's auditory anatomy, as well as the simplified model proposed by Miles and his collaborators, are explained in the following paragraph. Chapter III provides additional details concerning Miles' simplified model as they pertain to the MEMS devices designed and fabricated here at NPS.

The auditory system of the fly is behind the head of the insect and below the neck as shown in Figure 1. Two membranes, the prosternal tympanal membranes (PTMs), act as the main sensing system. These two membranes connect through a rod called an "apodeme" [Miles *et al.,* 1995]. The coupling of the PTMs makes the fly capable of distinguishing the direction of sound. When the membrane closer to the direction of sound (ipsilateral) is excited from an incoming wave, oscillation is forced. When the wave arrives at the other membrane (contralateral), which is already in motion because of its coupling to the apodeme, it exerts an additional driving force. The movement of the

contralateral membrane is, therefore, a combination of the direct drive – in this case the incoming wave – and the motion caused by the coupling to the ipsilateral membrane. This combination produces a difference in the amplitude of oscillation between the two membranes that translates into direction through the fly's neural system.

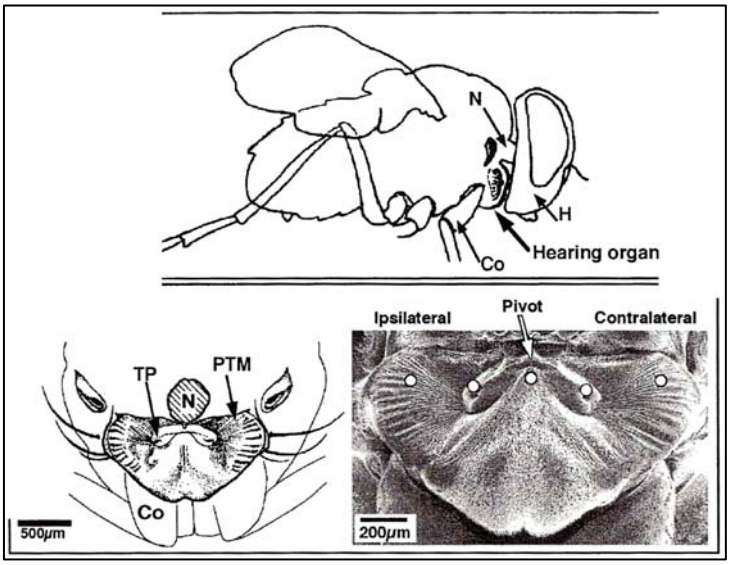

Figure 1. Fly's auditory system (*From*: Miles et al., 1995)

As is always the case in physics, Miles constructed a simplified model to study the physics behind the coupling between the membranes. The model, shown in Figure 2, represents both the oscillating membranes and the coupling between them. At the ends, the two rods connect to a spring-dashpot system and are free to oscillate. The dashpot acts as an absorption mechanism, accounting for losses during the movement of the membranes. The side where the two rods are connected couples through a spring–dashpot system in such a way that they are free to pivot around the connection point. Up and down movement, however, is impossible.

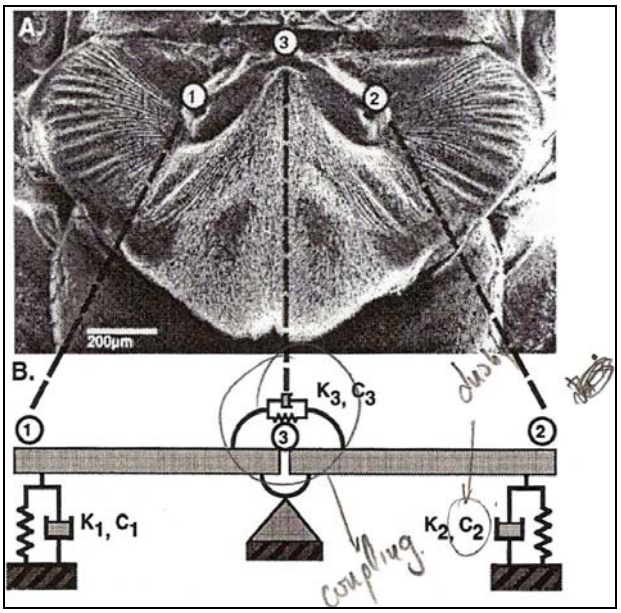

Figure 2. Simple model of the fly's auditory system (*From*: Miles *et al.*, 1995)

B. KARUNASIRI'S BIOMIMICRY WORK

Two NPS thesis students working under the mentorship of Professor Gamani Karunasiri have previously worked on the design, simulation, fabrication, and testing of a biomimetic MEMS device designed to determine the direction of sound based on the principles of the Ormia Ochracea. The first of these was LT Timothy Shivok. For his thesis, he designed, constructed, and tested several "MEMS PolyMUMPs-based Miniature Microphone for Directional Sound Sensing" devices. To predict their frequency response prior to the actual lab testing, he modeled all designs with COMSOL Finite Element Modeling software [Shivok, 2007]. Figure 3 shows a general diagram of one out of the 21 devices constructed. These devices all had small air gaps under the plates.

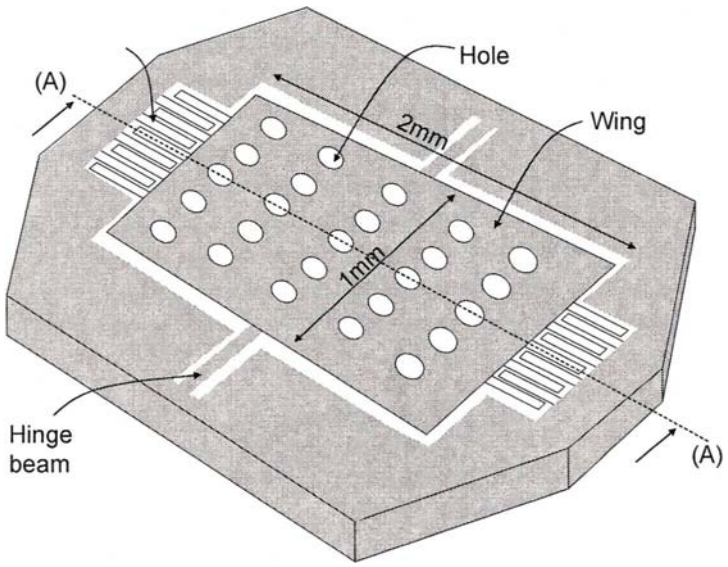

Figure 3. General schematic of MEMS device (*From*: Karunasiri *et al*., 2005)

To minimize an important damping mechanism known as “squeeze film damping,” the plates in these original designs were perforated. This damping mechanism appears in MEMS devices when a plate is vibrating very close to another surface. In squeeze-film damping, the thin film of air under the flaps of the device increases in pressure as the flaps move downward. In the absence of perforations, the air is forced to escape around the periphery of the plate resulting in additional damping. The addition of perforations minimizes the effect of squeeze-film damping with the hope of maximizing the displacement amplitude of the flap vibrations. Test results, however, from this initial work showed that the actual devices presented smaller amplitudes of oscillation than the modeled ones. The main reason for the discrepancy between the simulated and experimental results was assumed to be due to the way in which the affect of the pressure wave on the plates was simulated. Chapter IV will discuss this issue further. Newer experimental results suggest that the low displacement amplitudes for perforated plates previously observed may have been due to manufacturing issues. Future experimental work is being planned to resolve this issue.

As a continuation of Shivok's work with perforated plates, LT Antonios Dritsas worked on MEMS designs with solid plates. The fabrication method for these new sensors was changed to Silicon on Insulator Multi-User MEMS Process (SOIMUMP). Fifteen sensors were fabricated. Two were identical solid plates with a thin slit in the middle. Simulation results matched the experimental measurements for the solid plates quite well. One of the devices with holes was also tested. In contrast to the response of the solid plates, it showed the same disappointingly small amplitudes of vibration as seen in Shivok's work even though the holes were smaller. At this time, no further analysis was made on the devices with holes. Specific details concerning the physics, the construction procedure, the modeling, and other details of the devices is discussed later in this thesis.

Dristas also showed experimentally that the incident angle of an incoming sound wave could be determined from the relative amplitudes of the rocking and bending modes. However, due to the very sharp frequency response and the large difference in resonance frequencies of the two modes, a chirp signal from 2 – 14kHz was required to excite them both.

Several important questions remained at the conclusion of Shivok and Dritsas' work. First, how is the sound pressure to the MEMS device in COMSOL accurately coupled? The simulations run by Shivok and Dritsas applied a force directly onto the MEMS plates based on the pressure of the incoming wave as opposed to coupling the acoustic and MEMS modules. Second, the accuracy of the simulations for the plates with holes needed improvement to match the rather dismal experimental results. This might involve both the acoustic coupling as well as an improvement in the ability of the simulation to model the damping mechanisms. Finally, there is the question raised by Dritsas of how to obtain, in the absence of a known broadband signal, sufficient vibration amplitudes in the two modes to determine sound directionality.

III. THEORY

A. OVERVIEW

To design a MEMS microphone which can reproduce the directionality of Ormia Ochracea, it is necessary to understand both the basic acoustics of sound waves and microphones as well as the physics of the simplified model of the fly's auditory system. This chapter starts, therefore, with an explanation of the basic acoustics of the problem including a discussion of the relationship between pressure and particle velocity in a plane wave, the meaning of the near field and far field of an acoustic sensor, and the factors that determine the directionality of a sensor. The general rule of thumb is that a large sensor is required to achieve good directionality. It considers the conditions under which this rule applies along with an explanation of the key difference in the fly's ear that allows it to achieve a much greater directionality than expected for its size. The discussion of basic acoustics finishes with the role of the quality factor of a microphone in determining its frequency response. The chapter then provides a detailed explanation of the model of the fly's ear proposed by Miles including the additions made by Shivok and Dritsas. Finally, it includes an analysis of the damping mechanisms involved in the MEMS structure.

B. ACOUSTIC CONSIDERATIONS

1. Relationship between Pressure and Particle Velocity

The relationship between the acoustic particle velocity and pressure can be derived using the linearized Euler equation $\rho_0 \frac{\partial \vec{u}}{\partial t} = -\nabla p$, where ρ_0 is the fluid density; p is the sound pressure; and u is the particle velocity. Proper manipulation of this relationship for a single plane wave propagating in the

positive direction results in the following relationship between the instantaneous amplitude of the acoustic pressure and the particle velocity:

$$p = \rho_0 c u$$

The product $\rho_0 c$ is known as the "characteristic acoustic impedance" of the medium in which the sound wave propagates. Its value in air is 415 $\frac{Pa \cdot \sec}{m}$ at 20ºC [Kinsler *et al.*, 2000].

2. The Near Field and Far Field of a Source

The pressure produced at any point in space from a radiating source is a function of the distance to the source. It turns out that the pressure from a source can fluctuate rapidly when close to the source while it falls off smoothly at larger distances. The point at which this transition happens specifies the near and far fields of a source.

The reason for the large fluctuations in pressure amplitude in the near field of a source is the interference produced between waves coming from different points on that source to a specific position in space. Assuming a linear sound source of some length L, consider that any single point on it acts as a point source. The pressure at any position in space is the "summation" of the pressure produced by all the point sources along the length of the sound source. Consider, for example, positions on the perpendicular bisector of the line source. If the position is close to the source, waves transmitted from different locations on the line source arrive with larger time differences – and hence larger phase differences - than they will to positions further away. A physical representation of this appears in Figure 4.

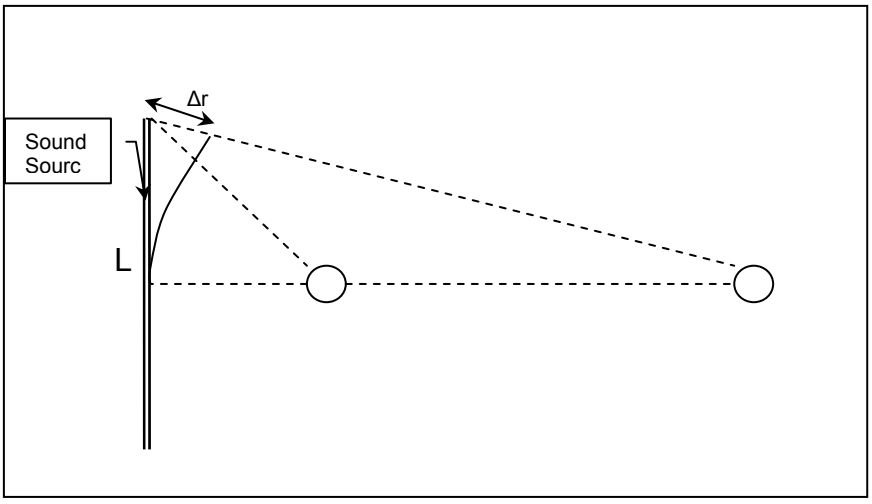

Figure 4. Difference in distance of signals arriving from the center and the end of a line source to two different spatial points.

The phase difference of the two signals arriving at the point is given by:

$$\Delta\phi = \frac{2\pi f}{c}\Delta r = \frac{2\pi}{\lambda}\Delta r \ ,$$

where f is the frequency of the wave, c is the speed of sound, and Δr is the difference in distance. As the distance to the position increases, Δr becomes smaller and so does the phase difference $\Delta\phi$. At a point "sufficiently" far from the source, the phase difference becomes negligible, and the pressure is estimated as the sum of the radiated pressures.

Since it depends on where the phase difference is considered "negligible," the transition distance from the near field to the far field is an approximation. A formula to calculate that distance can be found in Ziomek [1995] as:

$$R = \frac{\pi L^2}{\lambda} = \frac{\pi L^2 f}{c} ,$$

where L is the maximum length of the source; λ is the wavelength; f is the frequency; and c the speed of sound. It is important to note that the "range to far field" is proportional to the length of the source and inversely proportional to the

wavelength. Therefore, the far field of a larger source is farther away than that of a smaller source at any given frequency.

Because of acoustic reciprocity, this analysis is also valid in the case where the source and the receiver are interchanged [Kinsler *et al.*, 2000]. In other words, the pressure is approximately constant along a line receiver for a point source placed sufficiently in its far field.

3. Directionality of an Acoustic Sensor

Once in the far field, the radiated sound field of a source is described by its axial pressure $P_{ax}(r)$, which is only a function of the distance, and a normalized unitless factor known as the "directional factor," $H(\theta,\phi)$, which is a function of the direction. Thus, the amplitude of the pressure is described as:

$$P(r,\theta,\phi) = P_{ax}(r)H(\theta,\phi)$$

The exact form of the directional factor depends on the shape of the source, frequency, and the relative phase of each infinitesimal source element. Its maximum value is unity in the direction at which the pressure is a maximum. On the other hand, the zeroes, or nulls, of the directional factor provide the angles at which no pressure radiates [Kinsler, *et al.*, 2000]. This variation of the amplitude of the source as a function of the angle is known as "directionality." This is an important quantity because it specifies the ability of the source to project sound energy in a specific direction [Urick, 1983]. As an example, the directional factor of a line source can be computed as $H(\theta) = \sin c\left(\frac{1}{2}kL\sin\theta\right)$, where k = ω/c is the wavenumber and L is the length of the source. The quantity $b(\theta,\phi) = 20\log H(\theta,\phi)$ is known as the beampattern and is a measure of the directional factor in dB [Kinsler, *et al.*, 2000]. The directional factor, and thus the beampattern, of a transducer that can operate both as a source and as a receiver is the same.

Between two successive zeroes of the directional factor, the pressure increases from a minimum to a maximum and back to a minimum. The zeroes about the acoustic axis describe the angular limits of the mainlobe of the beampattern. The solid angle of this mainlobe is a measure of the directionality of a source. This solid angle turns out to be proportional to wavelength and inversely proportional to the source aperture. Therefore, the larger the source, the more directional it is. Based on the principle of reciprocity, the whole analysis is valid for the receiver.

4. Time Difference of Arrival

As discussed above, the directionality of a sensor is calculated for a specific frequency, and yet all realistic sounds consist of multiple frequency components. One of the mechanisms by which most animals are thought to determine the direction of a sound lies in detecting the time difference of arrival of the sound as it reaches the two ears. Figure 5 shows a simplified model of the animal ears as two omnidirectional point receivers. The model shows how the time difference of arrival depends on the direction of the sound source.

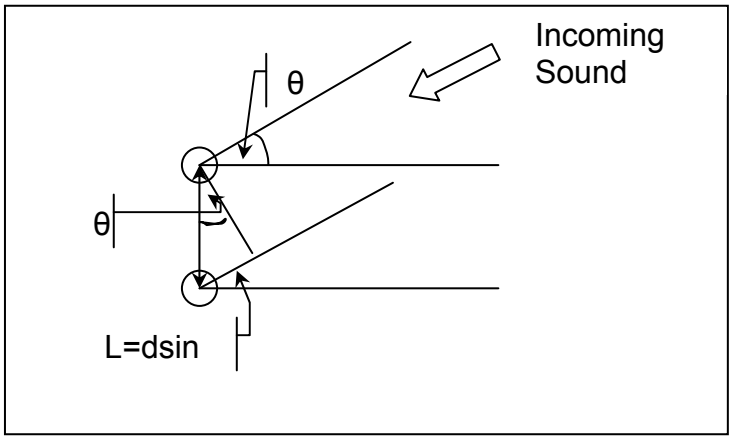

Figure 5. Sound direction determination with the use of two omnidirectional point receivers.

The receiver closer to the sound source receives the signal first. Assuming a plane wave arriving with angle θ relative to the horizontal, the time difference at which the sound arrives at the second receiver can be calculated as $\Delta t = d \sin(\theta)/c$, where d is the distance between the receivers, and c is the speed of sound in the medium.

Animal ears are similar to the two receivers above in the sense that they sense the sound pressure independently from one another (they are not coupled). As the two separate signals process in the brain, the time difference Δt presented above translates into direction. Taking the dimensions of the head to be about 22cm, the time difference Δt for an incoming sound at an angle of 30º would be 0.32ms. The precision with which the brain can accurately determine a direction with this mechanism depends on how large the time difference is as well as the lower limit to the time differences the brain can detect.

There are also other mechanisms involved in the ability of animals to detect sound direction. For example, at frequencies above 1500Hz, the human head essentially blocks an incoming pressure wave. In this case, the strength of the signal arriving at the ear closer to the source is greater than that arriving to the opposite side. Therefore, the direction of sound can be determined based on the relative amplitude of the signal [Smith, 1997].

5. Achieving Greater Directionality with Smaller Sensors

As discussed previously, the directionality of a receiver based on sensing the pressure of an acoustic wave increases with its size. A single receiver can be used to determine the direction of a sound source if it is rotated to different directions until the signal is maximized (If the receiver is stationary, it is not possible to distinguish between a strong source on a sidelobe and a weak source on the mainlobe.) The error in the source direction determined in this way is dependent on both the signal-to-noise ratio (SNR) as well as the width of the mainlobe of the beampattern. To the extent that the SNR is high and the mainlobe small, the error will be low. With two (or more) acoustic pressure

sensors, the time difference of arrival can be used to determine directionality as mentioned above. By using two independent receivers in the sensor, the need for moving the sensor to determine direction is eliminated. However, once again, the smaller the sensor the higher the SNR needs to be to achieve the same accuracy in terms of source directionality.

In the case of the fly, the coupling between the two acoustic membranes, achieved through the apodeme, provides a physical mechanism that "artificially" amplifies the time difference of the signal arrival by a factor of 20 [Miles *et al.*, 1995]. An amplification of the time difference of arrival certainly improves the ability of two receivers to determine directionality.

Another method for determining directionality is based on sensing the acoustic particle velocity instead of the pressure of an acoustic wave. Since velocity is a vector quantity as opposed to a scalar quantity, knowledge of the particle velocity for a single source yields direction without the need for a second receiver. Again, however, SNR is expected to be a determining factor in the accuracy of the method.

6. Quality Factor of a Microphone

The quality factor Q of an oscillating device is defined as the ratio between the resonance frequency divided by the frequency difference of the half power points or:

$$Q = \frac{\omega_{res}}{\omega_{+} - \omega_{-}} \tag{3.1}$$

where ω_{res} is the angular frequency at the maximum power and ω_{+}, ω_{-} are the angular frequencies above and below ω_{res}, respectfully, at which the power amplitude is half of its maximum value. If the value of Q is large, the frequency response curve falls off rapidly and it is considered a "sharp resonance." When it is small, the curve falls off more slowly and it is considered a "broad resonance."

It can be shown that the quality factor is inversely proportional to the damping coefficient of the oscillating system [Kinsler *et al.,* 2000]:

$$Q = \omega_{res} \frac{m}{R_m} \tag{3.2}$$

where m is the mass of the oscillator and R_m is the damping coefficient.

It is obvious from (3.2) that the frequency response curve becomes wider as the damping increases.

Not only can the quality factor provide an estimate of the damping coefficient of the system, but it also determines the maximum amplitude of the velocity. A mode of vibration with low damping (high Q) will have a higher amplitude at any given frequency than one with larger damping.

It must be noted that the resonance frequency corresponds to the maximum velocity amplitude -- not to the maximum displacement amplitude. The maximum displacement amplitude occurs at a frequency $\omega = \sqrt{\omega_{res}^2 - 2\beta}$ where $\beta = \frac{R_m}{m}$, R_m is the damping coefficient and m is the mass of the oscillator [Kinsler *et al.,* 2000]. It turns out nevertheless that the resonance frequencies of the current MEMS design are so high and the damping coefficients so small that there is essentially no difference between the frequency of the maximum velocity amplitude and that of the maximum displacement amplitude. In this work, therefore, the maximum displacement amplitude is used to determine the resonance frequency. This simplifies the comparisons with previous work.

C. THE SIMPLIFIED MECHANICAL MODEL

The model, as created and studied by Miles and then interpreted by Shivok, appears in Figure 6.

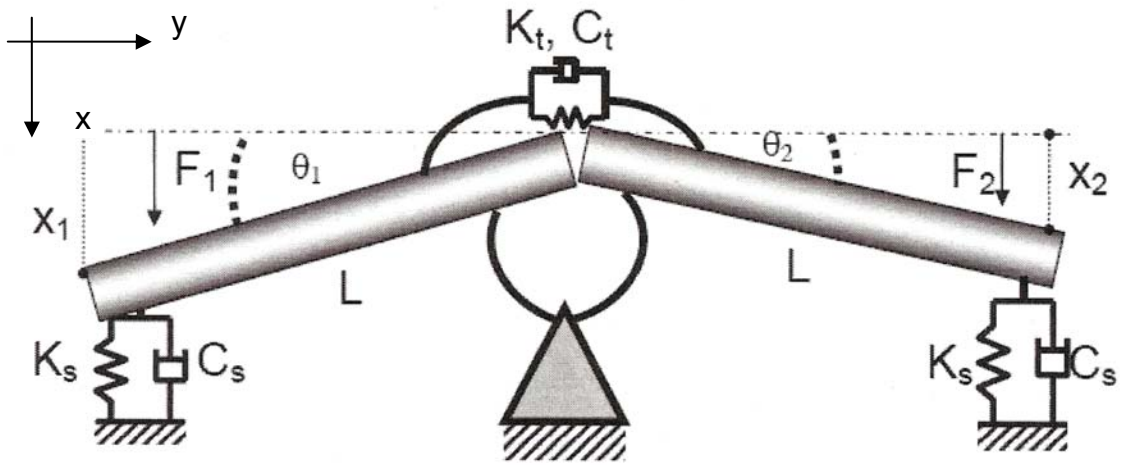

Figure 6. Simplified model of the fly's auditory system (*After*: Shivok, 2007).

It consists of two solid bars coupled in the middle with a torsional spring-dashpot mechanism. At this connection point, the model is clamped in such a way that there cannot be motion in the vertical direction (x-direction). The other two ends of the system are free to move vertically. There is another spring-dashpot system at the end of each bar. The parameter K_s represents the mechanical stiffness and C_s is the damping coefficient at the end of each rigid bar. These parameters are the same for both sides. On the other hand, K_t and C_t are the mechanical stiffness and damping coefficient of the torsional coupling mechanism.

When a force is applied on the bars, its vertical component results in the bar movement. The total displacement of the bars depends on the magnitude and phase of the applied force along each bar as well as on the spring and damping coefficients. The physical importance of the coupling mechanism is made clear by the following observation: If a force is applied on only one of the bars, the other bar will move in a direction opposite to that force due to the coupling provided by the spring – dashpot system. The exact amplitude and phase of that second movement is controlled by the spring and damping

coefficients mentioned above. Experiments conducted directly on the fly's ears [Robert *et al*., 1998] proved this observation. They showed that the excitation of only one of the membranes resulted in the movement of the other.

There are two degrees of freedom in this mechanical model. This means that the calculation of two parameters is required to describe its behavior. These two parameters can be either the displacement of the two free edges, x_1 and x_2, or the angle between the moving bars and the horizontal, θ_1 and θ_2. An important consequence of having a mechanical model with two degrees of freedom is that there will be two natural frequencies or normal modes of oscillation (resonance frequencies) when the system is forced into oscillatory motion.

The equations of motion, as they appear in Miles *et al.,* [1995], are as follows:

$$\begin{bmatrix}\begin{pmatrix} k_1+k_3 & k_3 \\ k_3 & k_2+k_3 \end{pmatrix}\end{bmatrix}\begin{bmatrix} x_1(t) \\ x_2(t) \end{bmatrix}+\begin{bmatrix}\begin{pmatrix} c_1+c_3 & c_3 \\ c_3 & c_2+c_3 \end{pmatrix}\end{bmatrix}\begin{bmatrix} \dot{x}_1(t) \\ \dot{x}_2(t) \end{bmatrix}+\begin{bmatrix}\begin{pmatrix} m & 0 \\ 0 & m \end{pmatrix}\end{bmatrix}\begin{bmatrix} \ddot{x}_1(t) \\ \ddot{x}_2(t) \end{bmatrix}=\begin{bmatrix} f_1(t) \\ f_2(t) \end{bmatrix} \quad (3.3)$$

where m is the mass of each bar, k_1 and k_2 are the mechanical stiffnesses; c_1, c_2 are the damping coefficients of the bars; k_3, c_3 the mechanical stiffness and damping coefficient of the coupling mechanism; $f_1(t), f_2(t)$ are the forces applied on the left and the right bar; and $x_1(t), x_2(t)$ are resultant amplitudes of oscillation. The objective of the problem is to calculate the amplitude of oscillation from the other parameters. Assuming that the two bars are geometrically and materially the same, $k_1 = k_2 = k_s$ and $c_1 = c_2 = c_s$ are substituted. To be consistent with Shivok's treatment, this research set $c_3 = c_t$ and $k_3 = k_t$. Thus, the equation (3.3) becomes:

$$\begin{bmatrix}\begin{pmatrix} k_s+k_t & k_t \\ k_t & k_s+k_t \end{pmatrix}\end{bmatrix}\begin{bmatrix} x_1(t) \\ x_2(t) \end{bmatrix}+\begin{bmatrix}\begin{pmatrix} c_s+c_t & c_t \\ c_t & c_s+c_t \end{pmatrix}\end{bmatrix}\begin{bmatrix} \dot{x}_1(t) \\ \dot{x}_2(t) \end{bmatrix}+\begin{bmatrix}\begin{pmatrix} m & 0 \\ 0 & m \end{pmatrix}\end{bmatrix}\begin{bmatrix} \ddot{x}_1(t) \\ \ddot{x}_2(t) \end{bmatrix}=\begin{bmatrix} f_1(t) \\ f_2(t) \end{bmatrix} \quad (3.4)$$

A similar equation could have been obtained from solving for the angles θ_1 and θ_2 generated between the moving bars and the horizontal.

Solution of the above equations for the resonance frequencies can be achieved by solving for the eigenvalues of the system assuming periodic excitation. Specific details of the method can be found in Taylor [2005]. The resultant eigenvalues, which can also be referred to as normal modes of oscillation or resonance frequencies, are, as expected, two. They were calculated by Miles to be:

$$\omega_r = \sqrt{\frac{k_s}{m}} \quad (3.5) \qquad \text{and} \qquad \omega_b = \sqrt{\frac{k_s + 2k_t}{m}} \quad (3.6)$$

These two normal modes correspond to two different motions of the model. The movement of the two bars that corresponds to the first normal mode is one where the two bars move exactly out-of-phase (180º phase difference). In other words, one of the bars moves upwards while the other moves downwards with approximately the same amplitude of oscillation. This movement is known as the "rocking mode," and the resonance frequency is ω_r. On the other hand, the second normal mode results in the two plates moving in the same direction (upwards or downwards) with approximately the same amplitude and is referred to as the "bending mode" (Figure 7). The angular frequency of the bending mode is ω_b. All movement of the model can be described as a combination of the rocking mode and the bending mode [Miles *et al.*, 1995].

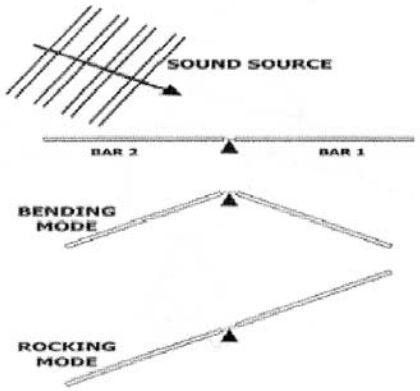

Figure 7. Rocking and bending modes of the mechanical model (*From*: Robert *et a*l., 1996).

In the case of a MEMS device, the only change that has to be made to the described physical model is to substitute the two bars with either solid or perforated plates. Because of its small size, when the sound from a distant source is incident on the device, the pressure amplitude at both sides of the device is essentially the same. Therefore, if the source is sufficiently far away, the amplitude of the incident pressure on the surface of the receiver is approximately constant - just as it would be in the case of a plane wave. More details on the approximation required will be provided in the modeling chapter of the thesis.

Figure 8 shows a diagram of a plane wave incident on the device at an angle of θ relative to a plane normal to the device through its midsection. Because it is a plane wave, the pressure on both sides will be very close. There will be a small difference in the time of arrival.

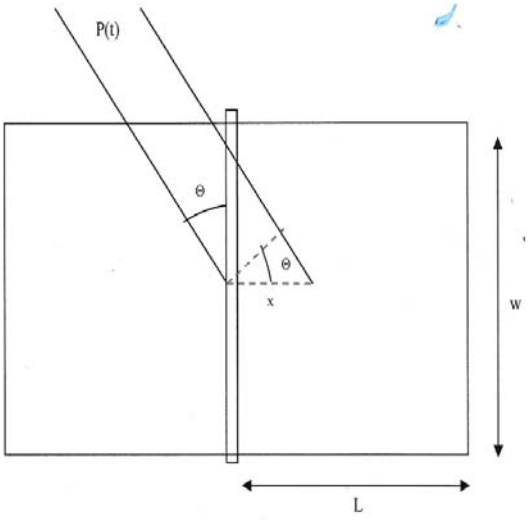

Figure 8. Incident pressure wave on the MEMS device. (*From*: Dritsas, 2008).

Assuming a pressure wave of the form $P(t) = P\sin(\omega t)$, the corresponding pressure on the ipsilateral (closer) plate can be expressed as:

$$P_1(t) = P\sin(\omega t + \omega\tau/2)$$

while the pressure on the contralateral (farther) plate is:

$$P_2(t) = P\sin(\omega t - \omega\tau/2),$$

where τ is the time delay in the arrival time between the two plates; ω is the angular frequency of the sound; φ is the angle of incidence; and x is the distance from the center of the device. For a source sufficiently far away, the time delay can be approximated as $\tau = x\sin(\phi)/c$.

The resulting amplitudes of oscillation were calculated by Miles *et al.,* [1995] and then modified by Shivok [2007] using the damping coefficients γ_r, γ_b:

$$x_1(t) = A_b\sin(\omega t + \phi_b) + A_r\cos(\omega t + \phi_r)$$
$$x_2(t) = A_b\sin(\omega t + \phi_b) - A_r\cos(\omega t + \phi_r)$$

for the ipsilateral and the contralateral plate respectfully, where

$$A_r = \frac{Ps}{m}\left(\frac{\sin(\omega\tau/2)}{\sqrt{(\omega_r^2-\omega^2)^2+(\gamma_r\omega)^2}}\right) \tag{3.7}$$

is the rocking mode response amplitude and

$$A_b = \frac{Ps}{m}\left(\frac{\cos(\omega\tau/2)}{\sqrt{(\omega_b^2-\omega^2)^2+(\gamma_b\omega)^2}}\right) \tag{3.8}$$

is the bending mode response amplitude. The phase constants, ϕ_r and ϕ_b, are given by $\phi_r = -\arctan\left(\frac{\gamma_r\omega}{(\omega_r^2-\omega^2)}\right)$ and $\phi_b = -\arctan\left(\frac{\gamma_b\omega}{(\omega_b^2-\omega^2)}\right)$; the damping coefficients, γ_r and γ_b. are given by $\gamma_r = \frac{2c_s}{m}, \gamma_b = \frac{2(c_s+2c_t)}{m}$. As before, ω_r and ω_b are the rocking and bending mode resonance frequencies. Likewise, m and s are the mass and area of the plate and P is the amplitude of the incident pressure wave.

If the frequency of the incident wave is equal to the resonance frequency of either the rocking or bending mode, Equations (3.7) and (3.8) above become:

$$A_r = \frac{Ps}{m}\left(\frac{\sin(\omega\tau/2)}{\gamma_r\omega}\right) \tag{3.9}$$

$$A_b = \frac{Ps}{m}\left(\frac{\cos(\omega\tau/2)}{\gamma_b\omega}\right). \tag{3.10}$$

To calculate the angle of incidence in the case of a MEMS sensor implementing those principles, Dritsas experimentally measured the amplitude response of the device at both the resonance frequencies simultaneously. Proper manipulation of equations (3.9) and (3.10) provided the following formula for direction determination:

$$\sin(\theta) = 2\frac{P_b}{P_r}\frac{\gamma_r}{\gamma_b}\frac{1}{\omega_b}\frac{c}{x}\frac{A_r}{A_b} \tag{3.11}$$

where P_b, P_r are the pressure amplitudes at the bending and rocking modes respectively; c is the speed of sound; x is the distance between the stress application points that, as was proved by Dritsas [2008], are the midpoints of the two plates; and A_r, A_b are the measured amplitudes. The experimentally measured values resulted in the correct determination of the incidence angle within experimental error [Dritsas, 2008].

D. AIR DAMPING

One particularly important factor that must be considered in the construction of a MEMS device is air damping. Air has a low viscosity. It contributes very little to the damping of oscillatory devices that are large -- as long as the velocity of oscillation is small. However, when the dimensions are decreased to that of the MEMS device described above, air damping can have a substantial effect on the displacement amplitudes.

In a study on the effect of air damping on the "miniaturization" of oscillatory devices, Newell [1968] divided the pressure of the incident sound field into three regions:

In the first region, the air pressure is so low that there is essentially no interaction between the air molecules and the device. Therefore, the air damping in that region in negligible and the only damping mechanism of importance is the damping due to the construction material.

In the second region of increased pressure, the air molecules interact with the device. They exchange momentum and energy with it, but they do not interact with each other. In this region, air damping becomes very important and is proportional to the velocity of the device with respect to the air as well as the ambient air pressure.

The third region is where the pressure has increased so much that the molecules interact with both the device and themselves. This interaction causes the air to act as a viscous fluid. Nevertheless, viscosity does not depend on pressure. Therefore, the air damping in this region is independent of the pressure. Newell calculated the quality factor of a cantilever vibrating in the third region to be: $Q = \left[\frac{(Y\rho)^{\frac{1}{2}} w}{24\mu}\right]\left(\frac{d}{L}\right)^2$, where ρ is the fluid density; Y is the Young's modulus; μ is the fluid viscosity; and L, d, w are the length, the thickness, and the width of the cantilever respectfully. By comparing the expression for the expected quality factor in regions 2 and 3, Newell calculates that cantilevers narrower than 0.4μm fall in the third region of air damping at atmospheric pressure. An additional damping mechanism exists when an inflexible surface is placed close to the resonator. In this case, air must escape through the sides as the resonator moves downwards. If there is a plate located at distance h from the cantilever, the expression for Q becomes: $Q = \left[\frac{(Y\rho)^{\frac{1}{2}}}{24}\frac{w}{\mu}\right]\left(\frac{d}{L}\right)^2\left(\frac{h}{w}\right)^2$. The smaller the distance between the resonator and the surface, the more damping [Newell, 1968].

The three regions of damping described above depend on both the pressure and the ratio of length versus thickness of the device in question. The quality factor in Figure 9 identifies these figures. Taking into account the dimensions described above for this work's device, the following ratio results:

$$\frac{L}{d} = \frac{2x10^{-3}m}{10x10^{-6}m} = 200.$$

This result, together with the fact that the devices operate at atmospheric pressure, suggests that the MEMS designs of the Karunasiri group operate in the third damping region.

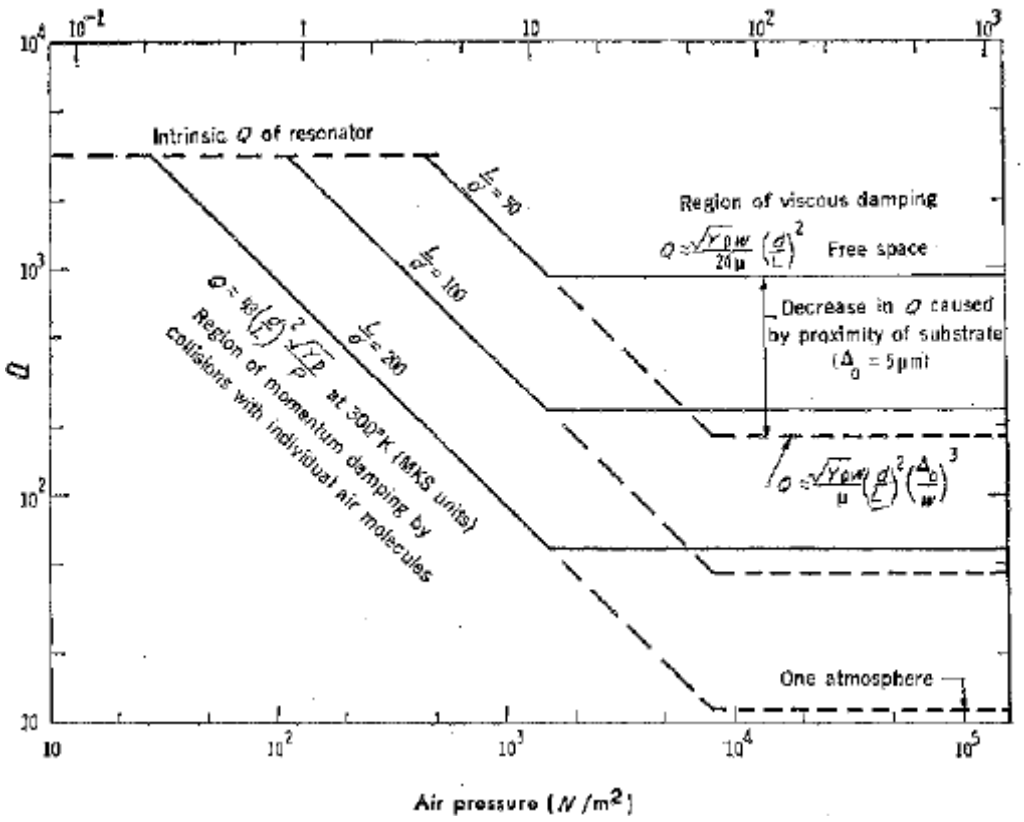
Intrinsic Q of resonator
Region of viscous damping
Free space
Decrease in Q caused by proximity of substrate
One atmosphere
Region of momentum damping by collisions with individual air molecules
at 300°K (MKS units)
Q
Air pressure (N/m²)

Figure 9. Variation of quality factor with air pressure for resonators having various length to thickness ratios for both free space and squeeze-film damping (*From*: Newell, 1968).

Following Newell's work, Zhang and Turner [2006] proposed a model for calculating the damping coefficient for "beam type resonators" as shown in Figure 10.

A linear damping force is opposite to the direction of movement and proportional to the velocity. For an extended object, such as the resonator, Zhang and Turner use the damping force per unit length, i.e.,:

$$F = c_{damping} u \tag{3.12}$$

where F is the force per unit length; u is the velocity of the motion; and $c_{damping}$ is the damping coefficient per unit length that must be determined for the each specific case examined.

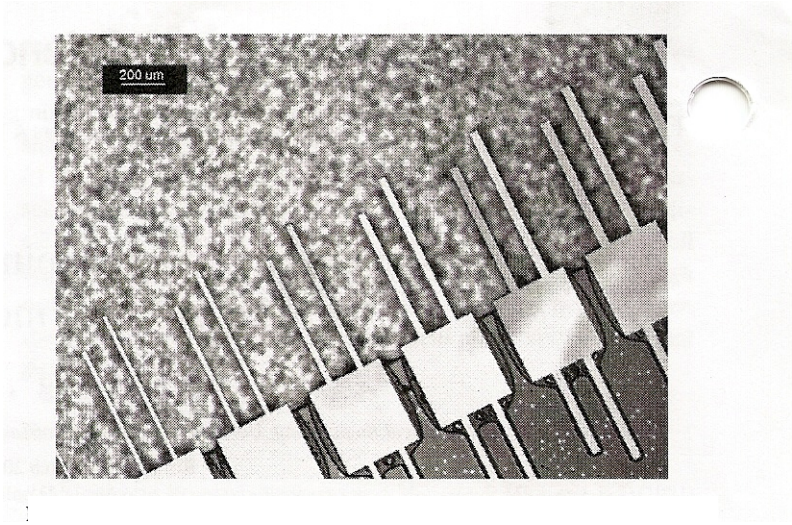

Figure 10. Silicon cantilevers with different dimensions used by Zhang to determine air damping (*From*: Zhang *et al.*, 2006).

Since the damping coefficient is observed to depend on both the resonance frequency and on the width of the device, the damping force was assumed to be of the form:

$$F = \pi \mu u f \tag{3.13}$$

where μ is the viscosity of the fluid; u is the velocity; and f is a dimensionless parameter that depends on the resonance frequency ω, the width of the cantilever, the fluid density ρ, and the viscosity μ.

Equation (3.12) can be rewritten as:

$$c_{damping} = \frac{F}{u} \tag{3.14}$$

Combining this with equation (3.13) and using dimensionless fluid analysis, Zhang concluded that the damping coefficient can be written in the form:

$$c_{damping} = \pi\mu(\alpha + b\lambda) \tag{3.15}$$

where λ is the dimensionless parameter $\lambda = \frac{width}{\delta}$; δ is a characteristic length used in the dimensional analysis procedure defined as $\delta = \sqrt{\frac{2\mu}{\rho\omega}}$; and α, b are unknown dimensionless parameters that were determined using both experimental measurements and simulation results from COMSOL software (Figure 11).

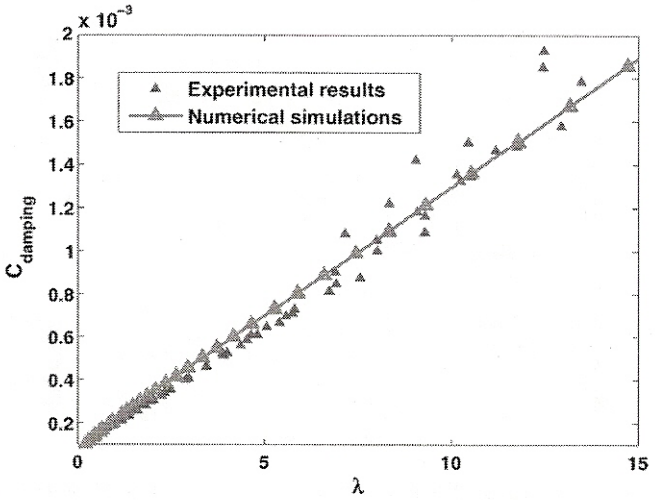

Figure 11. Experimental and numerical results justifying the linear model for the damping coefficient in equation (3.15) (*From*: Zhang *et al.*, 2006).

For high resonance frequencies the parameter bλ>>α in equation (3.15). This is because $\delta \propto \sqrt{\frac{1}{\omega}}$ and, thus, $\lambda \propto \sqrt{\omega}$. Therefore, as the frequency increases, bλ gets larger and so $(\alpha + b\lambda) \approx b\lambda$. The damping coefficient then becomes:

$$c_{damping} \approx b\lambda\pi\mu \tag{3.16}$$

The b parameter was calculated using numerical analysis (COMSOL) to be $b \approx 2$. It was also found to be independent both of the shape of the cross section of the cantilever (Figure 12) and the thickness of the cantilever -- as long as the width-to-thickness ratio was greater than 5 [Zhang *et al.*, 2006]. A direct comparison of that formula for the damping coefficient and that given by Newell, ($c_{damping} \approx 24\mu$), shows that both are directly proportional to the viscosity of the fluid μ. Furthermore, (3.16) extends the previous concept to include the excitation frequency. Using that formula in conjunction with (3.14) and the values for λ and δ, the damping force per unit area can be expressed as:

$$F = \pi u \sqrt{2\rho\omega\mu} \qquad (3.17)$$

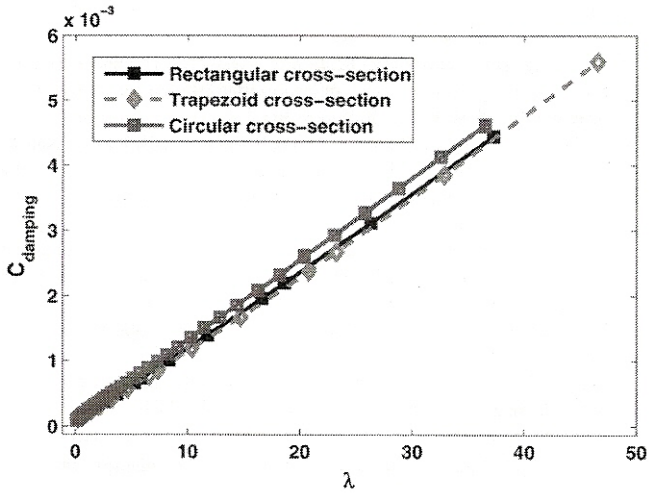

Figure 12. Damping coefficient for various cross sections (*From*: Zhang *et. al.*, 2006).

The above equation for the damping force per unit length can be applied to the design of the solid plate Karunasiri MEMS devices with no backing. This is because both the vibration mode and the physical dimensions correspond to the assumptions made by Zhang. Furthermore, the lowest resonance frequency calculated corresponds to the rocking mode and is on the order of Khz. Thus, the

assumption that bλ>>α is also valid. Therefore, using (3.17) in this thesis model should provide a reasonable approximation of the damping force on the device. In applying this equation, however, for a device that is oscillating as a result of an incoming acoustic wave, it is important to note that the velocity, u, must be calculated as the **difference between the acoustical particle velocity and the plate velocity.** In other words, the relative velocity between the plate and the surrounding air determines force. This is an important point because it predicts that the acoustic particle velocity will exert a force on the plate in the direction of air movement until the plate velocity exceeds the velocity of the surrounding air molecules. Thus the force on the plate is more properly described as a drag force as opposed to a damping force to the extent that the plate velocity is less than the velocity of air moving past it.

E. RESONATOR CAVITIES

A Helmoltz resonator is an acoustic system that consists of a cavity of volume V surrounded by rigid walls. The cavity communicates with the environment through a circular neck of radius α, length L, and area S. The importance of a Helmholtz resonator is that if it is driven at its resonance frequency it essentially acts as a pressure amplifier. In other words, the pressure inside the cavity is higher than the driving pressure [Kinsler *et al.*, 2000].

The resonance frequency of a Helmholtz resonator is given by:

$$\omega_0 = c\left(\frac{S}{L'V}\right)^{1/2} \tag{3.18}$$

where c is the speed of sound in the medium, L' is effective length of the resonators neck, V is the volume of the cavity, and S is the cross-sectional area of the neck. The effective length has various edge corrections depending on how it is terminated. It is given by:

$L' = L + 1.7\alpha$ when the neck edge is flanged.

$L' = L + 1.4\alpha$ when the neck edge is unflanged.

$L' = L + 1.6\alpha$ when the neck edge is a circular hole.

It turns out that the shape of the resonator is not important as long as the dimensions of the cavity are much smaller than a wavelength. The resonance frequency, however, is sensitive to the geometry of the neck. Therefore, the resonance frequency provided above is only an approximation for geometries where the neck does not have a uniform circular cross-section. The pressure amplification ratio of a Helmholtz resonator is given by:

$$\frac{P_c}{P} = Q = 2\pi \left[V \left(\frac{L'}{S} \right)^3 \right]^{1/2} \tag{3.19}$$

where P_c is the pressure amplitude inside the resonator; P is the ambient pressure amplitude; and Q is the quality factor of the resonator [Kinsler *et al.*, 2000].

Because of the ability of a Helmholtz resonator to amplify sound pressures, it can be considered as a candidate for increasing the amplitude of oscillation for a MEMS device mounted on its opening.

IV. DESIGN DETAILS OF PREVIOUS NPS MEMS SENSORS

A. MEMS DESIGN AND CONSIDERATIONS

As mentioned previously in the "Background" chapter, NPS Professor Karunasiri and students, LT's Shivok and Dritsas, designed, built, modeled, and tested MEMS devices to mimic the membranes of the fly's ear.

Initial designs were based on the PolyMUMPs procedure and their main characteristic was that the two plates of the device were perforated. The primary construction material for the plates was silicon (Si). These plates were mounted on a silicon substrate. The details of the construction procedure appear in Shivok's 2007 thesis while an example of a device structure is shown in Figure 13. A number of devices were constructed. They differed in size, dimensions of the holes, and shape. All devices were placed together on a single chip for ease in testing. Although the resonance frequencies agreed fairly well, the experimental amplitude of oscillation for the perforated devices turned out to be much smaller than expected. Shivok attributed the discrepancy between the simulated and experimental amplitudes to the communication of the acoustic pressure to the back side of the plates through the holes [Shivok, 2007].

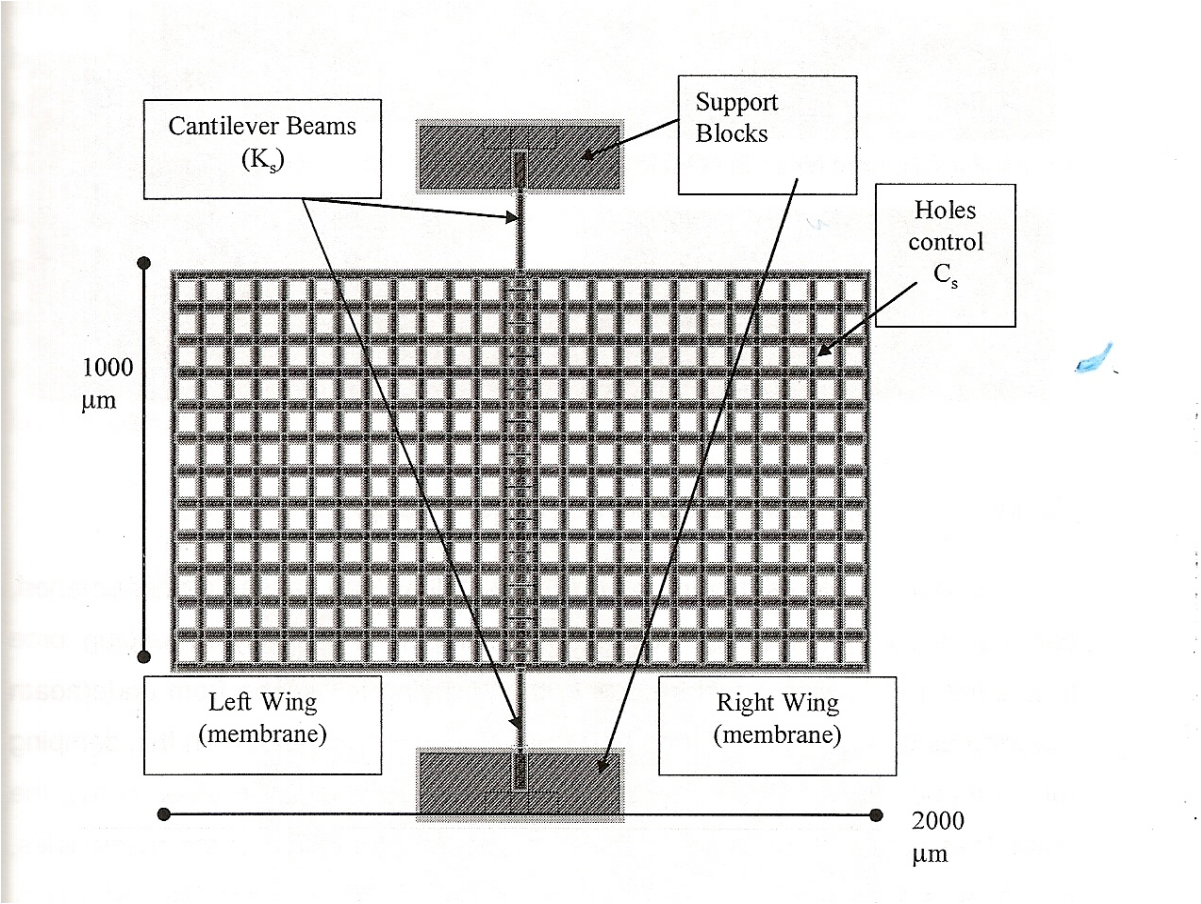

Figure 13. Initial design of a perforated MEMS device based on the PolyMUMPs' construction procedure (*From*: Shivok, 2007).

To increase the amplitude of oscillation and further explore the reason for the discrepancy between simulation and experiment, the next design focused on plates with solid plates. The construction procedure was based on the SOIMUMPs fabrication process that is described by Dritsas [2008]. An important difference from the previous design was that the substrate behind the plate was completely removed to reduce air damping. Again, the main material used for the device was silicon. Fifteen devices were again placed upon a single chip (Figure 14) to be tested in a sound field. Two identical devices, which had solid plates and a slit in the middle, exhibited resonance frequencies for the bending and rocking modes which were within 10% of the predicted values. The vibration

amplitudes were on the same order of magnitude as the values predicted by COMSOL and, as hoped, substantially higher than seen for the previous perforated plates. A large discrepancy (slightly more than a factor of two) in the amplitude of the rocking mode between the two sensors was noted. The cause, however, of this discrepancy was not clear and may have been due to small differences in the devices.

Despite the fact that squeeze-film damping was not an issue due to the lack of a backing, other sensors were constructed with holes of various sizes etched into the plates. In an attempt to increase the vibration amplitude, these holes were made smaller than in previous designs. Simulations were conducted in COMSOL using the same basic technique as Shivok, i.e. using the analytically calculated force of the sound on the sensor plates. To account for the damping in the unbacked plates, Dritsas used damping equations published by Zhang and Turner [2006].

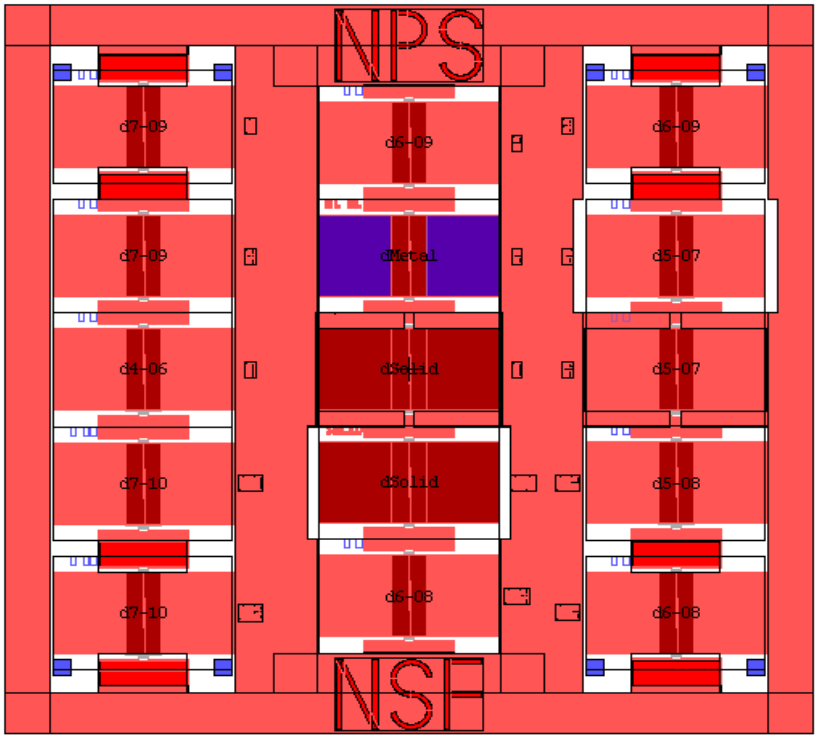

Figure 14. Latest chip layout composed of 15 sensors of different design. (*From*: Dritsas, 2008)

Since this thesis focuses on these solid plate devices, their physical characteristics will be discussed in greater detail. A graphical representation of Device #8, the primary design with solid plates to be tested, appears in Figure 15. Device #11 is identical to Device #8. As previously stated, the device has solid plates with dimensions 1mm x 1mm and a thickness of 10μm each and they are made of silicon. The type of construction material provides the physical property of the wing's stiffness, k_s. This physical property, together with the physical dimensions of the plates that account for the total mass, is the determining factor for the frequency of the rocking mode as given by equation (3.5).

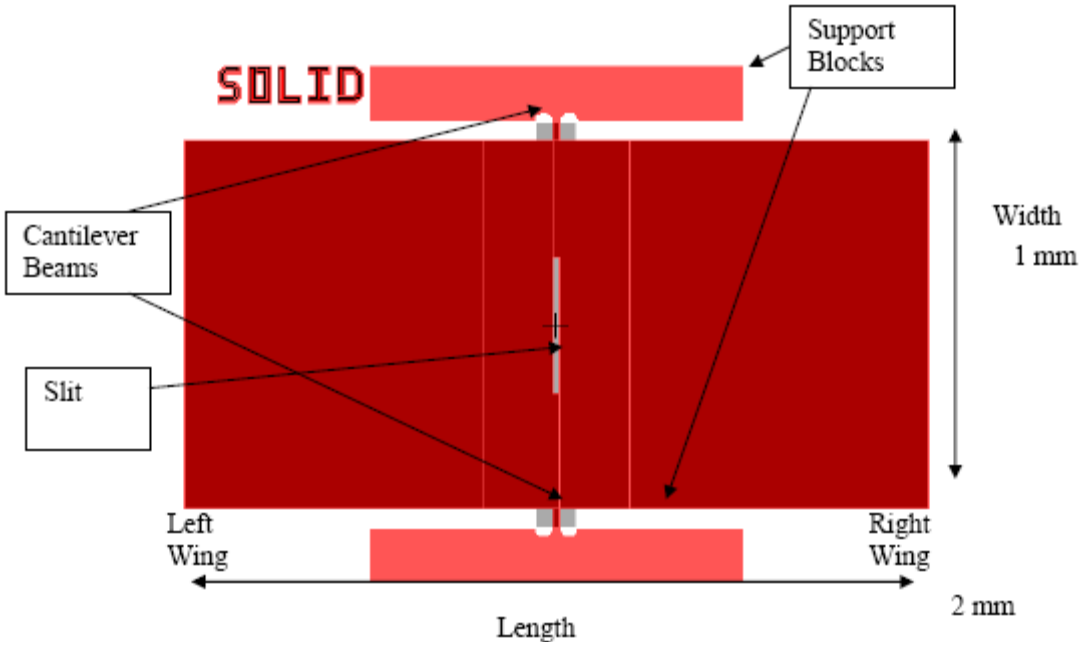

Figure 15. Device #8 - Solid plate design with slit in center (*From*: Dritsas, 2008).

The two solid plates connect to each other through a beam that is contiguous at both ends with 400 μm support blocks that are also made of silicon (Figure 16). The torsional stiffness of the beam, which depends on the construction material and the beam's dimensions, accounts for the coupling stiffness, k_t. This stiffness, together with the wing stiffness k_s discussed

previously and the total mass, account for the bending mode resonance as derived in equation (3.6). As shown in Figure 15, there is a slit in the cantilever beam. This controls the torsional stiffness and, therefore, the bending mode resonance frequency as given by equation (3.6). The dimensions of the slit for Device #8 were 370μm x 20μm.

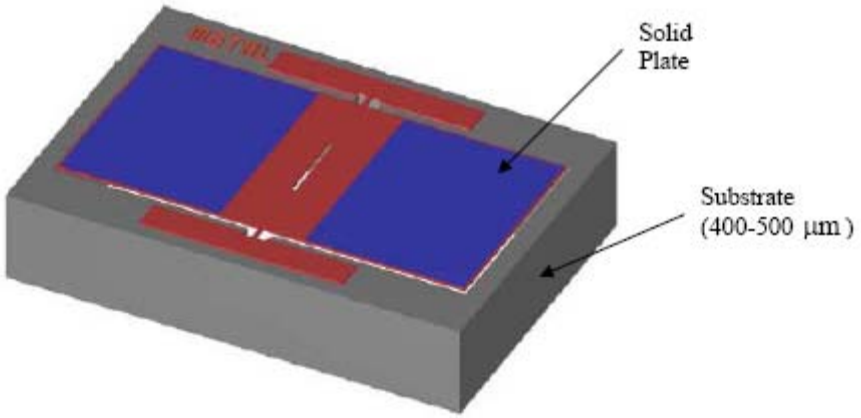

Figure 16. Device with removed substrate and the support structure (*From*: Dritsas, 2008).

The behavior of the device in the rocking and bending mode frequencies appear in Figures 17 and 18 (from COMSOL simulation program). As expected, in the rocking mode frequency, the two plates move with approximately the same amplitude, but they are 180º out-of-phase. On the other hand, when in the bending mode frequency, the two plates have approximately the same amplitude and are in-phase. Experimental measurements conducted by Dritsas [2008] on the device in question showed reasonably good agreement with both theory and simulation both in the resonance frequencies and displacement amplitudes.

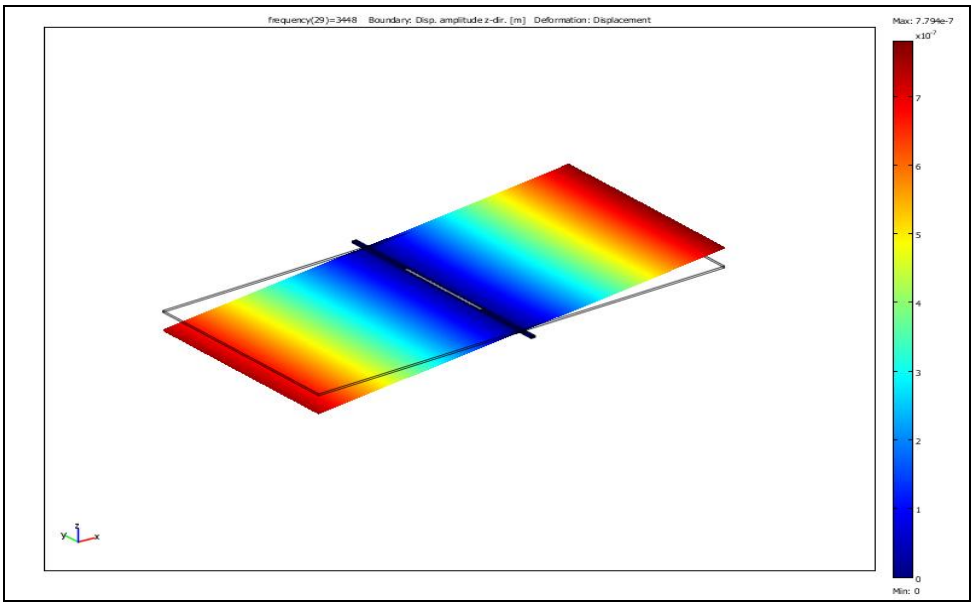

Figure 17. Rocking mode of oscillation.

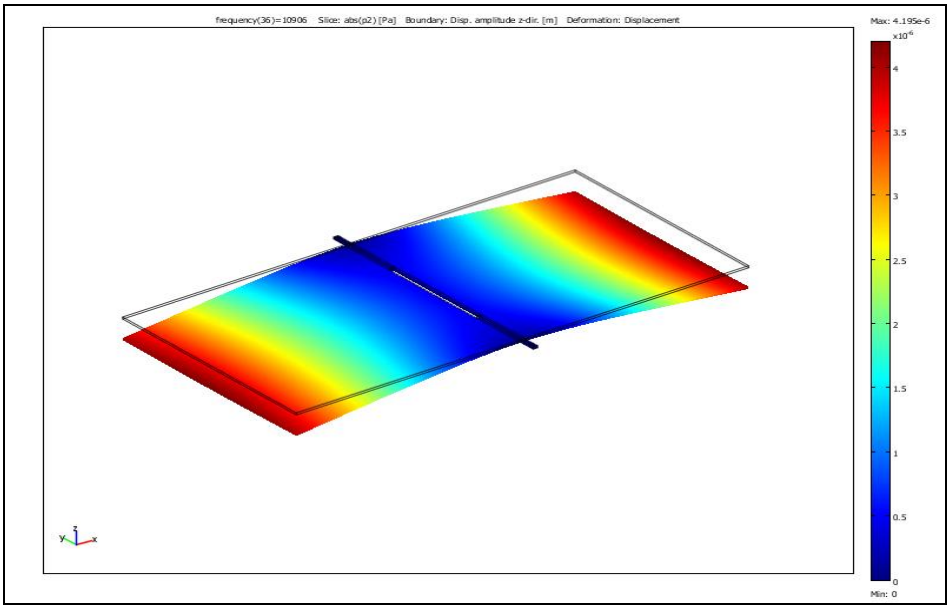

Figure 18. Bending mode of oscillation.

V. MODELING - SIMULATION

A. OVERVIEW

The physical behavior of a MEMS device mimicking the principles of Ormia Ochracea can be investigated using simulations. The results of the simulation can provide verification concerning the validity of the physical assumptions made in defining the model. Furthermore, simulations can be used to help determine the design parameters that will optimize the device performance thus minimizing the time, effort, and expense required to construct and test an actual device. As in the previous theses of LT's Shivok and Dritsas, the software selected to perform these simulations is "COMSOL Multiphysics."

The initial aim of the simulations was to reproduce the results achieved by Dritsas [2008] using an acoustics coupled model. Two different approaches were used to achieve this. In the first approach, the acoustic domain is defined as a rectangular box. One of the sides is defined as a radiating source. This technique should simulate a plane wave incident upon the device. It seemed impossible, however, to eliminate reflections from the boxes sides and/or bottoms. Following that unsuccessful attempt, a sphere was used for the acoustics domain in conjunction with a radiating point source. The calculated sound pressure was applied only on the top of the device, while the same damping term as Dritsas is used was applied to the bottom. This spherical model eliminated boundary reflections better than the former approach and managed to reproduce successfully the simulation results of the non-acoustic coupled simulation.

The next step was to implement a more realistic set of boundary conditions i.e., apply the calculated pressure incident upon the device, both at the top and the bottom of the plate. In addition to that, the damping term was modified to be proportional to the difference between the velocity of the device plates and the sound wave particle velocity. This model produced results reasonably close to those produced by Dritsas. Using this same approach, the

acoustic coupled simulation was conducted for a perforated plate to show that the oscillation amplitude is significantly reduced. The reduction is more than would be expected from the smaller effective solid area of the plates due to perforation. Finally, in an attempt to maximize the oscillation amplitude, a design where the device is mounted on the top of a resonant cavity was simulated. The results present a significant increase in the oscillation amplitudes when tested under the same boundary conditions mentioned above.

B. COMSOL SOFTWARE

1. Basic Simulation Procedure and Parameters

To achieve a better understanding of the simulation results and the underlying physics, it is important to describe the basics of COMSOL Finite Element Modeling software version 3.4.

COMSOL is available in various “modules”, each one covering a specific area of physics. The modules used in this work were:

1. Acoustics Module
2. MEMS Module

The basic process required to perform a simulation is the same for both modules. It is performed in Windows where the various parameters are set:

1. The first step is to select the modeling geometry (either 2-D or 3-D) and the “application modes” for the field of physics required to solve the problem. Figure 19 shows this.

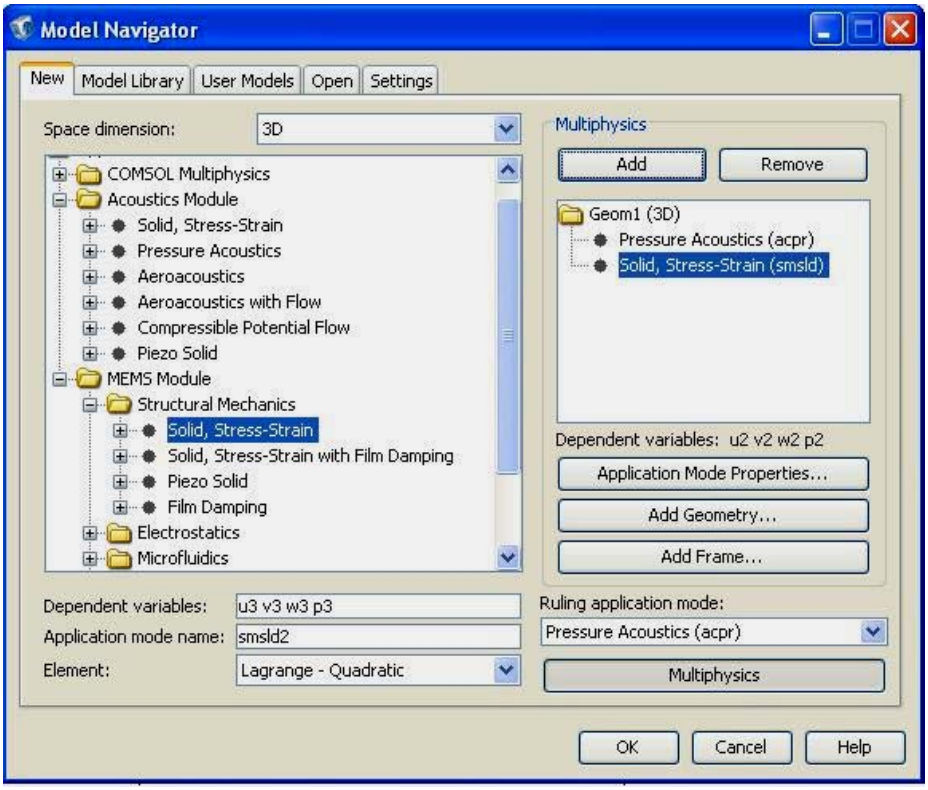

Figure 19. Application mode selection used in COMSOL simulations.

The parameters selected are both 2-D and 3-D geometry, Acoustic Module->Pressure Acoustics -> Frequency Response and MEMS Module -> Structural Mechanics -> Solid Stress-Strain.

2. The next step is to draw the object that needs to be modeled, i.e., the MEMS device. In the beginning, because it is both easier and more precise, the model is drawn in 2-D. Then, because the physical behavior of this device in space is required, the model is "extruded" in a 3-D geometry. Having finished with the MEMS model, the "Acoustics Domain," within which the model resides, must be drawn. As previously discussed, the Acoustics Domain was either a sphere or a box. The size and the shape of the Acoustics Domain affects both the time required to solve the problem as well as the type of sound waves used.

3. Following the design of a model, the physical conditions for each "subdomain" must be established. This includes the determination of the

construction materials for the MEMS device, silicon (Si) and the substance filling the acoustics domain -- in this case, air (Figure 20). These general choices remained unchanged in all the acoustic coupled simulations.

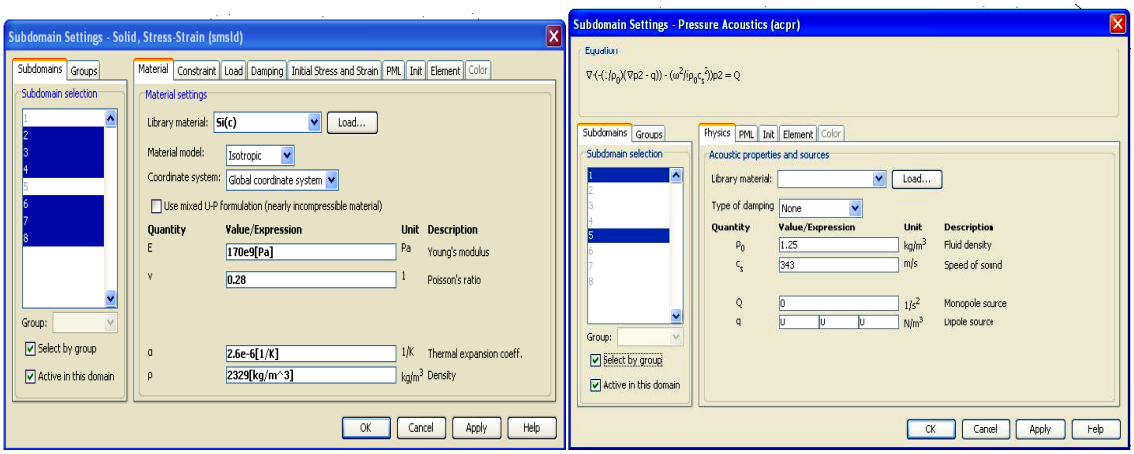

Figure 20. Subdomain settings for solid stress-strain and pressure acoustics application modes.

Moreover, the boundary conditions for every surface drawn must be established. This would include which boundaries are fixed, which are free, what is the condition of the acoustic domain at the boundary, and what is the load on each boundary, etc. The determination of each specific boundary condition must be carefully examined to represent the real conditions as closely as possible.

4. It is the meshing of the model that comes next. Meshing is the procedure of splitting the drawn space into small finite elements (Figure 21). The specific equations that apply in each domain are determined by the selections made in the previous step. They are solved individually for each of the small elements of the mesh, and the results are used as inputs for the following element. Meshing is a “give and take” procedure. The smaller the mesh size (more elements used), the more precise the numerical calculations. On the other hand, increasing the mesh size increases the time required for the software to reach a solution. Thus, a compromise must be made between a mesh size that provides accurate enough results and a reasonable solving time. Care must be

taken to fulfill the minimum requirements of the software to produce a physically valid result. In the case of the Acoustic Domain, at least five mesh elements per wavelength must be used. Thus, the mesh size also depends on the frequencies involved.

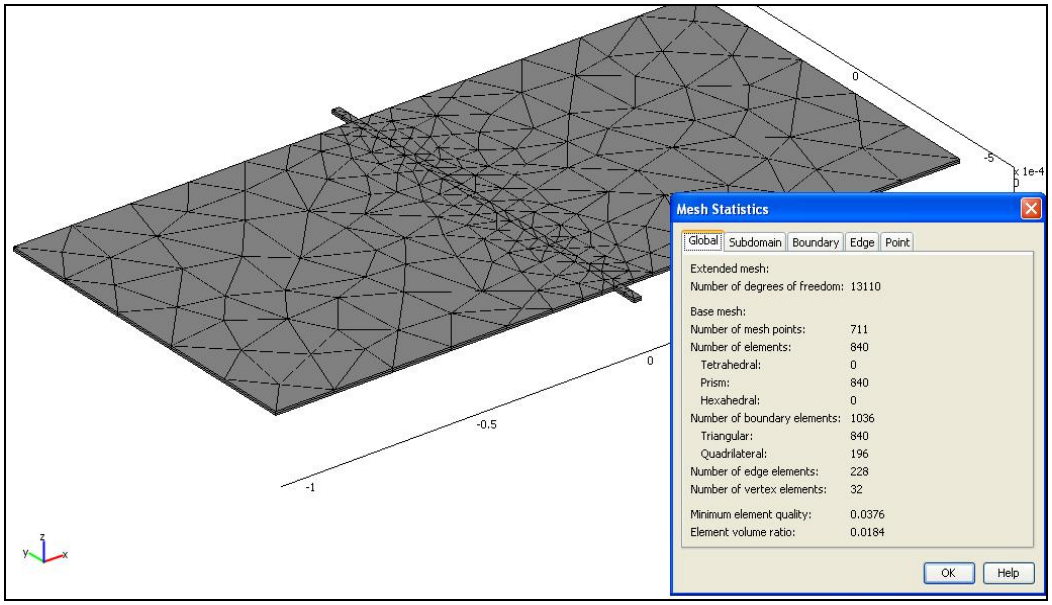

Figure 21. Mesh mode and mesh statistics in COMSOL.

5. The last step before starting the simulation is to set the solver parameters. Along with the type of solver, the range of frequencies, as well as the frequency step in the “parametric solver,” is set. Again, smaller frequency bins around resonance are used to obtain a precise resonance value. To reduce the solution time, larger frequency bins were used for the rest of the frequency range.

The procedure described above expresses the basic steps to set up and start a simulation. The decisions made concerning the boundary conditions and the load on the device, together with other details, will be discussed in the description of each specific model tested.

2. System Requirements

The number of numerical calculations that need to be performed, together with the fact that the two modules had to be coupled to perform the simulation, increased the need for computer processing power. All simulations were executed on an Intel based PC. The processor was a 4-core Xeon running at a frequency of 2GHz. The reason for having a multi-core processor is the ability to run more than one simulation simultaneously. The operating system was the 64-bit Windows XP Professional, and the amount of memory used was 16GB. At the time of this writing, this is the maximum memory that can be placed on a commercial PC.

Despite the fact that the computer used to run the simulations was quite powerful, the time required for the acoustic coupling simulations averaged about one hour per frequency. The average number of frequencies required to get a good representation of the resonance peak was about 100. This resulted in simulation times of 4 or more days for the whole frequency spectrum of interest. Furthermore, the maximum number of simulations running simultaneously was two. This resulted in the maximum allowable use of the available page file. Attempts to run simulations on poorer equipped computers resulted in “out-of-memory” error messages.

C. NON - ACOUSTIC COUPLED SIMULATIONS

The simulations run both by Shivok and Dritsas did not use the Acoustics Module to couple the pressure with the device. Instead, they calculated the force on the plate due to the acoustic wave analytically by integrating the pressure over the surface of each plate of the device. Dritsas showed in his thesis that the resultant forces could be assumed to operate at the midpoint of each plate with a time delay equivalent to the time difference of arrival of the pressure wave to the two points. This force was only applied at the top of the plate. On the bottom of the plate, the damping force was simulated by Dritsas to be proportional to the velocity of the device.

The primary objective for simulations run by Shivok [2007] was to predict the resonance frequencies of the early, perforated devices. The resonance frequency of the rocking mode was calculated to be 26% higher than the experimental one, while the bending mode frequency was calculated to be 0.6% smaller than the experimental. In contrast, Dritsas [2008] modeled a solid plate (non-perforated) device where the silicon substrate at the back was assumed to have been removed. Since the back was removed, squeeze film damping was practically eliminated. The next section discusses these simulation settings and results.

1. General Settings and Considerations

Dritsas's simulation focused in the regions of the resonance frequencies. These were 3-4 KHz for the rocking mode and 10-12 KHz for the bending mode. Assuming a plane wave incident on the device, the amplitude of the free field pressure wave is equal at both plates. As previously discussed, the resulting force is applied as a point force in the center of the two plates. Assuming an incidence angle other than zero, the applied forces differ slightly in-phase.

Table 1 summarizes the parameters used in the simulation run by Dritsas. As discussed above, the incident pressure (P) applied on the upper part of the device plates was entered as a numerical value. The direction of the acoustic plane wave was defined as "theta" and measured from the normal to the plate. It was used to calculate the time delay between the arrival of the assumed plane wave to the center of each wing (tau) and from that the phase difference (phi). Figure 22 shows a physical representation of the polar angle "theta" (θ) and also the azimuthal angle "psi" (ψ), which is measured from the x-axis to the y-axis counterclockwise and is defined between the interval $0<\psi<2\pi$. For the non-coupled simulations presented by Dritsas the angle ψ is 180 degrees while for the acoustic coupled simulations in this thesis, the angle was taken to be zero. Since the device is symmetrical, this difference does not affect the results.

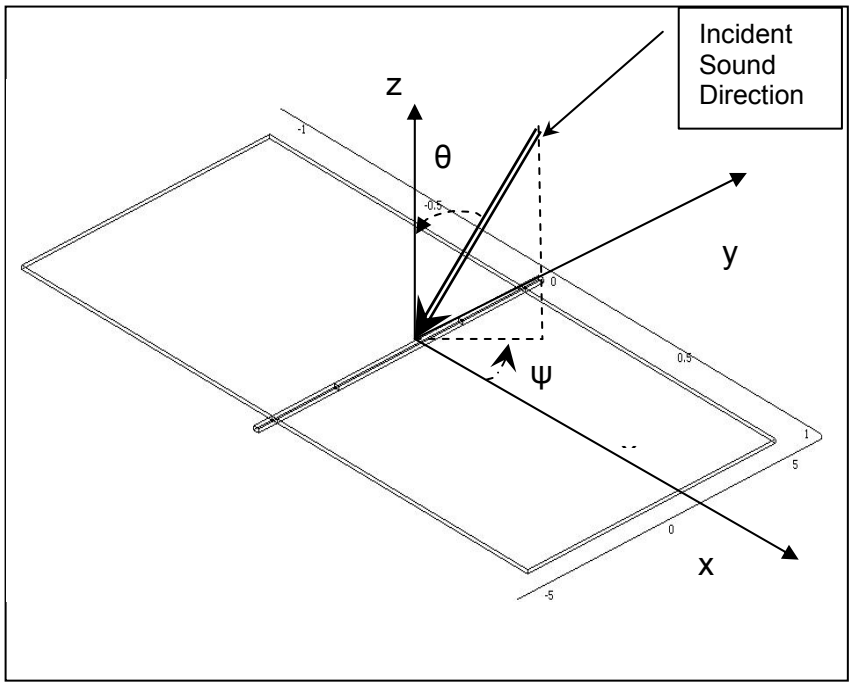

Figure 22. Definition of polar angle “θ” and azimuthal angle “ψ”.

To define the driving force, the value of “phi” is entered in the same window as the pressure amplitude (P). This is the phase difference between the force on the ipsilateral and contralateral plates. The damping force (pda) is applied to the underside of the plate. The formula used for the damping force is the one provided by Zhang *et al*., where the parameter “w_t_smsld” is the vertical velocity of the plates. The rest of the parameters used are the damping parameter “b,” the viscosity of air “mu,” the density of air “ro,” and the angular frequency calculated by the software for the frequencies set “omega_smsld.”

Description	Parameter	Numerical Value or Formula Used	Units
Incidence Pressure (P)	p	Numerical value defined by user. A value of 1 was used for the results presented	Pa
Damping Stress	pda	$b*\pi*(ro*mu*omega\_smsld/2)^{\frac{1}{2}}*w\_t\_smsld$	Pa
Damping Parameter defined by Zhang (Zhang *et. al.*, 2006)	b	2	--
Air Density (ρ)	ro	1.025	
Angular Frequency (ω)	omega_smsld	Calculated by program for every frequency defined by user in the "parametric solver"	rad/sec
Vertical Velocity (uz)	w_t_smsld	Calculated by program	m/sec
Incidence Angle	theta	Numerical value defined by user	Degrees
Time Difference (τ)	tau	-x*sin(theta*pi/180)/344	Sec
Phase Difference (φ)	phi	omega_smsld*tau*180/π	rad

Table 1. Parameters used in the model presented by Dritsas [After: Dritsas, 2008].

Figure 23 shows the parameters set for the upper plate. The pressure, referred to as "Face Load" by the software, has an amplitude of 1 [Pa] in the negative z-direction, while its phase is "phi." The damping force exerted on the bottom of the plate is in the opposite direction of the plate velocity. Figure 24 shows this.

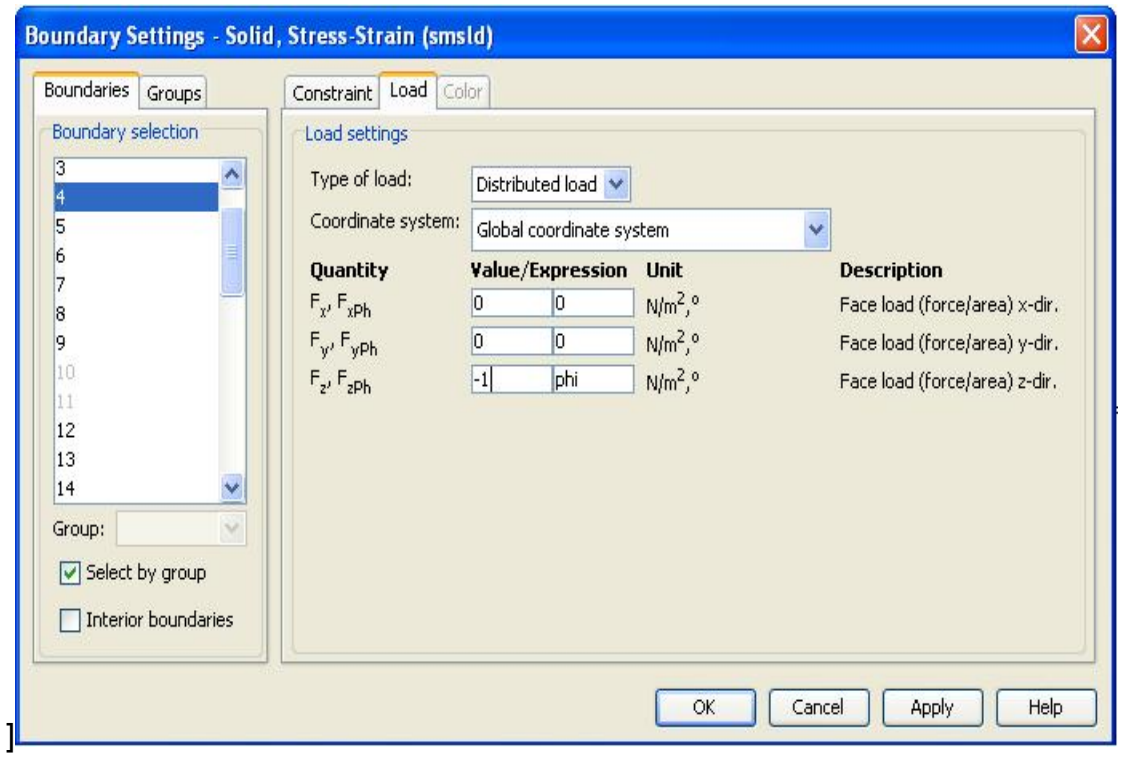

]

Figure 23. Set parameters for incident pressure at the upper plate.

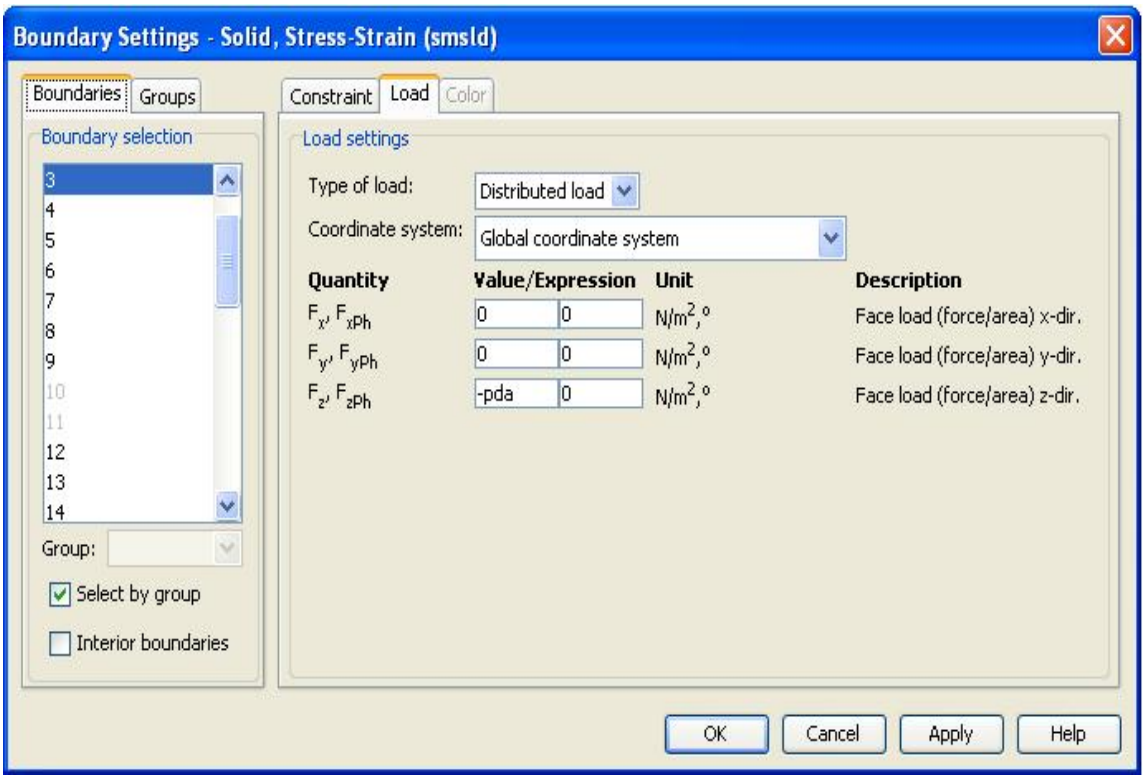

Figure 24. Set parameters for air damping under the plate.

2. Results

The results, as presented by Dritsas, appear on Table 2. In this table, the amplitudes of the contralateral and the ipsilateral plates of the MEMS device are recorded with respect to various angles of incidence at the two resonance frequencies. The incident pressure is 1 Pa. It must be noted that during the simulation a value of ρ=1.025 kg/m^3 was used for air density. If that value is changed to the correct ρ=1.25 kg/m^3 (which is the density of air at 1 atm, 20ºC [Kinsler *et al.*, 2000]), the effect on the amplitude of oscillation is small (about 60 nm less, or 9% error, for the rocking resonance and 300 nm less, or 7% error, for the bending resonance at an incident angle of 45º). This, together with the fact that the precision of the simulation is affected by the meshing size, supports the conclusion that the values in Table 2 can be used to compare with the results of the acoustic coupled simulations presented later.

Incident Angle	**Frequency**		**Displacement Ipsilateral Wing**		**Displacement Contralateral Wing**	
	Rocking Mode (kHz)	Bending Mode (kHz)	Rocking Mode (nm)	Bending Mode (nm)	Rocking Mode (nm)	Bending Mode (nm)
15°	3.48	11.11	268	4273	238	4267
30°	3.48	11.11	505	4265	475	4258
40°	3.48	11.11	642	4251	612	4258
45°	3.48	11.11	705	4254	675	4247
55°	3.48	11.11	785	4247	815	4239
70°	3.48	11.11	930	4237	900	4229
90°	3.48	11.11	990	4232	960	4224

Table 2. COMSOL simulation results for solid plate Device #8. value for air density is ρ=1.025 kg/m^3 [*From*: Dritsas, 2008].

In Table 2, the displacement of the ipsilateral wing is slightly larger than that of the contralateral. This is for all angles of incidence in both rocking and bending modes. The frequency response appears in Figure 25 where the vertical displacement of the device is plotted against frequency for an angle of 45º and sound incident pressure of 1 Pa.

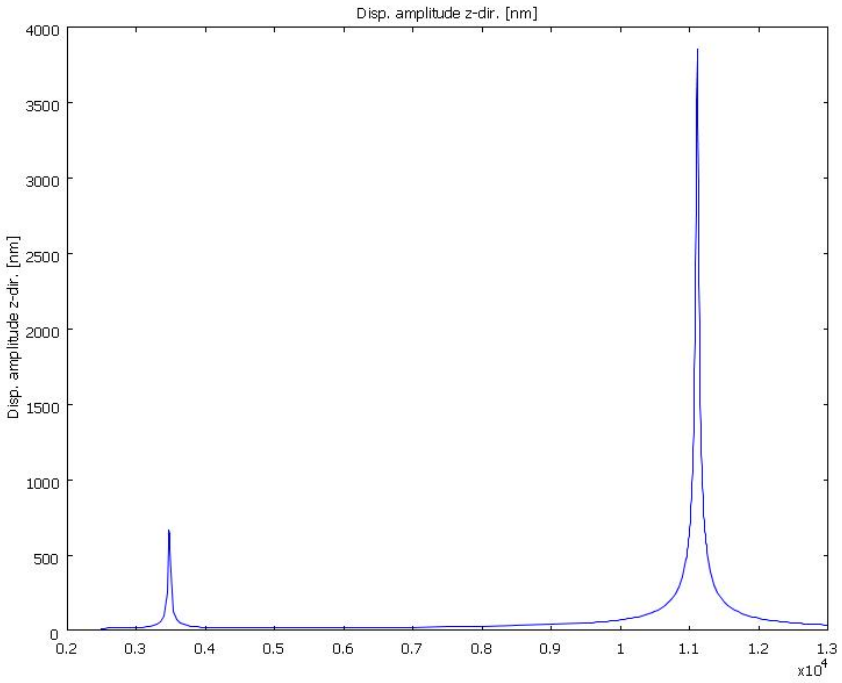

Figure 25. Simulated frequency response of Device #8 in the vertical direction.

The simulation results show that the amplitude of oscillation of the rocking mode increases as the angle of incidence increases. On the other hand, the amplitude of the bending mode remains almost constant [Dritsas, 2008]. Figure 26 plots this behavior.

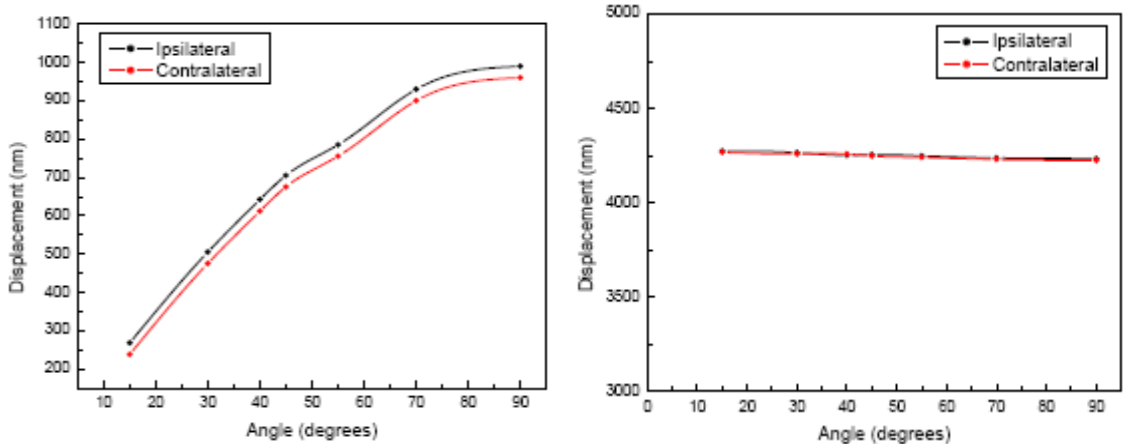

Figure 26. Displacement of rocking and bending mode versus angle of incidence (*After*: Dritsas, 2008).

D. ACOUSTIC COUPLED SIMULATIONS

Although Dritsas's simulation matched the experimental results for a solid plate device fairly well, the simplifying assumptions underlying the simulation are not realistic. The main problem lies in the lack of acoustic pressure at the backside of the plate. For an object, which is small in comparison to the wavelength, one expects the acoustic pressure to be almost uniform on all sides. The other issue of concern in his simulation is the fact that the damping was considered proportional only to the plate movement. Since an acoustic wave consists of air movement as well as pressure, one would expect the air particle velocity to provide an additional drag force on the plates in the direction of motion to the extent that it exceeds the plate velocity. Therefore, the drag force per unit length was changed to be proportional to the difference between the air particle velocity and the plate velocity, instead of just the plate velocity.

A simulation in which a sound wave is incident upon the device should provide more realistic results than one whose force is estimated analytically. The "Pressure Acoustics" mode in COMSOL solves the inhomogeneous Helmholtz equation to calculate the pressure at each point of the acoustic domain [COMSOL Users Guide, 2007]. Therefore, instead of requiring a known force

acting on the device, it calculates the net force based on the solution to the wave equation and the area of the plate. This allows for the investigation of problems where an analytical solution is unknown. The solution based on the Helmholtz equation can also include the pressure difference between the front and back of the device. Thus, coupling the MEMS device to the acoustic field has the potential for more accurate predictions of the device behavior.

1. Main Considerations

The main concern in creating a coupled simulation is in how to accurately couple the different "modules" in COMSOL, i.e., the Acoustics Module and the MEMS Module. The software requires that a parameter calculated by one of the modules acts as an input to the other and vice versa. One of the "Tutorial Models" in the COMSOL Acoustics Module documentation, the "Hollow Cylinder," provided the steps to couple the modules together [COMSOL Acoustics Module Model Library, 2007]. The acoustic pressure (p2), calculated by the "Acoustics Module," is used as boundary load on the device. The MEMS device couples back into the Acoustics Module by setting the acceleration of the surface of the device equal to the acceleration of the air in its surface (α_n). Figures 27 and 28 show this implementation into COMSOL where nx, ny, nz are the normal to the surface vectors in the outward direction.

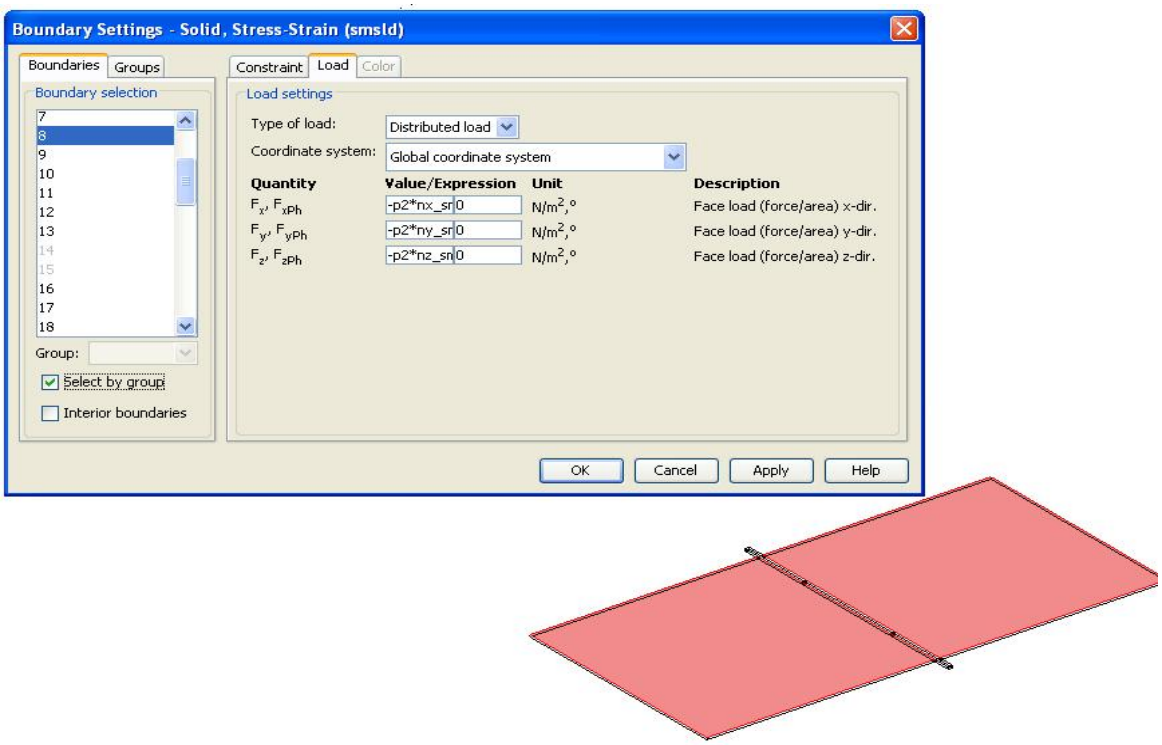

Figure 27. Coupling of the acoustic pressure in the MEMS solid stress-strain module (upper side of plate).

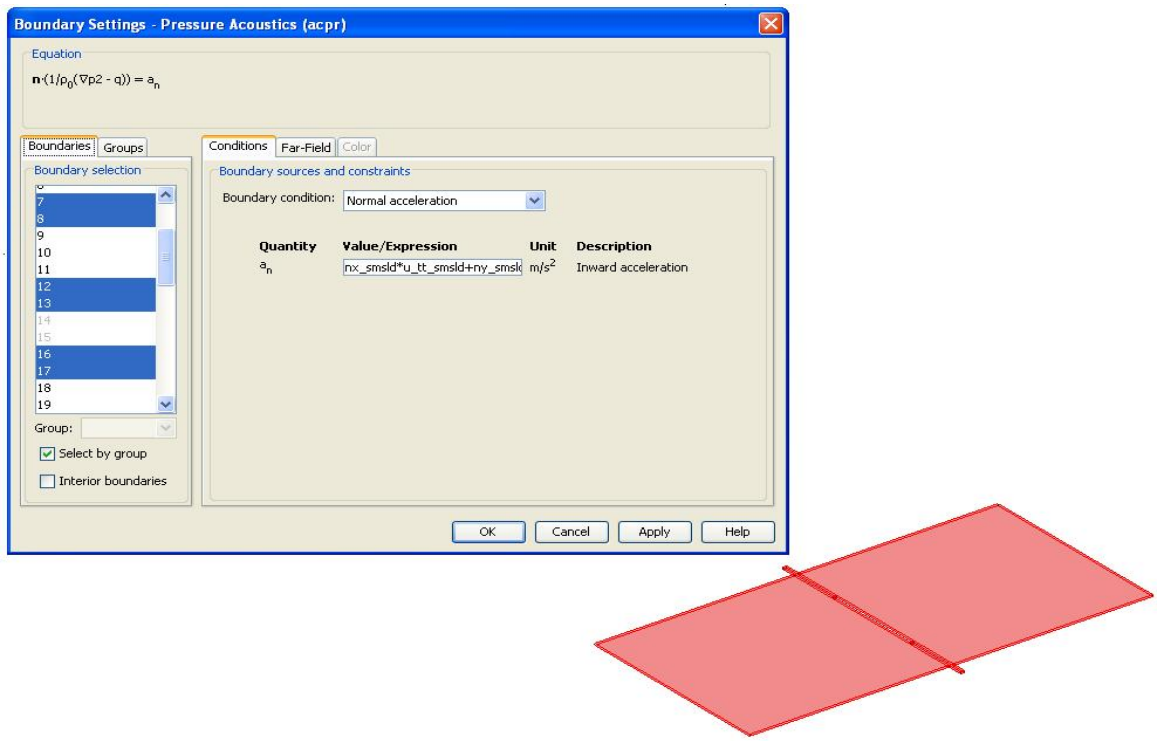

Figure 28. Coupling of the normal acceleration in the Acoustics Module.

As previously discussed, the device is so small that almost any incoming sound wave is essentially a plane wave. Therefore, the pressure acting on the two plates is uniform. In an attempt to produce a plane wave, two different acoustic domains were used, the box and the spherical domains. Since the sound wave in the spherical model is emitted by a point source, the wavefront is spherical. Therefore, the device has to be positioned far enough from the source for the incident wavefront curvature to be negligible. The following paragraphs provide specific details about both approaches.

2. Box Domain Model Simulation

a. Simulation Settings

The initial idea for the box domain model came from COMSOL Branch Manager, John Dunec Ph.D. He provided a rough model demonstrating the idea to LT Shivok to help predict more accurate displacement amplitudes for the perforated plate devices. This acted as a baseline for the simulations conducted, but various modifications were made with respect to meshing, boundary conditions, and the test device. Figure 29 shows the basic concept of the model where a box is drawn around the device. The initial dimensions of the box were selected to be 25mm x 25mm x 40μm.

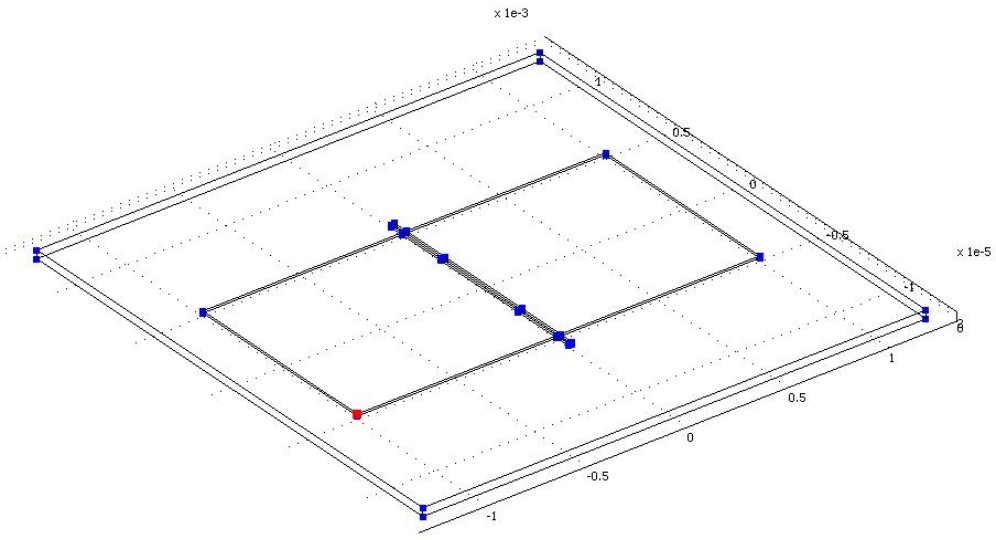

Figure 29. Schematic of the “Box Model”.

The main reason for choosing a very small height was to minimize the time required to achieve a solution. The need to concentrate only on the deformation of the MEMS device led to the assumption that the dimensions of the acoustic domain would not make any difference -- whether larger or smaller -- as long as they produced a plane wave of the required pressure amplitude incident upon the device. COMSOL provides the capability of defining one of the sides of the box as a radiating source with a user specified pressure value.

To simulate the response of the device in the presence of the direct sound field only, the boundary conditions in the Acoustics Module were defined in such a way that there would be no reflections inside the box. Amongst the various choices provided by COMSOL, the simplest way to eliminate reflections is to choose the “Radiation Condition.” This condition is defined in the software documentation as one that “allows an outgoing wave to leave the modeling domain with no or minimal reflections” [COMSOL User Guide, 2007]. After selecting this boundary condition, selecting the wave type is next, which in this work’s case was, for obvious reasons, “Plane Wave.” This condition was applied on the lower side of the box. The rest of the sides were initially left as “Sound

Hard" as they were given in the original model. Finally, the settings for the upper side, which would be the sound source, appear in Figure 30. The use of direction cosines defines the direction of the sound wave ("Wave Direction" field in Figure 30).

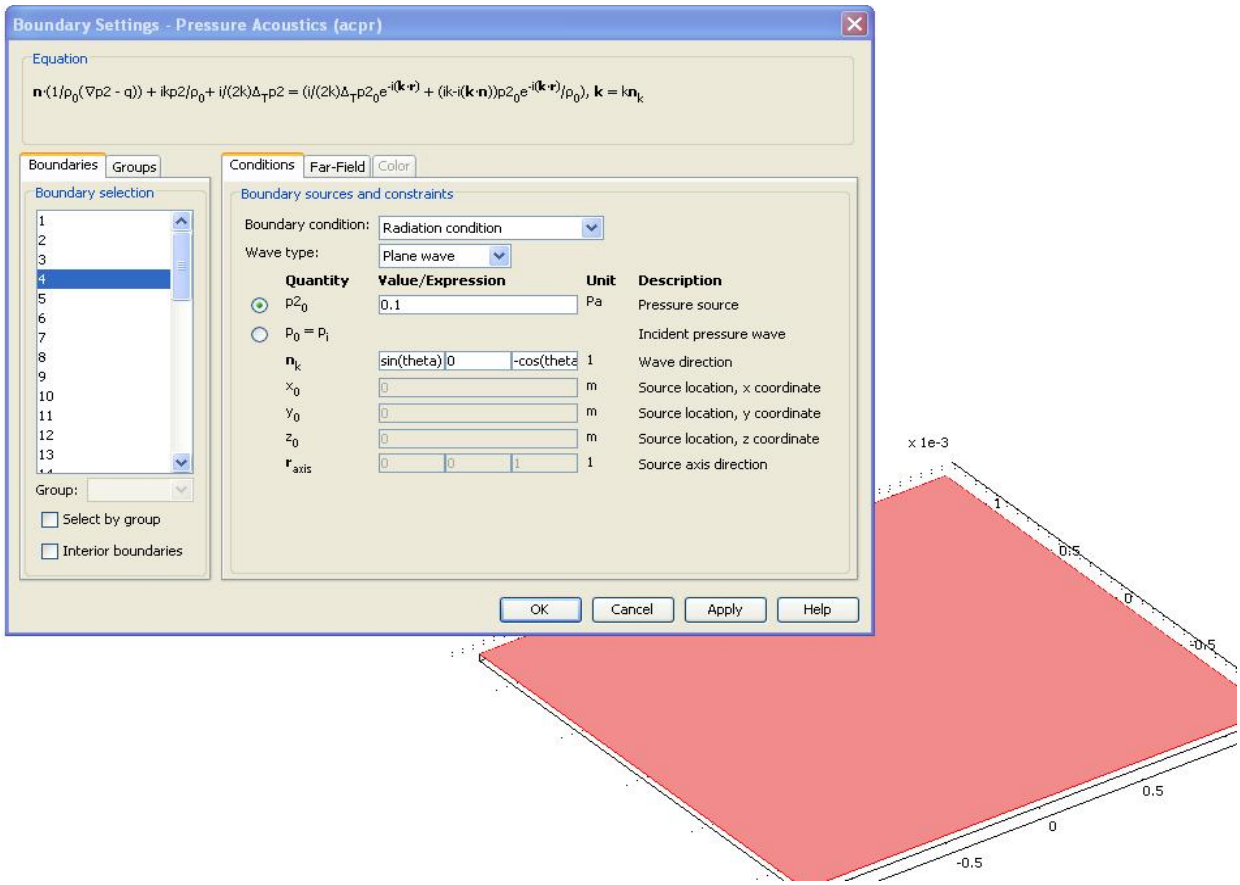

Figure 30. Boundary settings on the upper side of the box.

The actual MEMS boundary conditions remain the same as the ones presented in paragraph C.1. i.e., the pressure is only applied on the top plate while the damping force is only proportional to the plate velocity. The only difference is that, instead of a user defined pressure value applied directly upon the device, the software calculated value of the sound wave, as shown in Figure 27, is used.

b. Results

The simulation concentrated around the rocking and bending mode. The pressure of the sound field incident on the devise was 0.1 Pa. The angle of incidence was initially set to 45º. The use of the above value for sound pressure would appear to make the results difficult to compare with the ones presented in Table 2. Nevertheless, the relation between the pressure applied and the deformation caused on the device for a range of pressure values between 0.1 Pa and 1Pa can be approximated as linear. Rerunning both the acoustic coupled and the non-acoustic coupled simulations for different incident pressure values proves this. Therefore, if the pressure upon the device reduces by a factor of 10, the oscillation amplitude would also reduce by an equal amount compared to that presented in Table 2.

The physical behavior of the device in the presence of the sound field appears in Figures 31 (rocking mode) and 32 (bending mode). It is obvious that the behavior is expected: both plates have approximately the same amplitude of oscillation, are out-of-phase in the rocking mode, and in-phase in the bending mode.

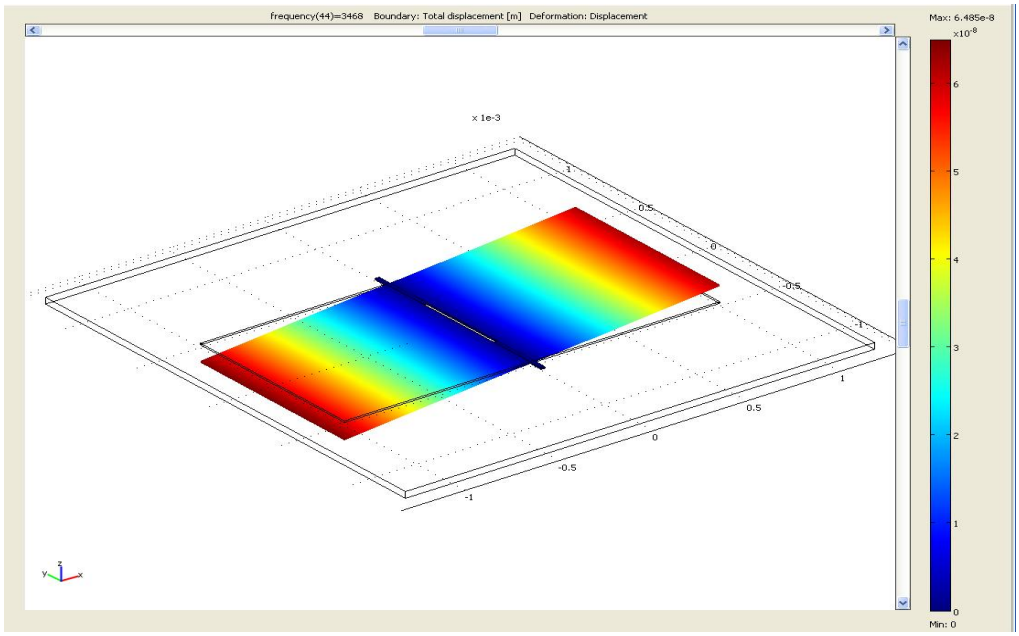

Figure 31. “Box Model” rocking mode.

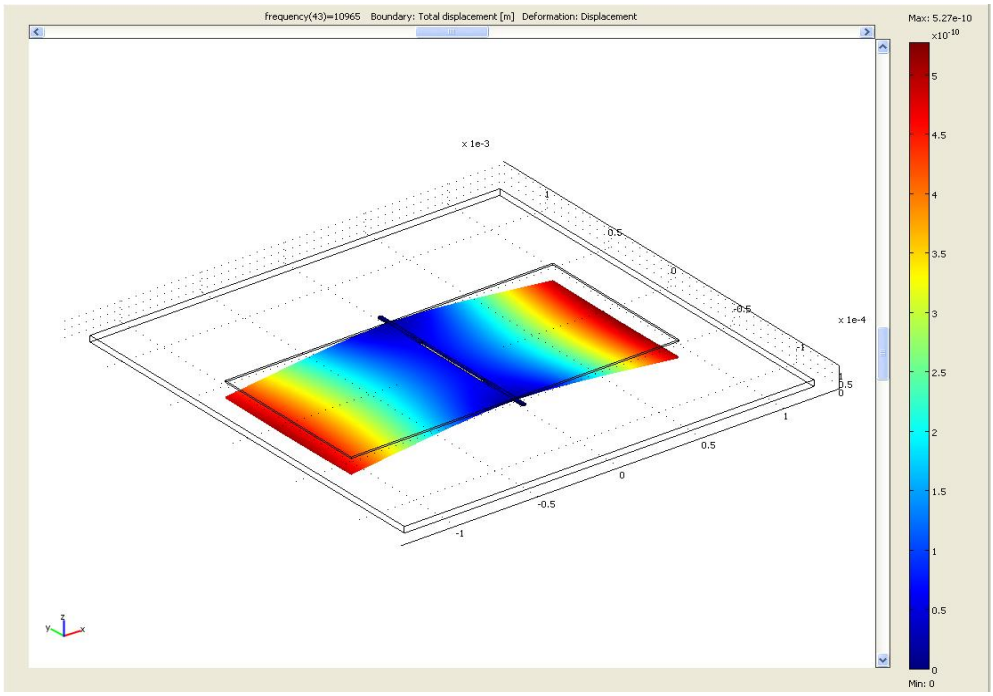

Figure 32. “Box Model” bending mode.

Table 3 provides numerical results for the simulation. After performing the linear interpolation to account for the reduced incidence pressure amplitude, Tables 2 and 3 show good agreement in both rocking mode frequency and amplitude. On the other hand, although the difference in the bending mode frequency is small ($\approx$200Hz) and certainly within the construction limits of the actual device, there is a significant decrease in the oscillation amplitude.

Incident Angle	**Frequency**		**Displacement Amplitude Ipsilateral Wing**		**Displacement Amplitude Contralateral Wing**	
	Rocking Mode (Hz)	Bending Mode (Hz)	Rocking Mode (nm)	Bending Mode (nm)	Rocking Mode (nm)	Bending Mode (nm)
45º	3,468	10,960	66.8	16.1	64.5	16.1

Table 3. COMSOL simulation results for a solid plate device in a Box Acoustic Domain.

In Figure 33, the deformation of the device in the vertical direction is plotted against frequency near the two resonance frequencies. A comparison with the one obtained for the non-acoustic coupling simulation in Figure 25 again yields two distinct resonance peaks.

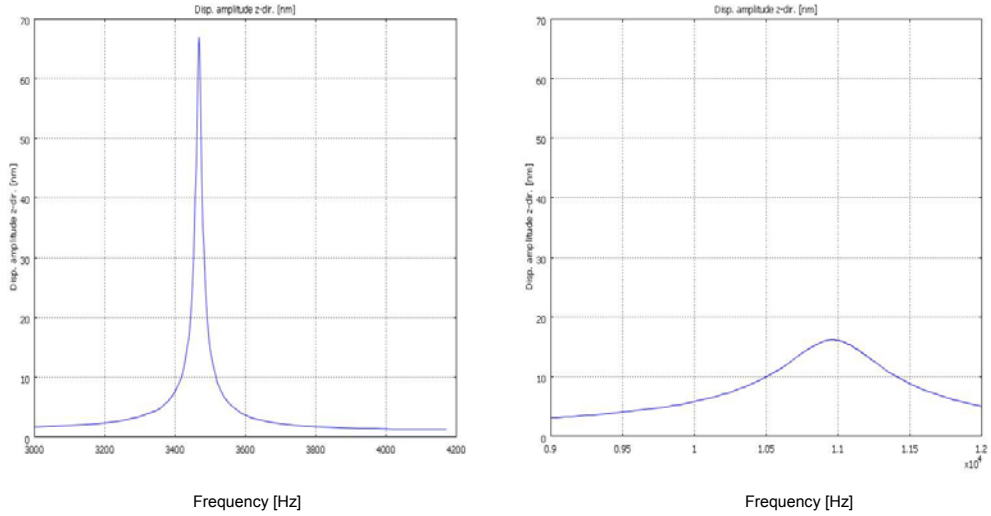

Figure 33. Simulated frequency response for the “Box Model”.

An important observation - apart from those concerning the amplitudes of oscillation and resonance frequencies discussed above - is the width of the frequency response curves. The quality factor around the bending mode resonance in the graph is obviously much lower (wider curve) than it was in the non-acoustic coupled simulation. This suggests a larger damping coefficient in the coupled case, but it is difficult to explain why. In investigating the results further, the pressure shows an anomalous behavior as well. For example, a plot of the pressure amplitude on the edge of the device versus frequency appears in Figure 34.

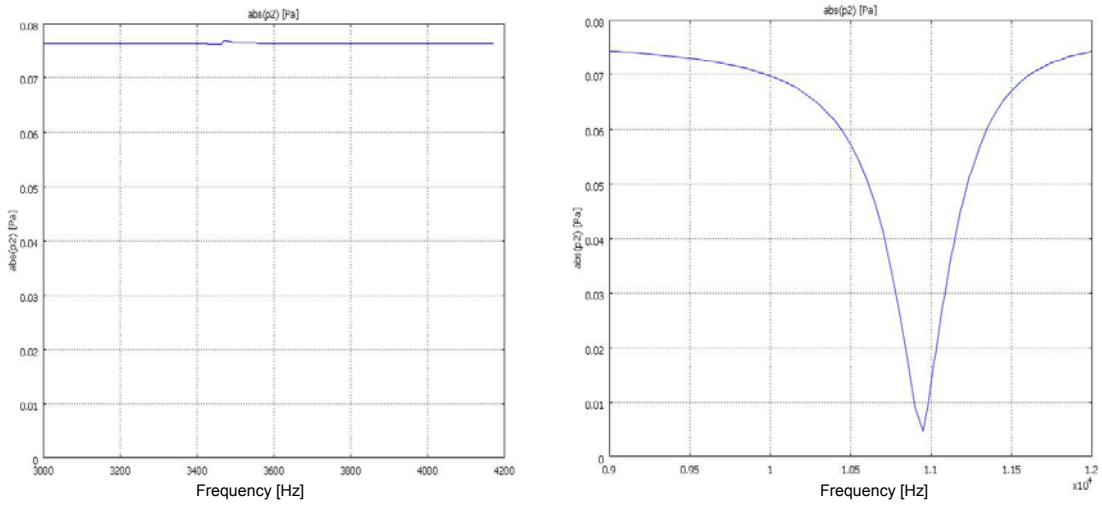

Figure 34. Simulated pressure response for the “Box Model”.

Notice that the pressure on the plate of the MEMS device is very close to the one expected around the rocking resonance. In the bending resonance, there is a huge drop, and the pressure is almost zero.

To investigate the pressure drop, both the dimensions and the acoustic domain boundary conditions were revised and another set of simulations were conducted. The results for various simulations run for the resonance frequencies of the rocking and bending modes (as contrasted to a range of frequencies) appear in Table 4.

Incident Angle	Frequency		Displacement Amplitude Ipsilateral Wing		Dimensions of Acoustic Domain (Box)
	Rocking Mode (Hz)	Bending Mode (Hz)	Rocking Mode (nm)	Bending Mode (nm)	
45º	3,468	10,960	51.7	67.3	5mm x 5mm x 50μm
45º	3,468	10,960	51.4	825	9mm x 9mm x 90μm
45º	3,468	10,960	35.1	6	50mm x 50mm x 90μm

Table 4. COMSOL simulation results for a solid plate device in Box Acoustic Domains of varying sizes.

The oscillation amplitude in both modes presents abnormal fluctuation -- especially noticeable in the bending mode resonance. These results are attributed to the failure of the bottom radiation condition to totally eliminate reflections. An attempt to change all boundaries to “Radiation Condition” again failed to reproduce the results of the non-coupled simulations. In all simulations run, the wavefront exhibited clear departures from planar. This indicated that reflections from the sides of the box continued to be an issue. COMSOL Technical Support suggested the use of a Perfectly Matched Layer (PML) around the box. A PML is essentially a tool provided by the software to absorb unwanted reflections. This approach also failed to eliminate reflections inside the box. Therefore, because of the inability to simulate a perfect plane wave in the box, the method was abandoned.

3. Sphere Domain Model Simulation

a. Simulation Settings

To couple the sound field incident upon a MEMS device in this new approach, a spherical acoustic domain was drawn around it. Figure 35 shows this. The sound source was defined as a point source in the outer boundaries of the acoustic domain. An initial value of 8mm was used for the sphere radius. This placed the source in the far field of the device.

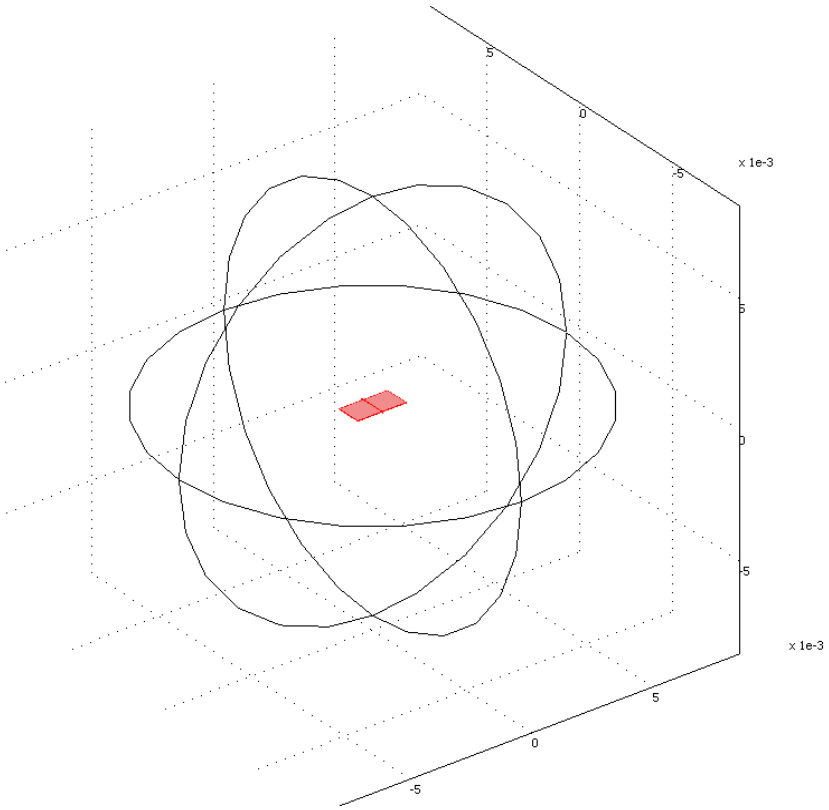

Figure 35. Schematic of the “Sphere Domain” model, 8mm radius.

The strength of the radiating point source was defined in terms of its power. For spherical wave propagation, the power required to achieve a given intensity as a function of the radial distance is given by:

$$\Pi = 4\pi r^2 \mathrm{I} \tag{5.1}$$

where Π is the power of the source; r is the distance from the device; and I is the intensity of the sound at the device. The instantaneous intensity is given by $\mathrm{I} = \frac{p^2}{\rho c}$. Therefore, using r=8mm and ρc = 415 $\frac{kg * m}{\sec}$, the power of a point source required to produce a peak pressure of P = 1 Pa incident upon the device

is calculated to be $\Pi = 1.938x10^{-6}W$. The point source settings appear in Figure 36. As previously defined in Figure 22, the source was located at a 45º polar angle and a 0º azimuthal angle.

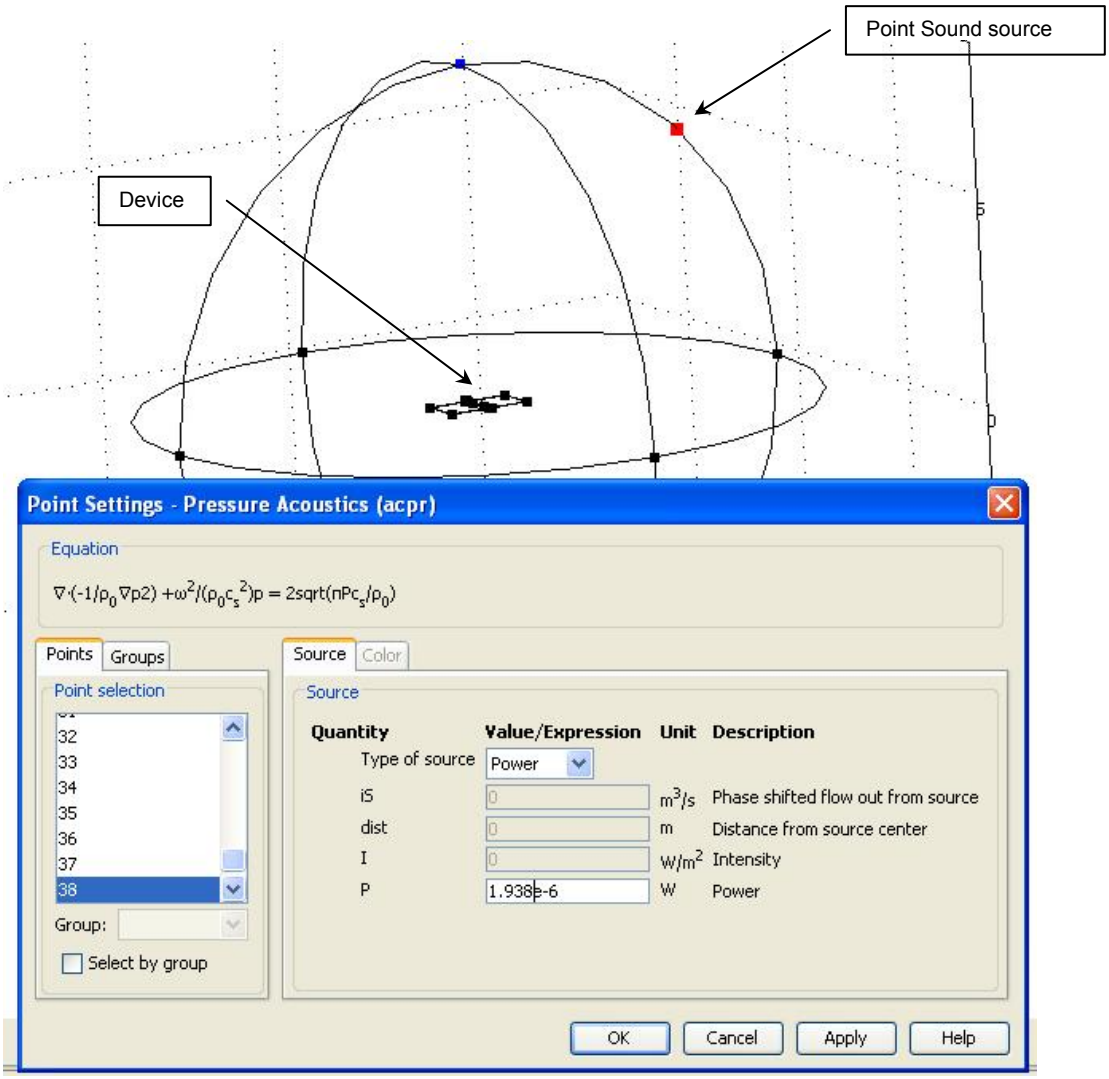

Figure 36. Point sound source settings and position.

The coupling of the Acoustic Module and the MEMS Module was achieved as discussed in paragraph D.1. of this chapter. Again, the boundary conditions in the acoustics domain were selected to eliminate reflections coming from the sides of the sphere. The “Radiation Condition” was chosen as in the “Box Model,” but, in this case, the wave type was set to “spherical wave.”

Although in this simulation the sound source has a 0º azimuthal angle (ψ), this could easily be varied. A single sound source, or even multiple sources, with varying polar and azimuthal angles with respect to the device can be simulated with this method.

The "Solid Stress - Strain" boundary settings remained the same as in previous simulations. The calculated sound pressure (p2) was only applied to the top plate of the device and damping, as calculated by Zhang's formula, is applied under the device. The damping formula used in this simulation was only proportional to the plate velocity in an attempt to reproduce the results obtained by Dritsas.

b. Results

To reduce the solving time, the simulation focused on frequencies around the two resonance frequencies. In contrast to the box model, there were no obvious reflections from the sphere boundary. The results for an incident pressure of 1 Pa and an angle of 45º are tabulated in Table 5. Figure 37 plots the frequency response of the device.

Incident Angle	**Frequency**		**Displacement Amplitude Ipsilateral Wing**		**Displacement Amplitude Contralateral Wing**	
	Rocking Mode (Hz)	Bending Mode (Hz)	Rocking Mode (nm)	Bending Mode (nm)	Rocking Mode (nm)	Bending Mode (nm)
45º	3,450	10,900	1,703	4,570	1,685	4,566

Table 5. COMSOL simulation results for a solid plate device in a sphere Acoustic Domain, radius 8 mm.

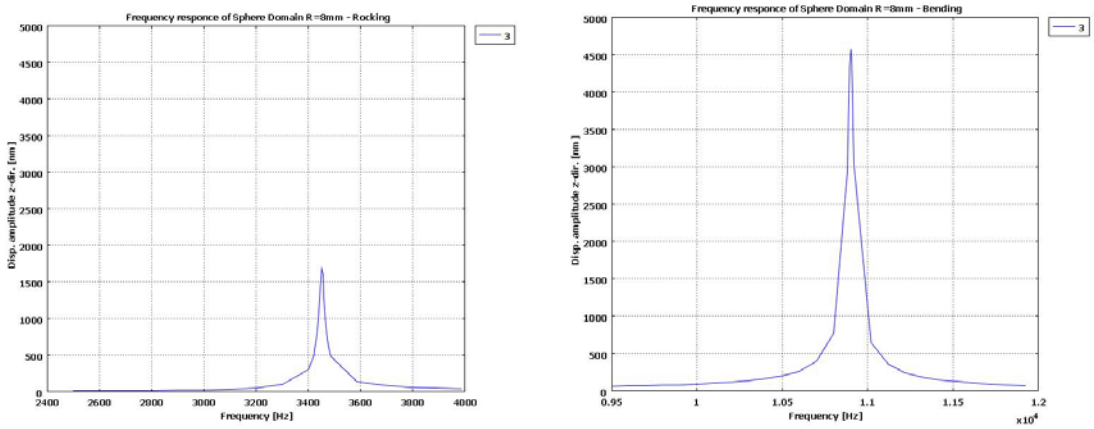

Figure 37. Simulated frequency response for the 8mm radius “Sphere Model”.

Figures 25 and 37 show that the frequency responses are in good agreement. Both of them present two distinct, sharp, resonance peaks with similar quality factors Q. In addition, the results presented in Table 2 from Dritsas show a very good agreement with the results in Table 5 in both bending and rocking mode resonance frequencies. On the other hand, the displacement amplitudes at resonance show an increase of about 130% for the rocking mode and 8% for the bending mode when compared to Dritsas’s results.

To understand the large deviation in the resonance amplitudes -- especially that of the rocking mode -- it is essential to consider the effect of source distance on the pressure amplitude of the two plates. Although the source was placed in the far field of the device, there is still a small pressure difference between the ipsilateral and the contralateral plates. This pressure difference can be calculated using the geometry in Figure 38.

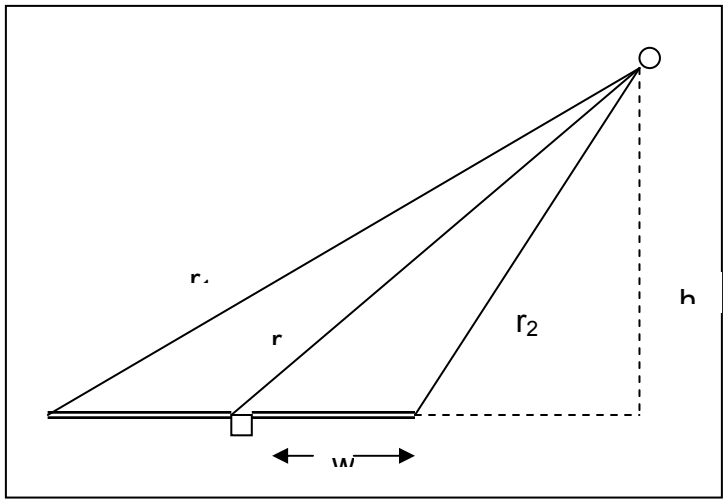

Figure 38. Pressure difference at the two edges of the MEMS device.

The pressure of a propagating spherical wave is inversely proportional to the distance from the source [Kinsler *et al*., 2000]. Therefore,

$$P = \frac{A}{r} \tag{5.2}$$

where A is a proportionality factor, which depends on the amplitude of the source and r is the distance from the source. Therefore, the pressures P_1 and P_2 at the two opposite edges of the device are:

$$P_1 = \frac{A}{r_1} \quad \text{and} \quad P_2 = \frac{A}{r_2}.$$

The fractional pressure difference between these two points can be expressed as:

$$\frac{\Delta P}{P} = \frac{P_2 - P_1}{P} = \frac{A\left(\frac{1}{r_2} - \frac{1}{r_1}\right)}{A\frac{1}{r}} = \frac{\left(\frac{1}{r_2} - \frac{1}{r_1}\right)}{\frac{1}{r}} \tag{5.3}$$

The distances r_1, r_2 can be calculated from the figure as:

$$r_1 = \sqrt{(r\cos\theta)^2 + (r\sin\theta + w)^2} \quad \text{and} \quad r_2 = \sqrt{(r\cos\theta)^2 + (r\sin\theta - w)^2}$$

A simple Matlab program was written to calculate the expected pressure difference based on the calculations above. For the initial spherical radius, the result was an 18% difference in the incident pressure between the two edges. This pressure difference mainly affects the rocking mode amplitude since this mode is driven by the pressure difference between the plates. On the other hand, the bending mode is not as sensitive to the pressure difference since it is driven by the sum of the pressures on the two plates [Miles *et al.*, 1995].

The pressure difference between the edges of the device, as was calculated by COMSOL, appears in Figure 39. The pressure of the ipsilateral edge (green line) and the contralateral edge (blue line) are plotted against frequency. As expected, the percentage pressure difference between the two edges is about 18%.

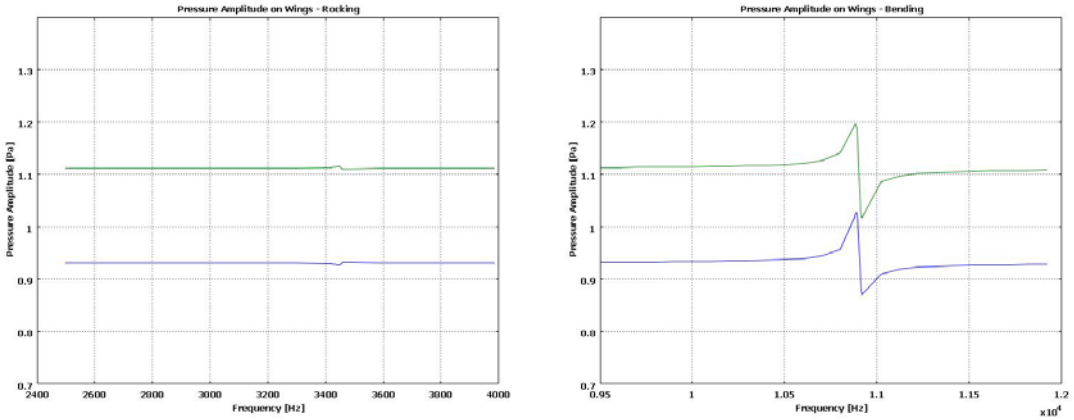

Figure 39. Simulated pressure difference at the two edges of the MEMS device.

An interesting phenomenon observed in the previous figures is the small disturbance in pressure. This disturbance exists exactly at the resonance frequencies but is more noticeable in the bending mode resonance. The reasons for this behavior are not precisely understood and need further investigation.

c. Results for Revised Sphere Radius

To reduce the pressure difference between the two edges of the MEMS device, the radius of the sphere was increased to 3cm. At the same time, the power of the source was revised to correspond to the new distance. The expected percentage difference for that radius was estimated to be about 5%. The calculated Sound Pressure Level (SPL) at the resonance frequency of the rocking mode appears in Figure 40. The reference pressure is the standard for air (20 μPa).

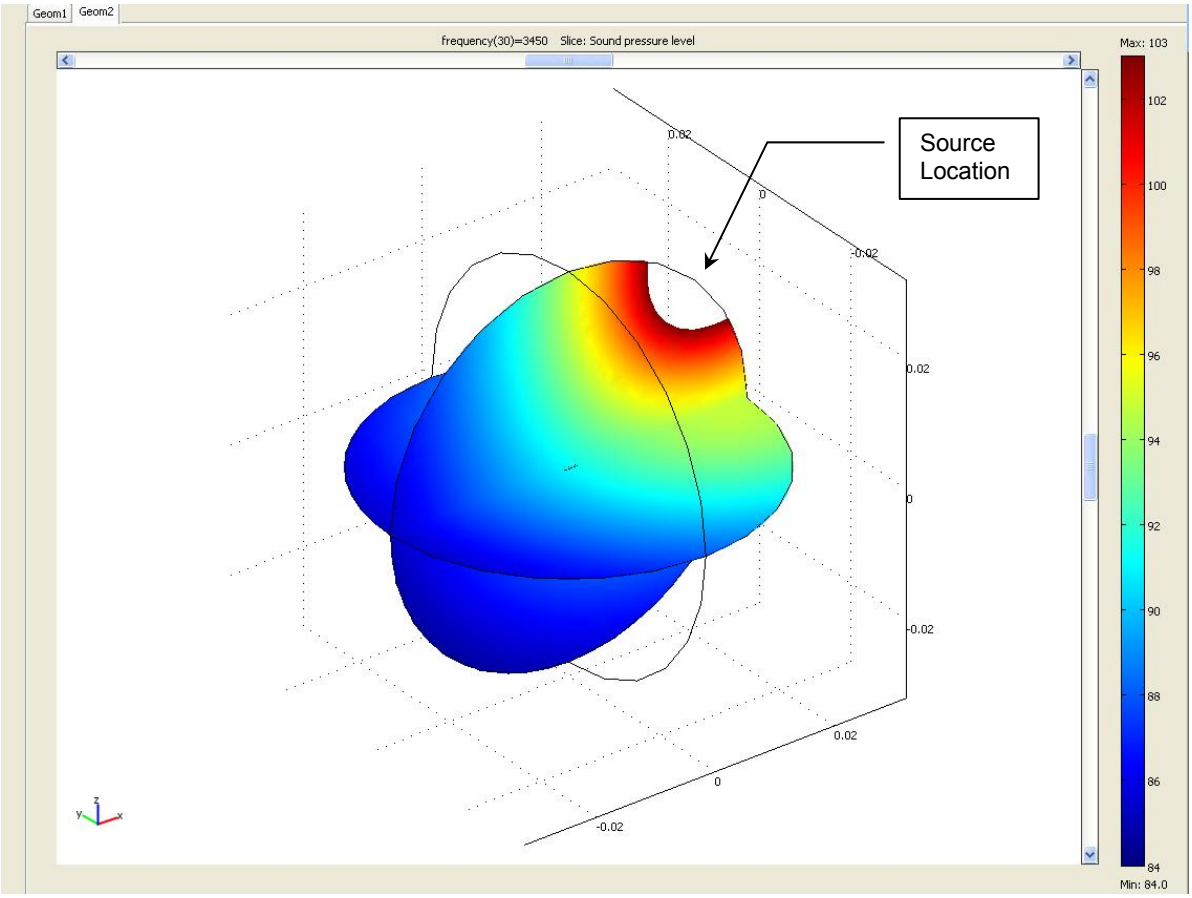

Figure 40. Sound Pressure Level of the “Sphere Model” at f = 3,450 Hz.

The image shows a spherical wave incident at a 45º angle upon the device. There are no obvious reflections coming from the sides of the spherical domain. This is an indication that the “Radiation” boundary condition works as

expected. To verify that the propagation is indeed spherical, a plot of the SPL versus distance from the source to the device at 3 cm was produced (Figure 41). The plot is linear with the expected slope for a spherical wave.

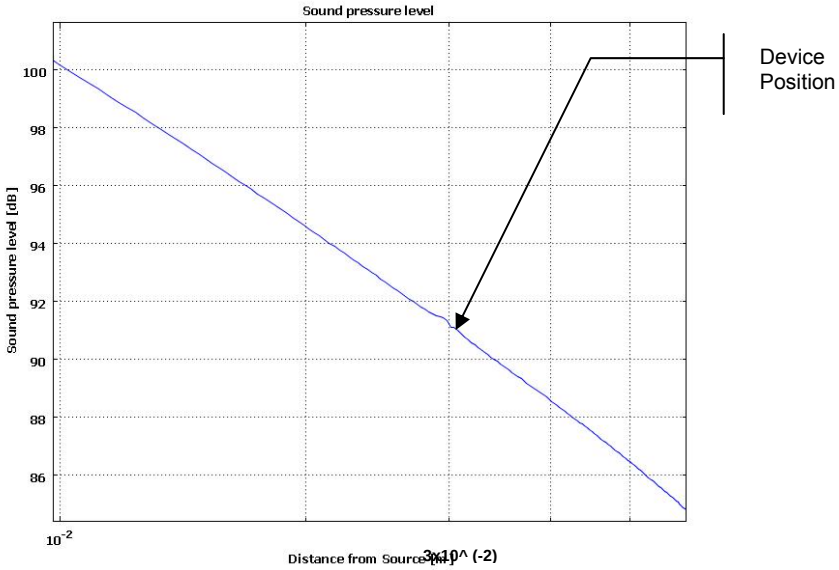

Figure 41. Sound Pressure Level over a diagonal at f = 3450 Hz.

In Figure 42, the pressure difference between the two opposite edges of the device is plotted against frequency. As was expected, the percentage pressure difference is 5%. Again, as described above, there is a small disturbance at the resonance frequency.

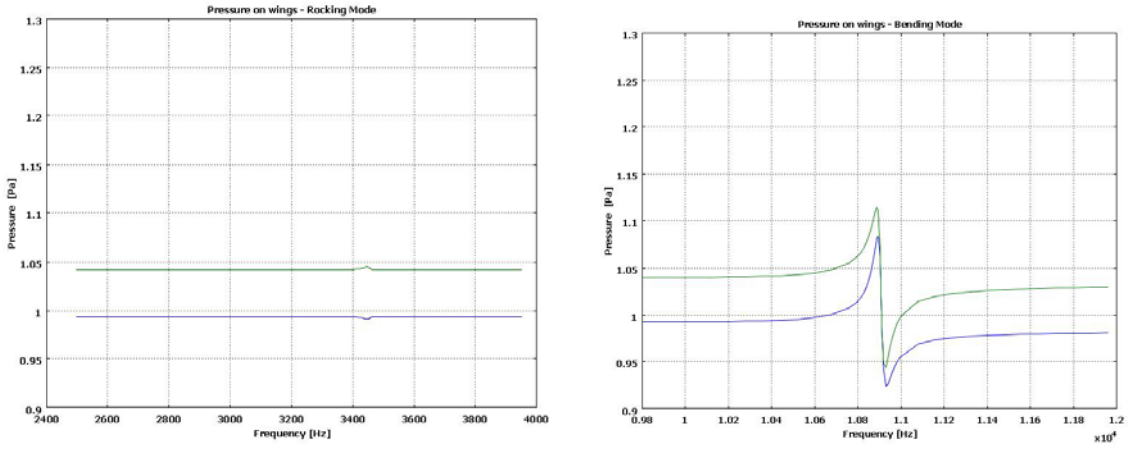

Figure 42. Pressure difference at the two edges of the MEMS Device with Acoustic Domain radius of 3 cm.

The physical behavior of the device at the two resonance frequencies appears in Figures 43 and 44. As expected, in the rocking mode the two plates move with the same amplitude and are 180º out-of-phase. In the bending mode, they move again with the same amplitude and are in-phase.

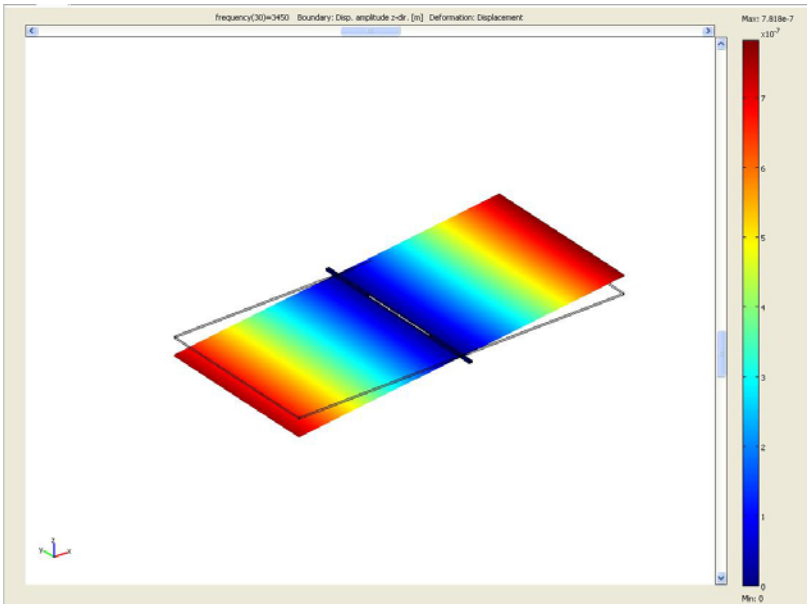

Figure 43. Device deformation in the rocking mode frequency – Sphere Model.

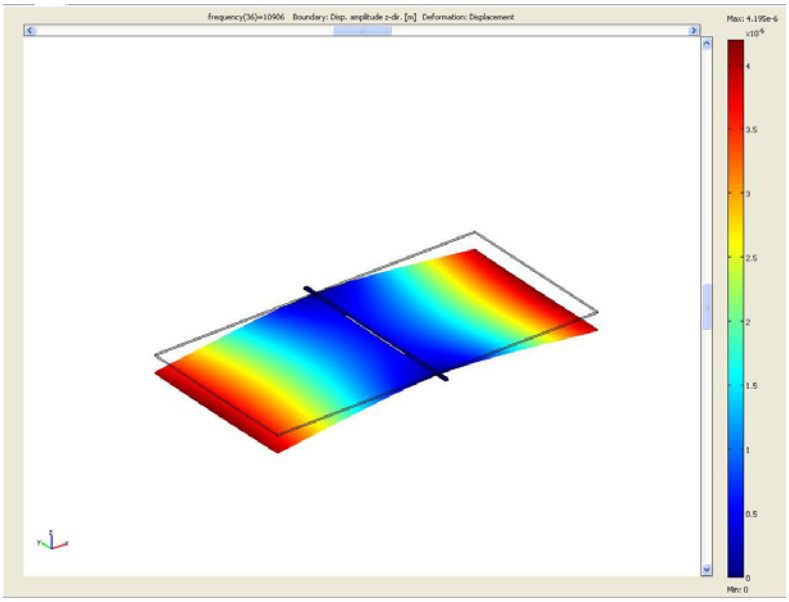

Figure 44. Device deformation in the bending mode frequency – Sphere Model.

Simulation results for various angles of incidence appear in Table 6. A comparison with those presented in Table 2 shows that the rocking mode resonance is almost identical. There is a small difference of 200 Hz in the bending mode resonance. Furthermore, there is good agreement in the displacement amplitudes between the acoustic coupled simulations presented in Table 6 and the non-acoustic coupled simulations presented in Table 2. Specifically, there is an increase of 10% in the rocking mode amplitude and a decrease of 6% in the bending mode amplitude. The small increase in the rocking mode oscillation amplitude values, appearing in the current simulation, can be attributed to the small 5% pressure difference between the two plates.

Incident Angle	**Frequency**		**Displacement Amplitude Ipsilateral Wing**		**Displacement Amplitude Contralateral Wing**	
	Rocking Mode (Hz)	Bending Mode (Hz)	Rocking Mode (nm)	Bending Mode (nm)	Rocking Mode (nm)	Bending Mode (nm)
30	3,450	10,906	562	4,025	535	4,022
45	3,450	10,906	777	4,025	759	4,022
60	3,450	10,906	951	4,028	924	4,024
80	3,450	10,906	1,082	4,026	1,055	4,018

Table 6. COMSOL simulation results for a solid plate device in a spherical Acoustic Domain for various angles of incidence, radius R=3 cm.

A comparison between the frequency response of the non-acoustic coupled simulation conducted by Dritsas (red line) and the acoustic coupled simulation using the sphere model (blue line) appears in Figure 45. Both simulations were run for an incident pressure of 1 Pa, and the air density is corrected in both to $\rho = 1.25\ kg/m^3$. The angle of incidence is 45º. Just as in the comparison of the tabulated results, there is good agreement between the two. In the rocking mode, the resonance frequency value for the acoustic coupled simulation is 0.7% smaller than of the non-acoustic coupled. The amplitude is

16% larger. In the bending mode, the resonance frequency value for the acoustic coupled simulation is 2% smaller than of the non-acoustic coupled. The amplitude is 4% larger.

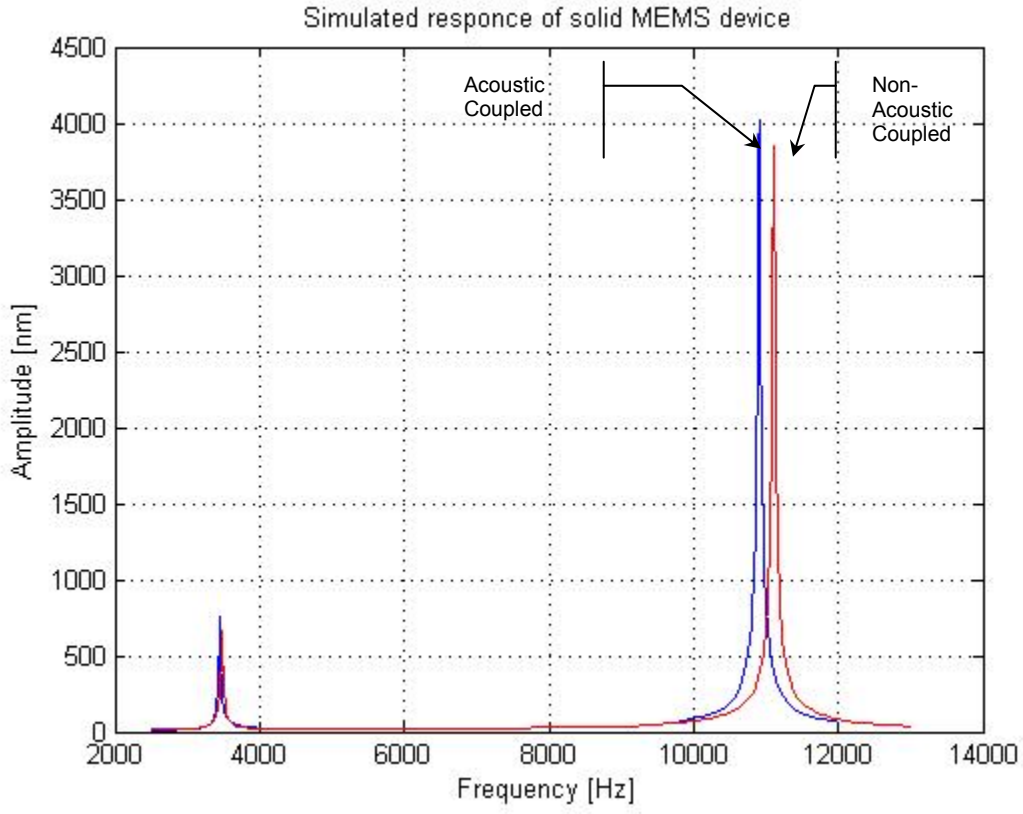

Figure 45. Comparison plot between the non-acoustic coupled and acoustic coupled simulation run using the Sphere Model.

To compare the two models further, Figure 46 depicts the displacement amplitude of the two plates as a function of the incidence angle for the sphere model -- both for the rocking and bending mode resonance frequencies. The behavior of the device is similar to the one in Figure 26. In the rocking mode, the amplitude increases as the angle of incidence increases. In the bending mode, it essentially remains constant.

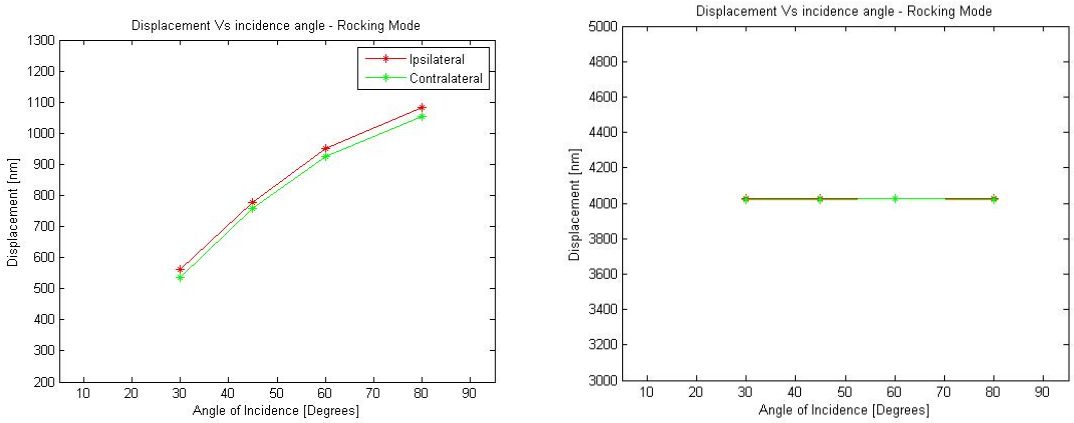

Figure 46. Displacement versus angle of incidence for the rocking and bending mode – Sphere Model.

Experimental results, as presented by Dritsas, appear in Figure 47. Although the exact incident pressure used to obtain this data is unknown, judging from the displacement amplitudes, the pressure was not the 1 Pa used for the simulation. Therefore, no direct comparison can be made between the displacement amplitudes. The graph shows the resonance frequencies and displacement amplitudes of two identical devices, i.e., Device #8 and Device #11. A difference of about 300 Hz is obvious in the figure between the bending mode resonances of the two presumably identical devices. There is also a noticeable difference in the rocking mode oscillation amplitude between the two.

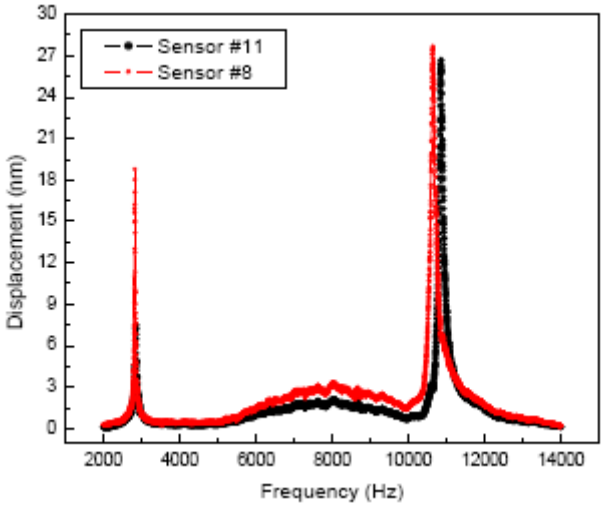

Figure 47. Frequency response of two identical sensors (*After*: Dritsas, 2008).

Comparing the above presented experimental results with those achieved in this work, there are small but noticeable deviations in the resonance frequencies of the two modes. The simulated value for the rocking mode resonance is around 550Hz greater than the experimental value. This is a discrepancy of about 19%. Dritsas attributed this difference to variations in device thickness due to the construction procedure [Dritsas, 2008]. The discrepancy in the bending mode resonance was slightly smaller. The experimental value is smaller compared to the simulated by about 90 Hz for device #11 (i.e., 0.8% difference) and about 300 Hz for device #8 (i.e., 3% difference). This discrepancy can also be attributed to limitations in the precision with which the plate thicknesses can be controlled in the construction process. Apart from the plate and beam thickness, the size of the slit must also be considered. In simulations, increasing the size of the slit by 0.2 mm reduced the bending mode resonance by 1,000 Hz.

Other experimental results provided by Professor Karunasiri for solid plate devices tested with an incident sound pressure of 0.1Pa were within an order of magnitude of the displacement amplitudes produced by the simulation. For an incident angle of 45º, the corresponding experimental amplitudes are 120 nm for the rocking mode and 200 nm for the bending mode. If

linear interpolation is conducted on the simulation results presented in Table 6 for an incident pressure of 0.1 Pa, the equivalent values are 76 nm – 36% lower -- and 402 nm – 50% higher --, respectively.

4. Revised Damping Simulations

Simulations conducted up to this point assumed that the acoustic pressure acted only on the top of the plate and that the acoustic pressure on the back was equal to zero. In addition, the air damping, implemented using Zhang's formula, was made proportional to the plate velocity alone. Since the back is open and the distance to it small, the acoustic pressure on the bottom of the device should be fairly close to the pressure at the top. This pressure difference can be approximated by the expected free field pressure difference in the acoustic wave which is given by:

$$\Delta p \cong p_o \sin k\Delta x = p_o \sin \frac{2\pi f}{c} \Delta x ,$$

where p_o is the peak acoustic pressure, k is the wavenumber, f is the frequency, c is the free field sound speed, and Δx is the distance between two points along the pressure wave. Referring back to the device dimensions shown in Figure 15, if the pressure difference between the top and bottom were simply given by the plate thickness alone, it would be extremely small. Given a plate thickness of 10μm, the maximum pressure difference expressed as a fraction of the peak pressure would be approximately:

$$\frac{\Delta p}{p_o} \cong \sin \frac{2\pi \cdot 3500 Hz}{343 \, m/s} 1\times10^{-5} m = 6.4\times10^{-4} \text{ or } 0.06\%$$

Even assuming that the acoustic pressure is transmitted to the back of the plate by traveling around the 500μm thick substrate, the fractional difference in the pressure would only be about 6%. Although this back of the envelope calculation fails to consider details on how the acoustic wave interacts with the

device, it is expected to give a reasonable upper limit to the pressure difference in this extremely low Reynold's number regime.

If the pressure difference between the top and bottom of the device is so small, the question then arises as to why the displacement amplitudes are not considerably smaller. To answer this question, this research proposes that the particle velocity of the air molecules moving past the plate provides an additional force on the plates in the direction of the air movement. Zhang's formula for air damping was developed for a cantilever oscillating in still air – not for a cantilever vibrating from a sound wave incident. Therefore, the relevant parameter for calculating the drag is the difference between the air particle velocity and the plate velocity. This concept also appeared in the damping theory proposed by Newell. He stated that the rate at which momentum is exchanged between the molecules and the device is proportional to the difference in velocity between them.

The drag force on one of the plates in the bending mode can be estimated using the above modification in Zhang's formula. This is accomplished by assuming that the plate velocity varies linearly from the hinge of the device to the edge of the plate. This back of the envelope calculation appears in Appendix 1. It turns out that the force from the air particle velocity is about 1/20 of the force on the top plates due to the incident acoustic pressure for a pressure of 1 Pa.

COMSOL calculates the velocity of the plates as w_t_smsld and the particle velocity as vz_acpr. Therefore, to implement the modified damping force, the formula for pda as presented in Table 1 was changed to:

$$pda\,\mathrm{mod} = \mathrm{b*\pi*(ro*mu*omega\_smsld/2)^{\frac{1}{2}}*(w\_t\_smsld - vz\_acpr)}.$$

In the new set of simulations, the "Sphere Model" was again used as the acoustics domain. The new boundary conditions, applied at the back of the

device, incorporate both the acoustic pressure as calculated by COMSOL and the modified damping formula. They appear in Figure 48. All other settings were unchanged.

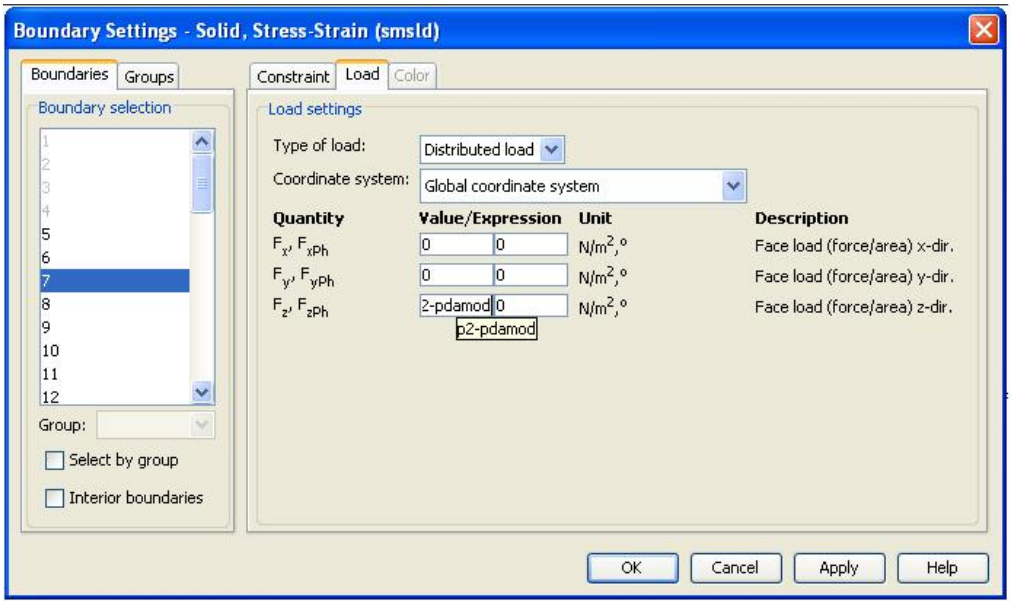

Figure 48. Revised back boundary settings.

The results for the revised simulation for an incident pressure of 1 Pa and angle of 45º appear in Table 7. The frequency response appears in Figure 49.

Incident Angle	**Frequency**		**Displacement Amplitude Ipsilateral Wing**	
	Rocking Mode (Hz)	Bending Mode (Hz)	Rocking Mode (nm)	Bending Mode (nm)
45º	3,432	10,846	189	2,957

Table 7. COMSOL simulation results for a solid plate device in a sphere Acoustic Domain with revised boundary conditions.

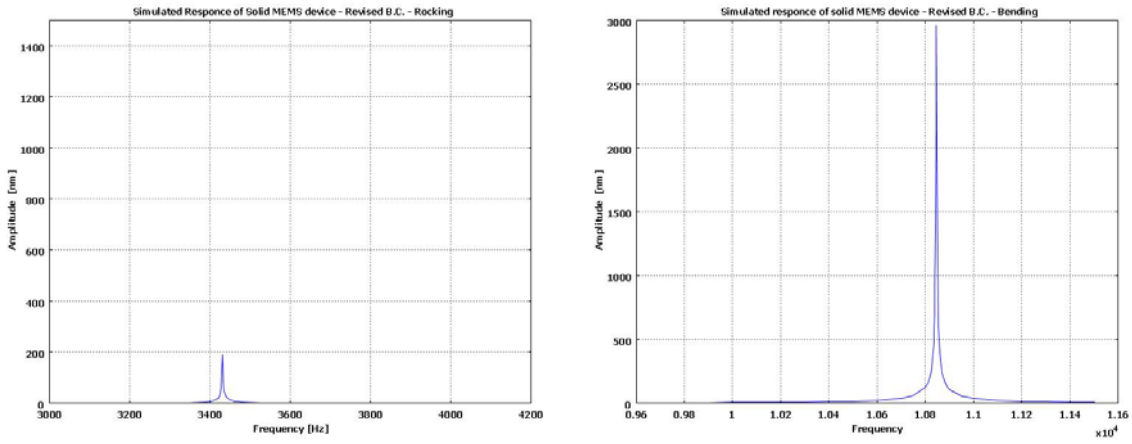
Simulated Responce of Solid MEMS device - Revised B.C. - Rocking
Amplitude [nm]
Frequency [Hz]
Simulated responce of solid MEMS device - Revised B.C. - Bending
Amplitude [nm]
Frequency
x10^4

Figure 49. Frequency response for revised boundary settings.

Compared with the results obtained from the original boundary conditions used by Dritsas, there is a small deviation in the resonance frequencies. The rocking mode resonance frequency decreased by 0.5% and the bending mode resonance frequency decreased by 0.3%. The displacement amplitudes were both lower – 75% lower for the rocking mode and 26% for the bending mode.

The above amplitude results can be compared to the experimental ones presented in Dritsas' thesis. These were achieved for a chip where the backing was removed. These results appear in Table 8 and Figure 50. The simulated values of the resonance frequencies appear to be larger – 22% for the rocking mode and 2% for the bending mode. Again, the deviation in the rocking mode resonance can be attributed to limitations in the precision with which the plate thicknesses can be controlled in the construction process, as previously discussed.

Parameter	Description	Value
P_r	Sound pressure at rocking frequency	199526.23 μPa
P_b	Sound pressure at bending frequency	63095.74 μPa
γ_r	Damping coefficient in rocking mode	13 Hz
γ_b	Damping coefficient in bending mode	105 Hz
υ_s	Sound velocity	344 m/sec
d	Distance between the two point forces	1 mm
ω_b	Frequency of bending mode	2π *10630 Hz
A_r	Amplitude of vibration in rocking mode	29.23 nm
A_b	Amplitude of vibration in bending mode	31.1 nm

Table 8. Experimental values as presented by Dritsas (*From*: Dritsas, 2008).

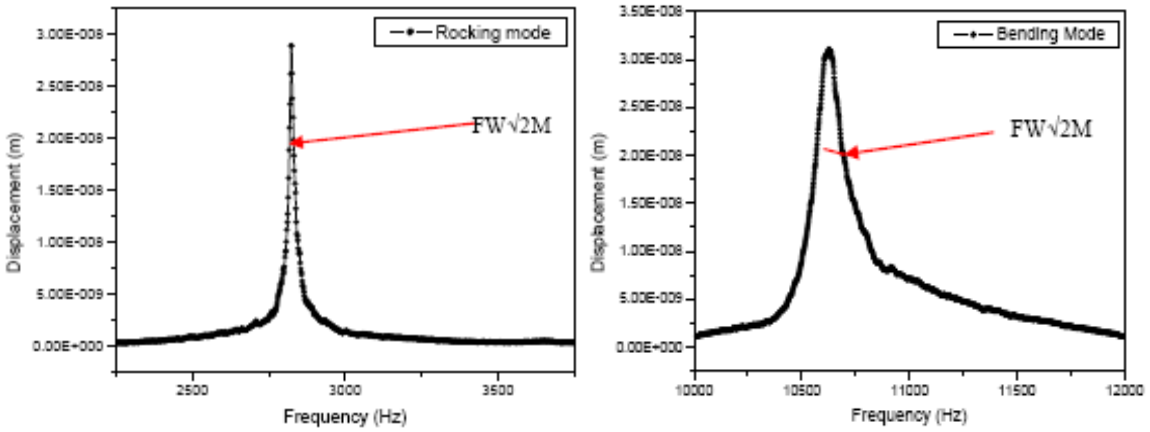

Figure 50. Experimental response for the rocking and bending mode (*From*: Dritsas, 2008).

The displacement amplitude results were not included because of concerns about the accuracy of the calibration procedure used in the experiment. Table 9 is a comparison table for the results of simulations conducted with the different boundary conditions analyzed up to that point and the most accurate experimental results, provided by Professor Karunasiri. The incident pressure is 1 Pa and the polar angle is 45^0.

		Non acoustic coupled simulation – pressure applied only on the top of plate – damping proportional to plate velocity (Dritsas Model)	Acoustic coupled simulation – sphere acoustic domain - pressure applied only on the top of plate - damping proportional to plate velocity	Acoustic coupled simulation - sphere acoustic domain - pressure applied on the top plate AND the back of plate - plate velocity AND particle velocity used to calculate "damping" force	Experimental results for a solid plate device (Extrapolated to an incident pressure of 1Pa)
Resonance Frequency Value [Hz]	Rocking Mode	3,480	3,450	3,432	2,800
	Bending Mode	11,100	10,906	10,846	10,630
Amplitude Value [nm] (Ipsilateral wing)	Rocking Mode	705	777	189	1,200
	Bending Mode	4,254	4,028	2,957	2,000

Table 9. Comparison of simulation and experimental results for the solid, non-backed MEMS device.

5. Perforated Plate Simulation

As mentioned previously, Shivok and Dritsas both tested devices with perforated plates. The main reason to consider such a design was to increase the displacement amplitude and control squeeze-film damping for devices without trenched substrate. The simulation methods developed in this thesis were also applied to the perforated plate design. This was an attempt to determine if it would be more successful than previous simulation methods in predicting the displacement amplitudes.

A design of one of the perforated devices (Device #10) appears in Figure 51.

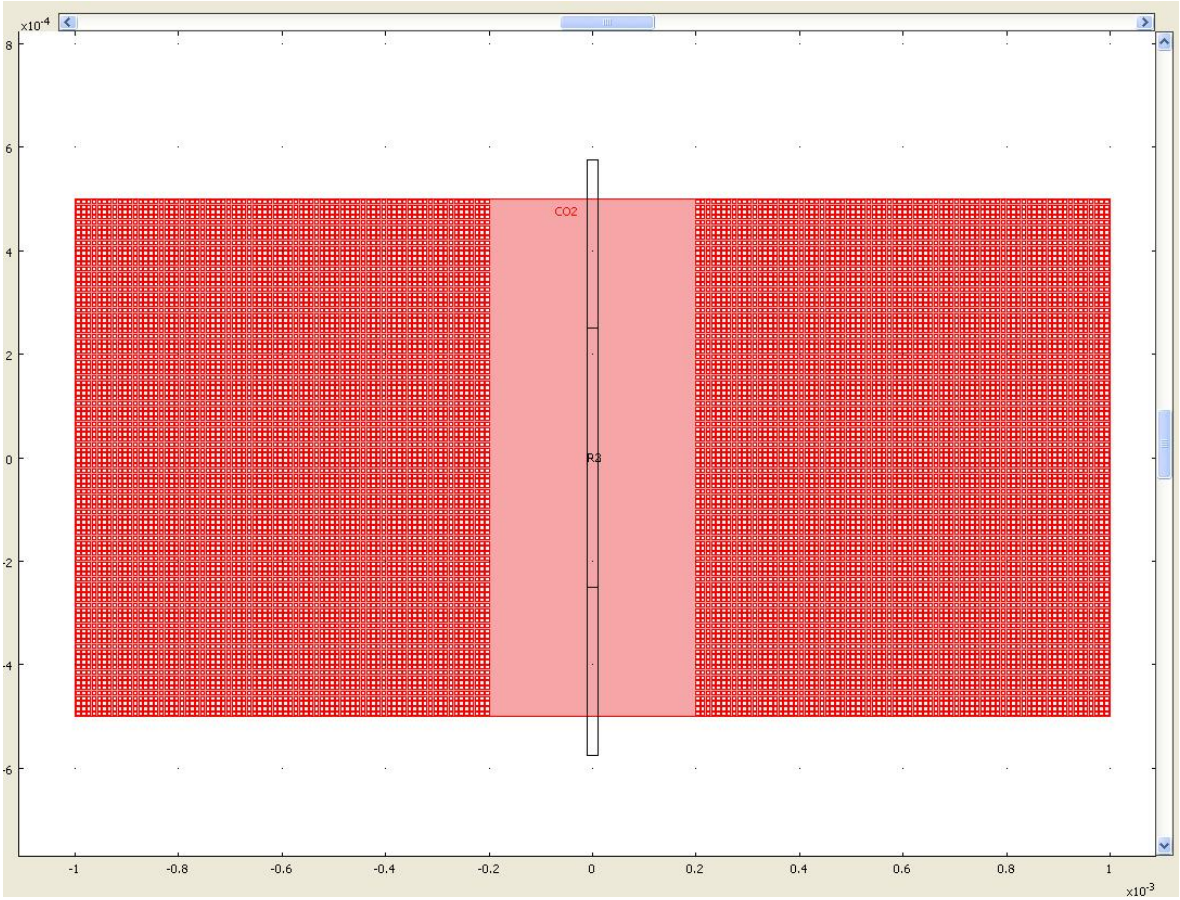

Figure 51. 2-D representation of Device #10.

The device consisted of 8,000 square holes per wing. The dimensions of each hole were 7μm x 7μm. The thickness was 10 μm. Unfortunately, COMSOL could not handle the requirements of such a dense perforation in the configuration used. During the initial step of extruding the design in 3-D, there were difficulties and error messages.

To overcome the design problem and achieve a simulation of a perforated plate, an alternative design was used. The idea was to create a design with the

same percentage of area removed from each plate with only four large holes. The total area of holes in the initial design was $7x10^{-6}$ m x $7x10^{-6}$ m x 8000 = $3.92x10^{-7} m^2$. Therefore, to achieve the same area with four holes, each hole was given an area of $9.8x10^{-8} m^2$. This design appears in Figure 52.

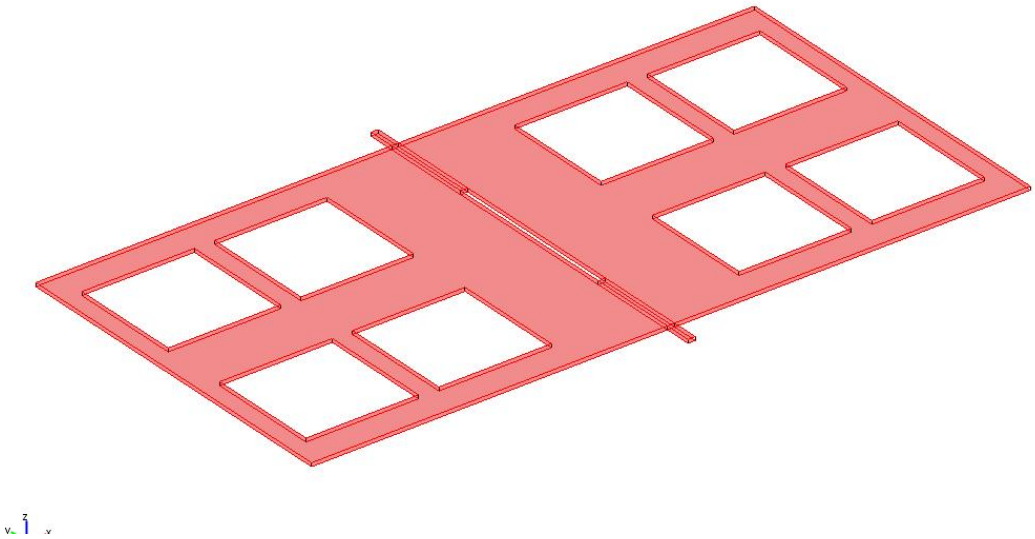

Figure 52. 4-Hole equivalent of Device #10.

To achieve a rough estimate of the rocking mode resonance frequency with the mass removed requires estimating the percent of silicon removed from the device. The mass is calculated as:

$$m = \rho A d$$

where ρ is the density of the plate; A is the area of the plate; and d is the thickness. Therefore, the ratio of the initial mass of the plates, m_1, to the remaining mass of the plate, m_2, after perforation is:

$$\frac{m_1}{m_2} = \frac{\rho A_1 d}{\rho A_2 d} = \frac{A_1}{A_2}$$

Since the area of one of the solid plates is $A_1 = 1x10^{-6}m^2$ and the total area of the holes per plate is $A_{holes} = 4x9.8x10^{-8}m^2 = 3.92 \times 10^{-7}m^2$, the remaining mass is:

$$m_2 = \frac{A_1 - A_{holes}}{A_1} m_1 = \frac{1x10^{-6} - 3.92x10^{-7}}{1x10^{-6}} m_1 \approx 0.6m_1$$

The rocking mode resonance is proportional to the inverse square root of the mass, i.e.,:

$$f_r \propto \sqrt{\frac{k_r}{m}} \Rightarrow f_r \propto m^{-\frac{1}{2}}$$

Therefore, the resonance frequency of the rocking mode is expected to increase to:

$f_{r2} = (0.60)^{-\frac{1}{2}} f_{r\_init} \Rightarrow f_{r2} = 1.291x3,450Hz \Rightarrow f_{r2} = 4,453Hz$.

The same calculation for the bending mode gives $f_{b2} = 13,900Hz$.

The simulation was conducted using the sphere model acoustics' domain. The sound pressure calculated by COMSOL was applied to both the top and the bottom of the plate. To incorporate both the plate velocity and the particle velocity, drag was calculated using the modified Zhang formula.

Table 10 shows the results of the simulation for an incidence pressure of 1 Pa and an angle of 45º. Figure 53 presents the frequency response of the device. As expected, the resonance frequencies increased. The error between the analytical estimations based on the change in mass and the simulated values was 5% for the rocking mode and 10% for the bending mode. Considering the accuracy of the meshing used in this research's model, these discrepancies are within reasonable limits. On the other hand, using denser meshing would vastly increase a solution time that was already large.

Incident Angle	Frequency		Displacement Amplitude Ipsilateral Wing	
	Rocking Mode (Hz)	Bending Mode (Hz)	Rocking Mode (nm)	Bending Mode (nm)
45º	4,684	12,511	17	282

Table 10. Simulated results for a 4-hole equivalent of Device #10 in a spherical Acoustic Domain.

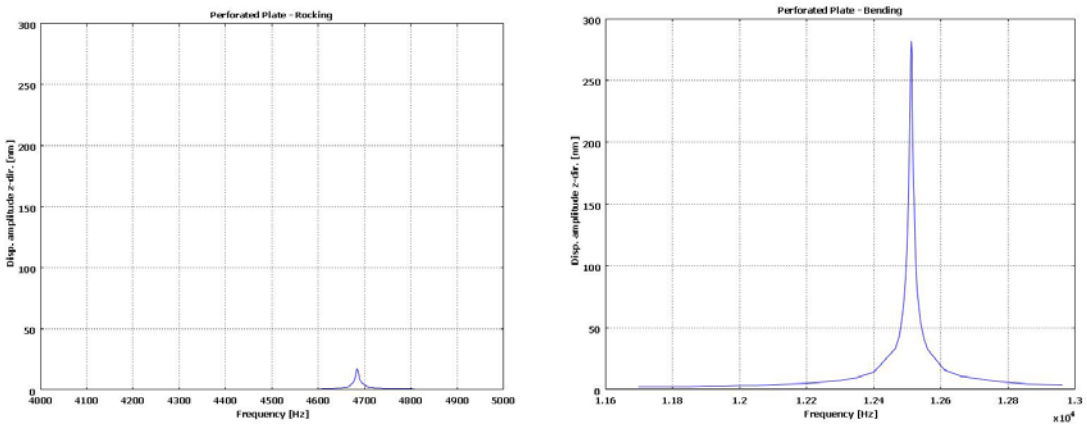

Figure 53. Frequency response for a 4-hole equivalent of Device #10.

Compared with those of a solid plate, the displacement amplitudes were reduced by 91% for both the rocking and bending modes. Note that both simulations were conducted under the same boundary conditions as those presented in paragraph D.4., i.e., the pressure is applied to both the top and the bottom of the plates. Drag is calculated using the modified Zhang's formula to include the air particle velocity. This reduction, which was exhibited by Shivok's experimental results, cannot be solely attributed to the reduction in the effective area of the plate. If this were the case, the reduction would be expected to be proportional to the percentage of the area removed, i.e., around 40%. It must nevertheless be noted that, the experimental results achieved by Shivok [2007], did not use sound excitation.

Running the above simulation with the boundary conditions defined by Dritsas, i.e., taking into account the pressure only on the top of the plate and calculating the damping using only the plate velocity, results in displacement amplitudes that are too high for the perforated plates. This suggests that the model used by Dritsas is not physically realistic.

More recent experimental data on devices with perforated plates show significantly higher amplitude values than those presented by Shivok and Dritsas. This suggests that the plates in previous devices might not have been properly released from the substrate. Further investigation is thus required to determine the actual physical behavior of perforated designs.

6. Device with Resonant Cavity

As discussed in the theory chapter, a resonant cavity (Helmholtz resonator) acts as an amplifier for an incident sound wave. Therefore, it is conceivable that a resonant cavity might be capable of increasing the displacement amplitude of a MEMS device placed either inside it or at its opening. To test this hypothesis, a square cavity was designed as shown in Figure 54. The goal was to create a cavity with a resonance frequency close to a natural frequency of the device.

In this work, the existing slit in the center of the plates and around the edges is used as the opening to the resonant cavity. To use the theory presented in Chapter III, the total open area is equated to a circular shape.

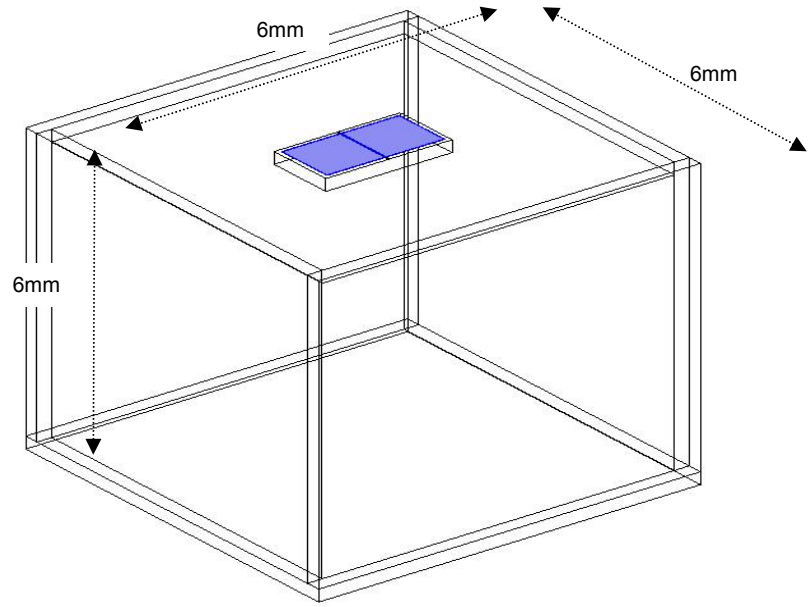

Figure 54. Resonator cavity and MEMS device.

The gap between the plates of the device and the supporting substrate was designed to be 75μm. Using this and the area of the center slit gives a total opening area, S, of $4.725\times10^{-7}m^2$. The equivalent radius, α, of a circular area S can be calculated using $\pi\alpha^2 = 4.725\times10^{-7}m^2$ to yield $\alpha \approx 3.88\times10^{-4}m$. Assuming that the neck length is negligible, the effective length is $L' = L + 1.6\alpha = 6.2\times10^{-4}m$. Applying these results to equation (3.18) and solving for the required volume of the cavity to achieve a resonance frequency of the rocking mode, 3.4kHz, gives $V = 1.96\times10^{-7}m^3$. A square cavity with this volume requires the dimensions of each side to be $\approx 6mm$.

The Acoustic Domain was again chosen to be spherical, but to include the resonant cavity, the sphere radius was increased to 8.5 cm. The sound power was increased to produce an incident pressure of 1 Pa. As before, the calculated sound pressure was applied to both the top and the bottom of the plate. To incorporate both the plate velocity and the particle velocity, drag was calculated using the modified Zhang formula.

The results of the simulation appear in Table 11 for three different angles of incidence. The frequency response at an incidence angle of 45º appears on Figure 55.

Incident Angle	**Frequency**			**Displacement Amplitude Ipsilateral Wing**		
	Rocking Mode (Hz)	Cavity Res. (Hz)	Bending Mode (Hz)	Rocking Mode (nm)	Cavity Resonance (nm)	Bending Mode (nm)
30º	3,440	--	10,840	1,312	--	8,418
45º	3,440	4,340	10,840	1,835	660	8,945
60º	3,440	--	10,840	2,082	--	9,845

Table 11. Simulated results for a MEMS device backed by a resonator cavity.

Comparing these results with those in Table 7, obtained with the same boundary conditions, it was observed that the resonance frequencies for both the rocking and bending modes remained almost the same. On the other hand, the displacement amplitude in both modes was amplified significantly. To be more precise, the amplitude of the rocking mode increased by a factor of 10 while that of the bending mode increased by a factor of 3. Another important observation is that there exists a third resonance peak at 4,340 Hz. This peak probably corresponds to the resonance frequency of the cavity. The displacement amplitude of the plate at that frequency is much lower than that at either of the two resonance frequencies of the device.

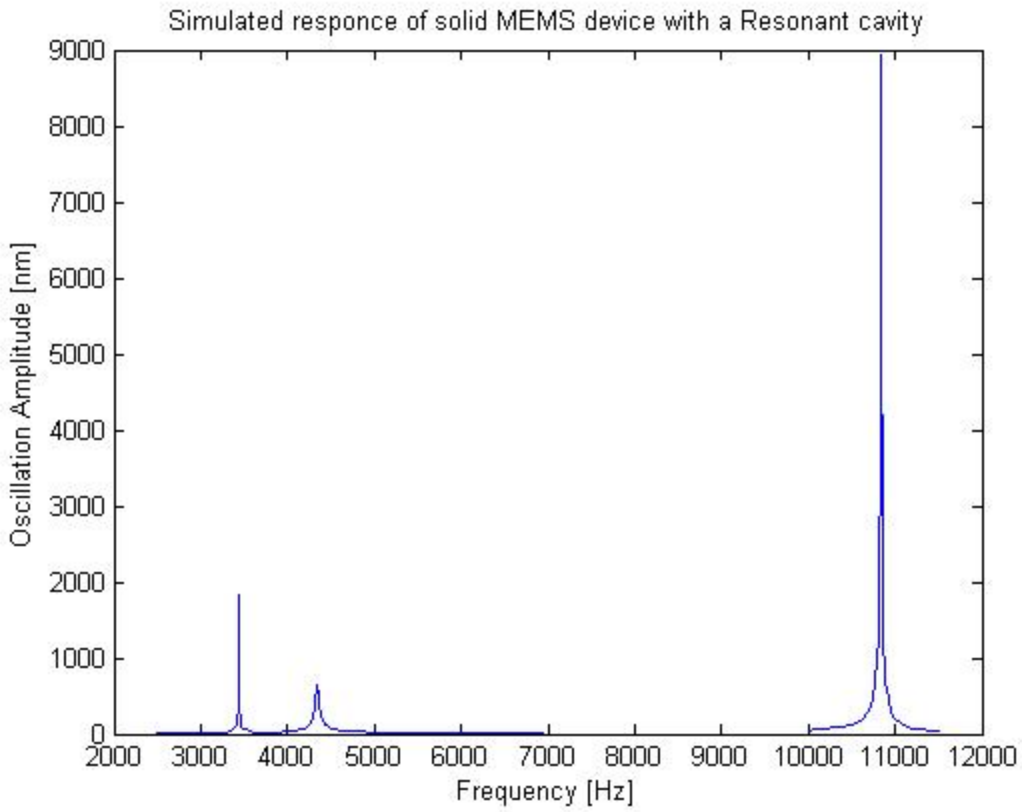

Figure 55. Frequency response of a MEMS device mounted on a resonant cavity.

Figure 56 presents the pressure amplitude value on the ipsilateral and the contralateral edges of the device versus frequency around the “cavity” resonance frequency. It is obvious that there is a large increase of the pressure on the plates of the device compared to the expected value -- around 1 Pa. More work is required to determine whether this result is due to pressure amplification by the device or by the faster air particle velocity streaming past the plates.

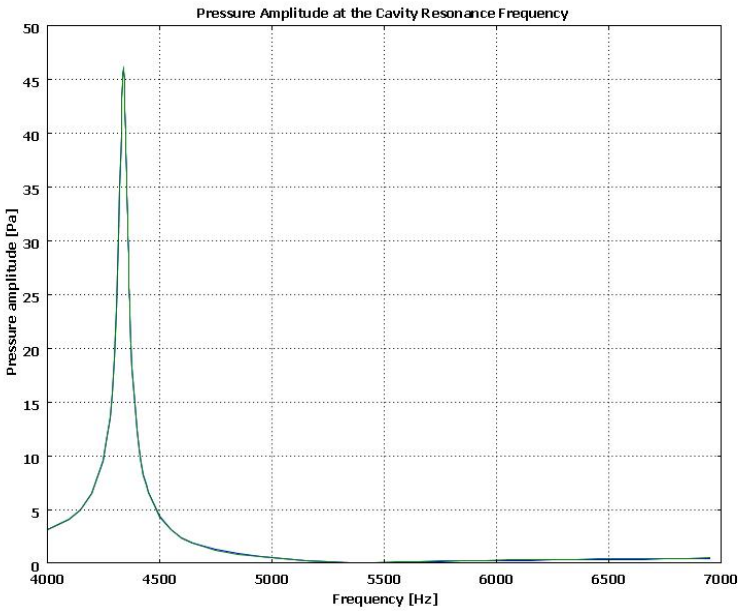

Figure 56. Pressure amplitude on the device plates around the cavity resonance.

The increase in the displacement amplitude of the plates could have been greater if the resonance frequency of the cavity matched that of either the rocking or the bending mode. In that case, however, the dimensions of the cavity for each mode would need to be changed. It may be preferable to have a resonance frequency for the cavity between the rocking and bending mode frequencies.

One of the questions that arose in the above implementation is whether the direction finding capabilities of the device would be affected by the presence of the resonant cavity. The results presented in Table 10 indicate that the behavior of the rocking mode amplitude is as expected, i.e., as the angle of incidence increases, the amplitude also increases. On the other hand, the same behavior also appears in the bending mode, i.e., the amplitude remained almost constant in previous simulations and experiments. This might be an indication that the directionality of the device is adversely affected by the resonant cavity or that the theory needs to be adjusted for this new design. Further research is required to investigate this behavior.

THIS PAGE INTENTIONALLY LEFT BLANK

VI. CONCLUSIONS AND RECOMMENDATIONS FOR FUTURE WORK

To improve upon previous simulations of directional acoustic MEMS devices, a new, more realistic approach was developed. The sound pressure radiated by an acoustic point source was directly coupled with the device. The choice of the acoustics domain posed an important challenge. The pressure amplitude had to be uniform over the surface of the device. Reflections from the simulated boundary of the acoustics domain had to be minimized. A spherical domain large enough to reduce the pressure difference between the two plates of the device to about 5% proved satisfactory.

The new approach managed to couple the sound field to the device and to reproduce the satisfactory simulation results presented previously by Dritsas [2008]. In the rocking mode, the resonance frequency of the acoustic coupled simulation calculated to be 0.7% smaller than of the non-acoustic coupled. The displacement amplitude was calculated to be 16% larger. In the bending mode, the resonance frequency for the acoustic coupled simulation was 2% smaller than of the non-acoustic coupled. The amplitude was 4% larger.

After demonstrating that the new acoustic coupled simulation reproduced previous simulation results when using identical boundary conditions, the boundary settings were revised in an attempt to make the model more realistic. This research made two changes. The first was to couple the acoustic pressure at the back of the plates as well as at the top. Since the device is not closed, the pressure at the back of the plate tends to equilibrate with the incidence sound pressure. In addition, the drag force was modified to include the effect of the sound particle velocity. The simulation results obtained with these new boundary settings were reasonably close to the previous results. The resonance frequencies were only slightly decreased – 0.5% for the rocking mode and 0.3% for the bending mode. The displacement amplitudes decreased by 75% and 26%, respectfully. A comparison with experimental results reported by Dritsas

showed an increase in the simulated resonance frequencies – 22% for the rocking mode and 2% for the bending mode. The simulated amplitude of the rocking mode was approximately 6 times lower than the experimental value. The bending mode was about 47% higher.

Using the revised boundary conditions, an attempt was made to simulate the small displacement amplitudes that had been observed experimentally in devices with perforated plates. Indeed, when the device was perforated, simulation showed a significant decrease of the oscillation amplitude. The reduction in the displacement amplitude calculated to be about 91% for both modes. This exceeded the percentage decrease expected by the reduction of the effective surface area of the plates due to the holes. Therefore, this cannot be explained as a simple percentage reduction in the force applied upon them. Nevertheless, the recent experimental results that showed amplitude values significantly higher that those observed previously might lead to a revision of the boundary conditions that have to be applied on simulation of perforated plates.

An important observation from both simulation and experiment is that these acoustic MEMS devices present sharp resonance peaks, i.e., large quality factors for both the rocking and the bending modes. Dritsas [2008] proposed obtaining a small quality factor through increased damping. This would achieve overlap of the resonance curves of the two modes. The assumption was that this would make the device effective in a larger frequency range. Since a reduced Q also results in reduced amplitude of oscillation, it might not be the most effective technique for attaining a large enough displacement amplitude for both modes simultaneously.

As an alternative, this thesis proposes a design capable of increasing the displacement amplitude of the solid plate MEMS device based on the ability of a Helmholtz resonator to act as a pressure amplifier. Simulation results show that the pressure on the plates is amplified, and the displacement amplitude is significantly increased. The rocking mode amplitude was increased by a factor of ten and the bending mode by a factor of three. Further research on the behavior

of such a design is required, both through simulations and experiment, in order to verify the validity of these results and, more importantly, to investigate whether the directional capabilities of the device are adversely affected.

One of the difficulties of these simulations is to find the most accurate expressions for the drag force on the plates due to the acoustic particle velocity. Zhang and Turner used COMSOL to calculate the expression for the drag force for a variety of cantilevers. Their method might be used for the MEMS microphone to obtain a solution of the full Navier-Stokes equations through COMSOL software to predict the drag force both in cases of solid plate and perforated devices. In this way, simulations would achieve better accuracy.

Furthermore, the spherical domain constructed to couple the sound field to the device makes it easier to explore the directional capabilities of the device through simulation. Up to now, a single source has been assumed with an azimuthal angle of either zero or 180º. In the spherical Acoustic Domain, several sources with variance of power, distance to the source, and angles both polar and azimuthal with respect to the device, can be designed and simulated.

In addition, more devices can be designed side by side in order to form an array of sensors. This array could be excited under the same sound field in order to investigate the feasibility of beamforming.

Another important aspect that needs further investigation is the determination of the angle of incidence based on the displacement amplitudes of the ipsilateral and the contralateral plates. Dritsas calculated the angle of incidence with the use of formula (3.11) that requires a measurement of the incidence pressure for both the rocking and the bending modes. Assuming that the incident sound succeeded in exciting both modes, a separate pressure-measuring device is needed to collect all the data necessary for determining the incident angle. Using the solution to the equations of motion described in the theory chapter, it would be preferable to determine how to find the angle from the amplitude difference between the two plates.

Finally, as mentioned in the modeling chapter, placing the device on the top of a resonant cavity shows potential for a significant increase in displacement amplitudes based on simulations. These results remain to be verified experimentally along with the directional capabilities of such a design. In addition, the resonant cavity design, if proven viable, can also act as a solution for the support of the device as it provides a rigid base with reasonably small dimensions.

APPENDIX

BACK OF THE ENVELOPE CALCULATION FOR THE DAMPING FORCE BASED ON THE MODIFIED ZHANG FORMULA

For a plane wave in air with a pressure of 1 Pa, the particle velocity is $u = \frac{p}{\rho c} = \frac{1Pa}{415Pa \cdot \frac{s}{m}} = 2.4\frac{mm}{s}$,

the device speed would be $u_o = 2\pi \cdot 11,400Hz \cdot 500nm = 35.8\frac{mm}{s}$.

The relevant velocity for drag is the difference between the air particle velocity and the plate velocity. Thus, the force on a plate is proportional to $-\left(u_{plate} - u_{air}\right) = -\Delta u$.

Drag force using Turner's equation:

The force per unit length is given by F:

$$C = \frac{F}{u} = \pi width\sqrt{2\rho\omega\mu}$$

Thus, the net force on a plate could be estimated as:

$$F_{plate-bend} = \frac{\pi width\sqrt{2\rho\omega\mu}}{2} length \cdot u = \pi \cdot S \cdot u\sqrt{\pi\rho f \mu}$$

$$= \pi 10^{-6} m^2 \; 3.58\times10^{-2}\frac{m}{s}\sqrt{1.2\frac{kg}{m^3}\pi \; 11.4\times10^3 Hz \cdot 1.87\times10^{-5}\frac{kg}{m\cdot s}} = 1\times10^{-7} N$$

In terms of average pressure, this is $\langle p \rangle = \frac{F}{A} = \frac{1\times10^{-7} N}{10^{-6} m^2} = 0.1Pa$.

This damping force is 1/10 of the acoustic pressure. Because the velocity closer to the hinge will be smaller, this is an upper limit. The force on one of the plates in the bending mode could be estimated more accurately by assuming that the velocity varies linearly from the hinge to the end. This is the case as long as the plate is rigid (which is expected at these frequencies).

Then:

$$F_{plate-bend} = \int_{o}^{L/2} \frac{\pi width\sqrt{2\rho\omega\mu}}{2}\left(u_{air} - \frac{u_{L/2}}{L/2}x\right)dx = \frac{\pi width\sqrt{2\rho\omega\mu}}{2}\left(u_{air}\frac{L}{2} - u_{plate}\frac{L}{4}\right) =$$

$$\pi 10^{-3} m\sqrt{4\cdot 1.2\frac{kg}{m^3}\pi\ 11.4\times 10^3 Hz\cdot 1.87\times 10^{-5}\frac{kg}{m\cdot s}}\ \frac{10^{-3}m}{2}\left(2.4\times 10^{-3}m - \frac{3.58\times 10^{-2}m}{2}\right) = -4.36\times 10^{-8} N$$

This is equivalent to an average pressure of $\langle p\rangle = \frac{F}{A} = \frac{4.36\times 10^{-8} N}{10^{-6} m^2} \approx 0.05 Pa$.

LIST OF REFERENCES

Bao, M., H. Yang, Y. Sun, and Y. Wang. “Squeeze-film air damping of thick hole-plate.” *Sensors and Actuators A: Physical* 108 (November 2003). 212-217.

COMSOL, (Version 3.4), (2008). [Computer Software]. www.comsol.com. (June 2008).

COMSOL, (October 2007). Acoustics Module Model Library. COMSOL.

COMSOL, (October 2007). Acoustics Module User’s Guide. COMSOL.

COMSOL, (October 2007). MEMS Module User’s Guide. COMSOL.

Dritsas, A. “*Characterization of the MEMS Directional Sound Sensor Fabricated Using the SOIMUMPS Process.*” Master’s Thesis, Monterey, CA: Naval Postgraduate School, June 2008.

Kinsler, L.E., A.R. Frey, A.B. Coppens, and J.V. Sanders. *Fundamentals of Acoustics.* New York: Wiley and Sons, 2000.

Miles, R.N., D. Robert, and R.R. Hoy. “Mechanically coupled ears for directional hearing in the parasitoid fly *Ormia Ochracea.*” *The Journal of the Acoustical Society of America* 98 (December 1995): 3059-3070.

Newell, W.E. “Miniaturization of Tuning Forks.” *Science* 27(161) (September 1968): 1320-1326.

Robert, D., R.N. Miles, and R.R. Hoy. “Tympanal mechanics in the parasitoid fly *Ormia Ocracea.*” Comp. Physiol A. 183 (June 1998).

Shivok, T.J. “*Mems Polymumps_Based Miniature Microphone for Directional Sound Sensing.”* Master’s Thesis, Monterey, CA: Naval Postgraduate School, September 2007.

Smith, S.W. *The Scientists and Engineer’s Guide to Digital Signal Processing*. San Diego: California Technical Publishing, 1997.

Taylor, J.R. *Classical Mechanics.* California: University Science Books, 2005. 187-192; 417-430.

Urick, R.J. *Principles of underwater sound.* Peninsula Publishing, 1983.

Zhang, W. and K. Turner. “Frequency dependent fluid damping of micro/nano flexural resonators: Experiment, model and analysis.” *Sensors and Actuators A: Physical 134* (July 2006): 594-599.

Ziomek, L.J. *Fundamentals of Acoustic Field Theory and Space-Time Signal Processing.* Florida: CRC Press, Inc., 1995.

INITIAL DISTRIBUTION LIST

1. Defense Technical Information Center
   Ft. Belvoir, Virginia

2. Dudley Knox Library
   Naval Postgraduate School
   Monterey, California

3. Daphne Kapolka
   Naval Postgraduate School
   Monterey, California

4. Gamani Karunasiri
   Naval Postgraduate School
   Monterey, California

5. LT Dimitrios Chatzopoulos
   Naval Postgraduate School
   Monterey, California